INSTITUTO POLITÉCNICO NACIONAL
CENTRO INTERDISCIPLINARIO DE INVESTIGACIÓN PARA EL DESARROLLO INTEGRAL REGIONAL UNIDAD OAXACA

DOCTORADO EN CIENCIAS EN CONSERVACIÓN Y APROVECHAMIENTO DE RECURSOS NATURALES

SENSORES DE RESONANCIA MAGNÉTICA PARA CARACTERIZAR ASPECTOS DE DURABILIDAD DEL RECUBRIMIENTO DE CONCRETO

TESIS QUE PARA OBTENER EL GRADO DE:
DOCTOR EN CIENCIAS
PRESENTA:
M. EN C. FLORIBERTO DÍAZ DÍAZ

DIRECTOR DE TESIS:
DR. PRISCILIANO FELIPE DE JESÚS CANO BARRITA

Santa Cruz Xoxocotlán, Oaxaca abril de 2021

SIP-13
REP 2017

INSTITUTO POLITÉCNICO NACIONAL
SECRETARIA DE INVESTIGACIÓN Y POSGRADO

ACTA DE REGISTRO DE TEMA DE TESIS Y DESIGNACIÓN DE DIRECTOR DE TESIS

Ciudad de México, a 20 de Abril del 2021

El Colegio de Profesores de Posgrado de CIIDIR UNIDAD OAXACA en su Sesión
(Unidad Académica)

ordinaria No. 07 celebrada el día 13 del mes Agosto de 2018, conoció la solicitud presentada por el (la) alumno (a):

Apellido Paterno:	Díaz	**Apellido Materno:**	Díaz	**Nombre (s):**	Floriberto

Número de registro: A 1 5 0 1 1 6

del Programa Académico de Posgrado: Doctorado en Ciencias en Conservación y Aprovechamiento de Recursos Naturales

Referente al registro de su tema de tesis; acordando lo siguiente:

1.- Se designa al aspirante el tema de tesis titulado:

"Sensores de resonancia magnética para caracterizar aspectos de durabilidad del recubrimiento de concreto"

Objetivo general del trabajo de tesis:

Diseño, construcción y caracterización de sensores de resonancia magnética nuclear para detectar señales de núcleos de ^{1}H, ^{23}Na y ^{35}Cl para caracterizar materiales basados en cemento.

2.- Se designa como Directores de Tesis a los profesores:

Director: Dr. Prisciliano Felipe de Jesús Cano Barrita 2° Director:

No aplica: ☐

3.- El Trabajo de investigación base para el desarrollo de la tesis será elaborado por el alumno en:

Centro Interdisciplinario de Investigación para el Desarrollo Integral Regional, Unidad Oaxaca

que cuenta con los recursos e infraestructura necesarios.

4.- El interesado deberá asistir a los seminarios desarrollados en el área de adscripción del trabajo desde la fecha en que se suscribe la presente, hasta la aprobación de la versión completa de la tesis por parte de la Comisión Revisora correspondiente.

Director(a) de Tesis

Dr. Prisciliano Felipe de Jesús Cano Barrita

2° Director de Tesis (en su caso)

Aspirante

Díaz Díaz Floriberto

Presidente del Colegio

Dr. Salvador Isidro Belmonte Jiménez

ESTADOS UNIDOS MEXICANOS

CENTRO INTERDISCIPLINARIO
DE INVESTIGACIÓN PARA EL
DESARROLLO INTEGRAL REGIONAL
C.I.I.D.I.R.
UNIDAD OAXACA
I.P.N.

SIP-14
REP 2017

INSTITUTO POLITÉCNICO NACIONAL

SECRETARÍA DE INVESTIGACIÓN Y POSGRADO

ACTA DE REVISIÓN DE TESIS

En la Ciudad de Santa Cruz, Xoxocotlán, Oax., siendo las 11:00 horas del día 27 del mes de Febrero del 2021 se reunieron los miembros de la Comisión Revisora de la Tesis, designada por el Colegio de Profesores de Posgrado de: Centro de Investigación Interdisciplinario para el Desarrollo Integral Regional, unidad Oaxaca para examinar la tesis titulada: **"Sensores de resonancia magnética para caracterizar aspectos de durabilidad del recubrimiento de concreto"** del (la) alumno (a):

Apellido Paterno:	Díaz	**Apellido Materno:**	Díaz	**Nombre (s):**	**Floriberto**

Número de registro: A 1 5 0 1 1 6

Aspirante del Programa Académico de Posgrado:

Doctorado en Ciencias en Conservación y Aprovechamiento de Recursos Naturales

Una vez que se realizó un análisis de similitud de texto, utilizando el software antiplagio, se encontró que el trabajo de tesis tiene ___5___ % de similitud. **Se adjunta reporte de software utilizado**.

Después que esta Comisión revisó exhaustivamente el contenido, estructura, intención y ubicación de los textos de la tesis identificados como coincidentes con otros documentos, concluyó que en el presente trabajo **SI** ☐ **NO** ☒ **SE CONSTITUYE UN POSIBLE PLAGIO.**

JUSTIFICACIÓN DE LA CONCLUSIÓN:

No se constituye un posible plagio debido a que el porcentaje de similitud es bajo (5 %) y principalmente se encuentra en algunas partes de marco teórico, así como en materiales y método, en los cuales se incluyen las referencias a las fuentes originales. Se eliminó del análisis el artículo publicado en la revista Cement and Concrete Research que forma parte de esta tesis.

****Es responsabilidad del alumno como autor de la tesis la verificación antiplagio, y del Director o Directores de tesis el análisis del % de similitud para establecer el riesgo o la existencia de un posible plagio.**

Finalmente y posterior a la lectura, revisión individual, así como el análisis e intercambio de opiniones, los miembros de la Comisión manifestaron **APROBAR** ☒ **SUSPENDER** ☐ **NO APROBAR** ☐ la tesis por **UNANIMIDAD** ☒ o **MAYORÍA** ☐ en virtud de los motivos siguientes:

La tesis satisface los requerimientos señalados en las disposiciones reglamentarias vigentes.

COMISIÓN REVISORA DE TESIS

Dr. Priscliano Felipe de Jesús Cano Barrita Director de Tesis Nombre completo y firma	Dra. Luicita Lagunez Rivera Nombre completo y firma	Dr. Francisco Castellanos León Nombre completo y firma
Dra. Delia Soto Castro Nombre completo y firma	Dr. Magdaleno Caballero Caballero Nombre completo y firma	Dr. Salvador Isidro Belmonte Jiménez Nombre completo y firma **PRESIDENTE DEL COLEGIO DE PROFESORES**

CENTRO INTERDISCIPLINARIO
DE INVESTIGACIÓN PARA EL
DESARROLLO INTEGRAL REGIONAL
C.I.I.D.I.R.
UNIDAD OAXACA
I.P.N.

INSTITUTO POLITÉCNICO NACIONAL
SECRETARÍA DE INVESTIGACIÓN Y POSGRADO

CARTA CESIÓN DE DERECHOS

En la Ciudad de **Oaxaca de Juárez** el día **18** del mes de **febrero** el año **2021**, el que suscribe **Floriberto Díaz Díaz** alumno del Programa de **DOCTORADO EN CIENCIAS EN CONSERVACIÓN Y APROVECHAMIENTO DE RECURSOS NATURALES** con número de registro **A150116**, adscrito a Centro Interdisciplinario de Investigación para el Desarrollo Integral Regional Unidad Oaxaca, manifiesta que es autor intelectual del presente trabajo de Tesis bajo la dirección del **Dr. Prisciliano Felipe de Jesús Cano Barrita** y cede los derechos del trabajo titulado: **"Sensores de resonancia magnética para caracterizar aspectos de durabilidad del recubrimiento de concreto"** al Instituto Politécnico Nacional para su difusión, con fines académicos y de investigación.

Los usuarios de la información no deben reproducir el contenido textual, gráficas o datos del trabajo sin el permiso expreso del autor y/o director del trabajo. Este puede ser obtenido escribiendo a la siguiente dirección **floribertodiazdiaz@gmail.com**. Si el permiso se otorga, el usuario deberá dar el agradecimiento correspondiente y citar la fuente del mismo.

ESTADOS UNIDOS MEXICANOS

Floriberto Díaz Díaz

Nombre y firma

CENTRO INTERDISCIPLINARIO
DE INVESTIGACIÓN PARA EL
DESARROLLO INTEGRAL REGIONAL
C.I.I.D.I.R.
UNIDAD OAXACA
I.P.N.

Resumen

La resonancia magnética nuclear (RMN) es una técnica no destructiva que ha sido utilizada con éxito para estudiar materiales basados en cemento. No obstante, el alto costo, la portabilidad y la limitación del tamaño de muestra son los principales inconvenientes al momento de emplear sistemas convencionales de RMN con magnetos superconductores. Esta investigación presenta el uso de distintos sensores de RMN de campo bajo para caracterizar de manera no destructiva aspectos relacionados con la durabilidad del concreto hidráulico. Se utilizó un arreglo unilateral de tres magnetos con una antena elíptica de superficie para caracterizar la profundidad de carbonatación en morteros de cemento Portland con una relación a/c = 0.60, saturados y no saturados. El punto de cruce entre el perfil de T_2 y el perfil de intensidad de la señal coincide con la profundidad de carbonatación determinada con la prueba de la fenolftaleína. La profundidad a la cual T_2 empieza a ser relativamente constante es 1.44 veces la profundidad obtenida con la prueba de la fenolftaleína. Un segundo estudio con el arreglo de tres magnetos fue la obtención de perfiles de distribución de humedad durante absorción capilar en muestras de mortero y concreto. Los perfiles obtenidos fueron similares a los obtenidos con la técnica de Imagenología por Resonancia Magnética Single Point Imaging (SPI) utilizando un sistema de campo bajo, donde la ventaja del arreglo de tres magnetos, además de ser portable, es que no existen restricciones en el tamaño de la muestra a analizar. Un tercer estudio fue el diseño y construcción de antenas para detectar señales de RMN del ^{35}Cl y ^{23}Na. Para esto se utilizaron dos magnetos circulares de un sistema comercial de imagenología por RMN que generan un campo magnético de 0.302 Teslas, así como un arreglo Halbach de magnetos que generaron un campo magnético de 1.028 Teslas. Se realizaron mediciones de RMN en soluciones con diferente concentración molar de NaCl y en tres especímenes de pasta de cemento con relación a/c = 0.55 saturadas con soluciones de NaCl. Se obtuvo una relación lineal ($r^2 > 0.96$) entre la intensidad de la señal de RMN para ambos núcleos en las soluciones de NaCl. Un último estudio se enfocó a investigar la relación entre el tiempo de vida T_2 de la señal de RMN con

el ancho de grietas artificiales, generadas con láminas de acero inoxidable, en muestras de pasta de cemento con relación a/c = 0.50. Los resultados mostraron que una de las componentes del tiempo de vida T_2 y su correspondiente intensidad presentan una relación lineal con el ancho de grieta.

Abstract

Nuclear magnetic resonance (NMR) is a non-destructive technique that has been successfully used to study cement-based materials. However, high cost, portability, and limited sample size are the main drawbacks when using conventional NMR systems with superconducting magnets. This research presents the use of low-field NMR sensors to non-destructively characterize aspects related to the durability of hydraulic concrete. A unilateral three-magnet array with an elliptical surface antenna was used to characterize the carbonation depth in saturated and unsaturated 0.60 w/c ratio Portland cement mortars. The crossover point between the T_2 profile and the signal intensity profile coincides with the carbonation depth determined with the phenolphthalein test. The depth at which T_2 stars to behave relatively constant is 1.44 times the depth obtained with the phenolphthalein test. A second study with the three-magnet array was to obtain moisture distribution profiles in mortar and concrete samples. The profiles obtained were similar to those obtained with the Single Point Imaging (SPI) MRI technique using a low-field system, where the advantage of the three-magnet array, in addition to being portable, is that there are no restrictions on the sample size. A third study was the design and construction of antennas to detect ^{35}Cl and ^{23}Na NMR signals. Two circular magnets from a commercial MRI system that generate a magnetic field of 0.302 Tesla were used, as well as a Halbach magnet array that generated a magnetic field of 1.028 Tesla. NMR measurements were undertaken in NaCl solutions with different molar concentrations, and in three 0.55 w/c ratio cement paste specimens saturated with NaCl solutions. For both nuclei, a linear relationship was obtained ($r^2 > 0.96$) between the NMR signal intensity and the NaCl concentration. A last study focused on investigating the relationship between the T_2 lifetime and the width of artificial cracks, generated with stainless steel sheets, in 0.50 w/c ratio cement paste samples. The results showed that the long T_2 lifetime component and its corresponding signal intensity had a linear relationship with the crack width.

Dedicatoria

A mis padres, a mis hermanos y a mi esposa.

Agradecimientos

A través de las presentes líneas deseo expresar mis agradecimientos a todas las personas e instituciones que han colaborado con su soporte científico, humano y económico para la realización de este trabajo de investigación.

A mi tutor y director **Dr. Prisciliano Felipe de Jesús Cano Barrita** por su apoyo y sus consejos durante esta etapa de aprendizaje y formación en el área de la investigación científica. Por su constancia, paciencia y orientación durante la elaboración de esta tesis. Finalmente, quiero agradecer la confianza que ha depositado en mi persona y la amistad que me ha brindado.

Al **Instituto Politécnico Nacional y CIIDIR Unidad Oaxaca**, por ser la casa de estudios que me abrió las puertas de su seno científico para poder realizar mis estudios de doctorado y por todo el apoyo brindado.

Al **Consejo Nacional de Ciencia y Tecnología (Conacyt)** por la beca de posgrado otorgada para la realización de mis estudios de doctorado.
A la **Comisión de Operación y Fomento de Actividades Académicas** (**COFAA**) del Instituto Politécnico Nacional por la beca **BEIFI** otorgada.

Al **Dr. Bruce J. Balcom**, director del Centro de Imagenología por Resonancia Magnética de la Universidad de New Brunswick, por donar el arreglo unilateral de tres magnetos con la cuál fue realizada parte de esta investigación.

Al **Conacyt** por financiar el proyecto "Estudio de las propiedades de durabilidad del recubrimiento del concreto por medio de resonancia magnética de los núcleos ^{1}H y ^{35}Cl", Proyecto Conacyt Ciencia Básica clave 239727 bajo la dirección del Dr. Prisciiano Felipe de Jesús Cano Barrita.

A la **Secretaría de Investigación y Posgrado del Instituto Politécnico Nacional** por financiar el proyecto Clave SIP 20170803.

A los miembros de comisión revisora: **Dra. Luicita Lagunez Rivera, Dra. Delia Soto Castro, Dr. Magdaleno Caballero Caballero, Dr. Prisciliano Felipe de Jesús Cano Barrita y al Dr. Francisco Castellanos León**, por el tiempo invertido en la revisión de mi trabajo de tesis y comentarios hechos al respecto con el fin de mejorarlo.

Al **M. en C. Frank Manuel León Martínez** por las contribuciones y observaciones hechas a mi trabajo, y por su valiosa amistad.

A todos **los compañeros y amigos del CIIDIR** en especial a los del área de materiales basados en cemento por el apoyo que me brindaron en la elaboración de los especímenes y por las numerosas discusiones que hemos tenido durante las presentaciones de avances que se realizaba en nuestro grupo.

Índice

Índice de figuras

Índice de tablas

Capítulo 1. Introducción general

En la actualidad el concreto se ha vuelto uno de los materiales más utilizados en el mundo para la construcción de diversas estructuras, gracias a que es un material resistente al agua, permite dar una gran variedad de formas y tamaños a las estructuras y es un material relativamente de bajo costo (Mehta & Monteiro, 2006). Desafortunadamente, la vida útil de las estructuras de concreto reforzado se ve reducida por distintas causas de deterioro dependiendo de las condiciones ambientales en las que se encuentran expuestas.

El agua está presente en diversos mecanismos de deterioro del concreto, tales como el agrietamiento por contracción durante secado, el ingreso de agentes agresivos como iones cloruro, CO_2 y sulfatos. Por ejemplo, los iones cloruro al ingresar a través de procesos de absorción capilar y difusión causan deterioro por corrosión cuando una cierta concentración de cloruros se presenta en la superficie del acero de refuerzo y despasiva la capa protectora del mismo. Por otra parte, el CO_2 es un agente que causa la carbonatación del concreto que penetra a través de los poros y microgrietas del recubrimiento del concreto. Durante la carbonatación, el hidróxido de calcio, de naturaleza alcalina, contenido en la pasta de cemento hidratada reacciona con el dióxido de carbono disuelto en la solución de poro, formando carbonato de calcio y agua. Este proceso gradual de carbonatación reduce el pH de la solución de poro de valores típicos de 12 – 13 a valores de 9 o menos (Kim et al., 2014; Sideris & Savva, 2005). Cuando el proceso de carbonatación alcanza el nivel del acero de refuerzo, la capa pasiva que protege el acero se destruye y se inicia la corrosión de este.

Los métodos estándar que se utilizan para determinar la condición de humedad, la profundidad de penetración de iones cloruros y la carbonatación en el concreto reforzado, por lo general son destructivos y proveen información de utilidad limitada. El método colorimétrico se utiliza ampliamente para determinar la profundidad de penetración de iones cloruro y la profundidad de carbonatación por medio de soluciones de nitrato de plata en el caso de cloruros (Baroghel-Bouny, Belin, Maultzsch, & Henry, 2007) y fenolftaleína en el caso de carbonatación (RILEM Recommendations CPC-18, 1988). El método consiste en fracturar el espécimen y rociar el nitrato de plata o la fenolftaleína. En el caso de cloruros, la parte de la superficie recién fracturada del espécimen de color blanquecino indica la presencia de cloruros y mientras que la otra parte en color marrón indica la zona libre de cloruros. En el caso de carbonatación, la fenolftaleína (indicador de pH) puede señalar el área carbonatada que permanece incolora, mientras que adquiere un color rosado en la zona no carbonatada. Otra técnica comúnmente utilizada para determinar la profundidad de penetración de cloruro es por medio de muestras de polvo de concreto que se extraen a distintas profundidades y por titulación química se determina la concentración de cloruros. A partir del perfil de concentración de cloruros se estima el coeficiente de difusión de cloruros (NT Build 443, 1995). Sin embargo, esta técnica también es destructiva y requiere de tiempo considerable para llevarse a cabo.

Otro de los factores que afectan la durabilidad del concreto es el agrietamiento, ya que aumenta significativamente su permeabilidad y lo vuelven vulnerable al ingreso de los agentes agresivos (Aldea, Shah, & Karr, 1999). La observación de las grietas se hace mediante microscopios y tarjetas de plástico transparentes que permiten medir el ancho de la grieta hasta 25 μm. También se ha utilizado el procesamiento de imágenes de alta resolución donde se puede detectar grietas de hasta 250 μm de ancho (Zhang, Zhang, Qi, & Liu, 2014), por lo que no puede aplicarse para la detección de grietas más estrechas que son de interés desde el punto de vista de la durabilidad del concreto.

La Resonancia Magnética Nuclear (RMN) es una técnica no destructiva que ha sido utilizada con éxito para estudiar hidratación de materiales base cemento (Apih et al., 2001), determinar perfiles de penetración de cloruros mediante sistemas de imagenología por RMN de campo alto (Cano et al, 2002), caracterizar la condición de humedad, el refinamiento de la porosidad y la resistencia a la compresión de materiales basados en cemento (Díaz-Díaz et al,2013). El inconveniente de esta técnica cuando se utilizan sistemas convencionales de magnetos superconductores, es que son de alto costo de adquisición y de mantenimiento debido al uso de criogénicos como helio y nitrógeno líquidos para mantener una baja temperatura. No obstante, actualmente existen sistemas comerciales de RMN portables con arreglos de magnetos unilaterales como el MOLE (Manz et al, 2006), el MOUSE (Blümich et al., 1998), arreglos de tres magnetos (Marble et al, 2007), los cuales permiten realizar mediciones superficiales y hasta una profundidad de 2.5 cm. Sin embargo, los costos siguen siendo relativamente altos.

El presente trabajo tiene por objetivo el uso de la técnica de Resonancia Magnética Nuclear empleando arreglos de magnetos con antenas de radiofrecuencia diseñadas y construidas para la caracterización, de manera no destructiva, de procesos que afectan la durabilidad del recubrimiento del concreto tales como la carbonatación, la distribución de humedad durante absorción capilar, la penetración de iones cloruros y el agrietamiento, como una alternativa a las técnicas destructivas tradicionales. Por lo tanto, este trabajo está compuesto por seis capítulos organizado de la siguiente manera:

Capítulo 1. Introducción general.

Capítulo 2. Marco teórico. En este capítulo se aborda el marco teórico referente a la técnica de Resonancia Magnética Nuclear.

Capítulo 3. Unilateral low-field magnetic resonance measurements of carbonation depth in unsaturated and saturated Portland cement mortars. Este capítulo aborda el diseño, construcción y caracterización de antenas de RMN para un arreglo unilateral de tres magnetos (Marble et al., 2007) para determinar la profundidad de carbonatación en pastas y morteros de cemento Portland en estado saturado e insaturado. El haber podido determinar el frente de carbonatación en el mortero en estado insaturado significa que esta técnica tiene el potencial de monitorizar el frente de carbonatación en función del tiempo.

Capítulo 4. Moisture distribution profiles during water absorption of mortars obtained nondestructively by low-field unilateral magnetic resonance. Este capítulo trata sobre la obtención de perfiles de humedad en morteros expuestos a absorción capilar por medio de la técnica CPMG de RMN utilizando el arreglo unilateral de tres magnetos y una antena elíptica, comparando estos perfiles con los obtenidos con la técnica Single Point Imaging de imagenología por RMN.

Capítulo 5. Detección de ^{35}Cl y ^{23}Na en soluciones de NaCl y en pastas de cemento saturadas con NaCl. Este capítulo aborda el diseño, construcción y caracterización de antenas de RMN para la detección de ^{35}Cl y ^{23}Na, utilizadas con los magnetos de un sistema comercial de imagenología por RMN y un arreglo Halbach de magnetos. Se detectaron señales de RMN en soluciones de cloruro de sodio (NaCl) y en pastas de cemento saturados con soluciones de NaCl.

Capítulo 6. Crack width estimation in cement paste and mortar by low field magnetic resonance. Este capítulo trata sobre la relación existente entre el ancho de grietas artificiales en pastas de cemento y morteros, con el tiempo de vida T_2 de la señal de RMN.

1.1 Referencias

Aldea, C.-M., Shah, S. P., & Karr, A. (1999). Effect of Cracking on Water and Chloride Permeability of Concrete. *Journal of Materials in Civil Engineering*, *11*(3), 181–187.

Apih, T., Lahajnar, G., Sepe, A., Blinc, R., Milia, F., & Cvelbar, R. (2001). Proton spin - lattice relaxation study of the hydration of self-stressed expansive cement, *31*, 263–269.

Baroghel-Bouny, V., Belin, P., Maultzsch, M., & Henry, D. (2007). AgNO3 spray tests: Advantages, weaknesses, and various applications to quantify chloride ingress into concrete. Part 2: Non-steady-state migration tests and chloride diffusion coefficients. *Materials and Structures/Materiaux et Constructions*, *40*(8), 783–799. https://doi.org/10.1617/s11527-007-9236-y

Blümich, B., Blümer, P., GUTHAUSEN, A., HAKEN, R., SCHMITZ, U., Aito, K. S., & Immer, G. Z. (1998). q Invited Lecture, *16*(98), 479–484.

Cano, F. de J., Bremner, T. W., Mcgregor, R. P., & Balcom, B. J. (2002). Magnetic resonance imaging of 1H , 23Na , and 35Cl penetration in Portland cement mortar. *Cement and Concrete Research*, *32*, 1067–1070.

Díaz-Díaz, F., Cano-Barrita, P. F. de J., Balcom, B. J., Solís-Nájera, S. E., & Rodríguez, A. O. (2013). Embedded NMR sensor to monitor compressive strength development and pore size distribution in hydrating concrete. *Sensors (Switzerland)*, *13*(12), 15985–15999. https://doi.org/10.3390/s131215985

Kim, G., Kim, J.-Y., Kurtis, K. E., Jacobs, L. J., Le Pape, Y., & Guimaraes, M. (2014). Quantitative evaluation of carbonation in concrete using nonlinear ultrasound. *Materials and Structures*, *49*(MARCH), 399–409. https://doi.org/10.1617/s11527-014-0506-1

Manz, B., Coy, A., Dykstra, R., Eccles, C. D., Hunter, M. W., Parkinson, B. J., & Callaghan, P. T. (2006). A mobile one-sided NMR sensor with a homogeneous magnetic field: The NMR-MOLE. *Journal of Magnetic Resonance*, *183*(1), 25–31. https://doi.org/10.1016/j.jmr.2006.07.017

Marble, A. E., Mastikhin, I. V., Colpitts, B. G., & Balcom, B. J. (2007). A compact permanent magnet array with a remote homogeneous field. *Journal of Magnetic Resonance*, *186*(1), 100–104. https://doi.org/10.1016/j.jmr.2007.01.020

Mehta, P. K., & Monteiro, P. J. M. (2006). *Concrete: Microstructure, properties and materials* (3rd ed.). New York: McGraw-Hil. https://doi.org/10.1036/0071462899

NT Build 443. Concrete, Hardened: Acceletared Chloride Penetration (1995).

RILEM Recommendations CPC-18. (1988). CPC-18 Measurement of hardened concrete carbonation depth. *Materials and Structures*, 21(6), 453–455.

Sideris, K. K., & Savva, A. E. (2005). Durability of mixtures containing calcium nitrite based corrosion inhibitor. *Cement and Concrete Composites*, *27*(2), 277–287. https://doi.org/10.1016/j.cemconcomp.2004.02.016

Zhang, W., Zhang, Z., Qi, D., & Liu, Y. (2014). Automatic crack detection and classification method for subway tunnel safety monitoring. *Sensors (Basel, Switzerland)*, *14*(10), 19307–19328.

Capítulo 2. Marco teórico

2.1 Física de la resonancia magnética nuclear

La resonancia magnética nuclear (RMN) se puede definir como una técnica que permite caracterizar propiedades de la materia a nivel molecular, la cual se basa en la absorción y emisión de radiación electromagnética de los núcleos de ciertos átomos, cuando estos son expuestos a un campo magnético intenso y excitados por pulsos de radiofrecuencia con características específicas (Blümich, Sabina, & Zia, 2014; Fukushima & B.W. Roeder, 1981; Macomber & Harbison, 1997). Los experimentos de RMN solo pueden funcionar con los núcleos de algunos átomos que cumplen con una propiedad cuántica llamada momento angular de giro o spin.

2.1.1 Momento angular o spin

Para entender mejor el momento angular nuclear es importante analizar el momento angular del electrón. El electrón, al igual que el fotón, cumple con la propiedad dual onda-partícula. En el átomo una onda de electrón está caracterizada por cuatro números cuánticos: n niveles de energía, l subniveles de energía, m_l número magnético y m_s spin, el cual puede tomar dos valores $+\frac{1}{2}$ o -$\frac{1}{2}$ (Macomber & Harbison, 1997). En un átomo dos electrones no pueden tener los mismos números cuánticos de acuerdo con el principio de exclusión de Pauli (Brown, Cheng, Haacke, Thompson, & Venkatesan, 2014). Por lo tanto, un orbital solo puede contener como máximo dos electrones, los cuales deben tener diferente número cuántico spin; en otros términos, dos electrones compartiendo el mismo orbital siempre se encuentran en estado bajo de energía, lo que significa que tienen momento angular opuesto también llamado apareamiento de electrones (Fig. 2.1). Dado que el electrón tiene carga, este movimiento de spin produce un momento magnético (μ).

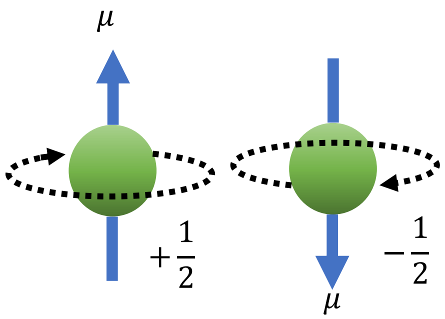

Figura 2.1 Apareamiento de electrones, debido a la dirección opuesto de *spin* el momento angular resultante es cero.

El núcleo del átomo está constituido por protones y neutrones, también conocido como nucleones, estos al igual que el electrón poseen un momento angular y también existe apareamiento entre ellos (protón-protón y neutrón-neutrón). Por lo tanto, el spin nuclear I es resultado de la suma del momento angular de los nucleones no apareados y toma valores de cero y múltiplos de $\frac{1}{2}$, de aquí se tiene que únicamente los átomos con $I \neq 0$ son visibles para la RMN. Esto ocurre cuando el número de masa es impar y/o cuando el número de masa es par pero el número atómico es impar. Siguiendo la analogía del electrón, en el núcleo del átomo de igual forma se produce un momento angular magnético μ cuando éste posee un valor de spin diferente de cero.

2.1.2 Estados de energía y precesión nuclear

A causa del movimiento térmico la orientación de μ es aleatorio en ausencia de algún campo magnético estático externo (Fig. 2.2a), es decir, para la materia a nivel macroscópico, en equilibrio térmico, no existe una magnetización neta (Brown et al., 2014). Por otra parte, al ser sometidos a un campo magnético constante e intenso (B_0) se alinean con este (Figura 2.2 b), algo parecido a lo que ocurre con las brújulas y el campo magnético terrestre.

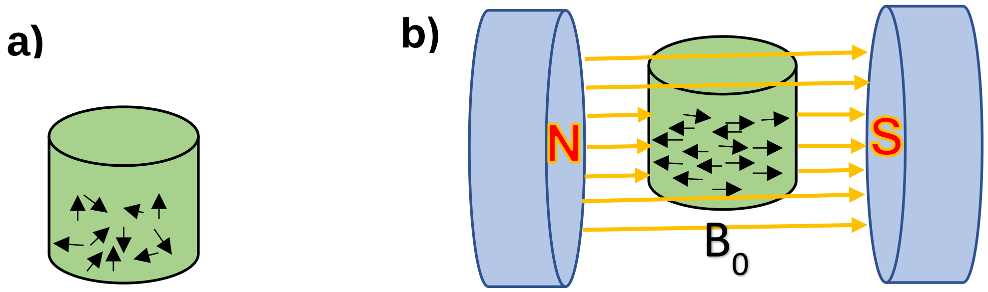

Figura 2.2 Orientación del spin de protones, a) sin influencia de campo magnético externo B_0, b) bajo influencia de un campo magnético externo B_0.

Sin embargo, no todos se alinean en la misma dirección; algunos lo hacen en dirección del campo magnético B_0 (estado de baja energía $N\uparrow$) y otros en contra (estado de alta energía $N\downarrow$) cancelándose mutuamente. Pero hay un pequeño exceso en el estado de baja energía tal que el vector de magnetización neta es en dirección de B_0 y a mayor intensidad del campo externo mayor será la diferencia de niveles y por lo tanto mayor el número de espines en exceso en dirección del campo (Figura 2.3). La diferencia de energía entre los niveles se calcula de $\Delta E = \gamma\hbar B_0$ donde γ es la relación giromagnética (relación del momento magnético entre el momento angular del núcleo) y $\hbar$ es la constante de Planck reducida. La diferencia de población entre los dos posibles estados sigue la distribución de Boltzmann (Ec. 2.1), donde k es la constante de Boltzmann y T es la temperatura en grados Kelvin (Blümich et al., 2014).

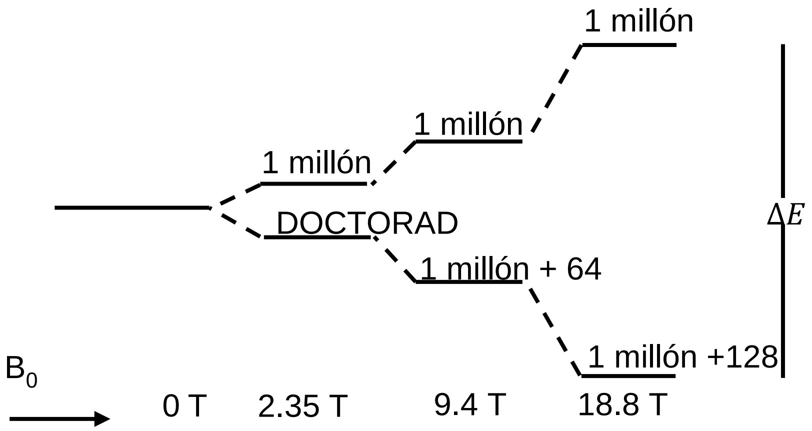

Figura 2.3 Distribución de 2 millones de protones a diferente intensidad de campo B_0 a 23 °C.

$$\frac{N\downarrow}{N\uparrow} = e^{-\frac{\Delta E}{kT}} \tag{2.1}$$

El hecho de que el núcleo tenga un momento angular hace que no pueda alinearse de manera perfecta con el campo magnético B_0, en cambio provoca que se comience un movimiento de precesión tomando como eje la dirección del campo B_0 (Brown et al., 2014) similar al movimiento de un trompo cuando empieza a tambalearse por la influencia del campo gravitatorio de la tierra (Figura 2.4). La frecuencia de precesión es directamente proporcional a la intensidad del campo magnético externo de acuerdo con la ecuación de Larmor (Ec. 2.2).

$$\omega = \gamma . B_0 \tag{2.2}$$

donde

ω es la frecuencia de Larmor (MHz),

γ es la relación giromagnética (MHz/Tesla), y

B_0 es el campo magnético estático (Tesla)

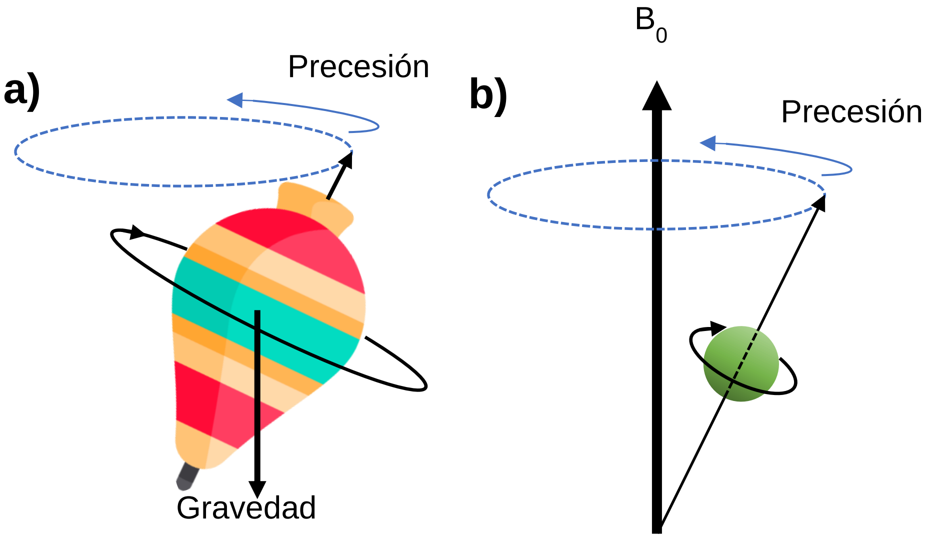

Figura 2.4 Movimiento de precesión de a) un trompo con momento angular bajo la influencia de la gravedad terrestre y b) un núcleo con spin I y momento magnético μ dentro de un campo magnético B_0 constante.

2.1.3 Excitación de los espines

Los protones pueden absorber energía si se les aplican pulsos de radiofrecuencia (RF) a una frecuencia igual a la frecuencia de Larmor. Lo que sucede a nivel cuántico es que un solo protón pasa del estado de baja energía a un estado de alta energía. A nivel macroscópico un observador ubicado en un marco de referencia estacionario puede observar un vector de magnetización M_0 rotando en el plano XY y formando un espiral (Figura 2.5a). En cambio, si el observador está situado en un marco de referencia rotatorio lo que puede ver es un vector de magnetización inclinarse suavemente hacia el plano XY (Figura 2.5b) con un ángulo α de inclinación que está en función de la intensidad y la duración del pulso de RF.

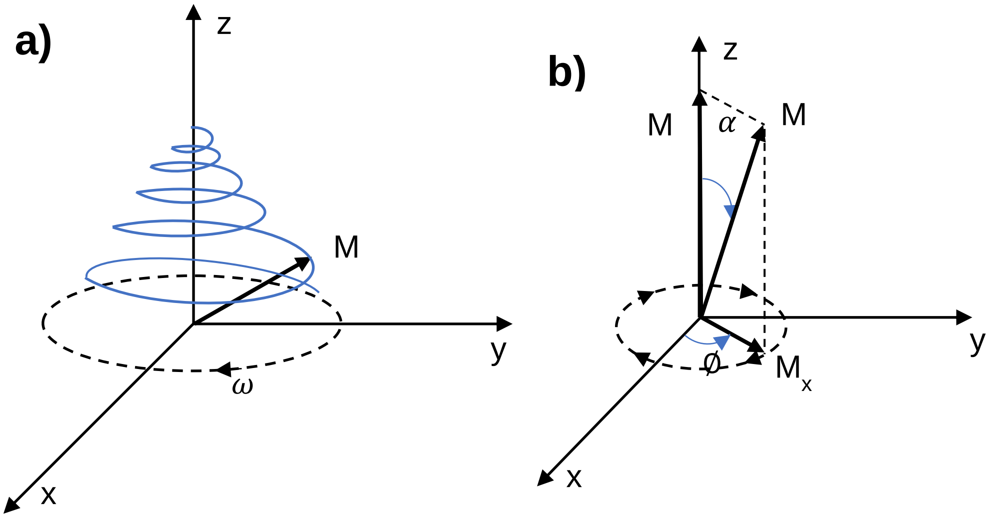

Figura 2.5 Absorción de la energía de RF a) Vector de magnetización visto desde un marco de referencia estacionario b) Vector de magnetización visto desde un sistema de referencia rotatorio.

Una vez que la transmisión del pulso de RF es interrumpida, la energía absorbida por los protones es retransmitida a la frecuencia ω, el vector M_0 regresa a su orientación inicial y los vectores de magnetización de los protones que habían entrado en fase comienzan a desfasarse.

Un vector de magnetización M_z que ha sido inclinado desde el eje Z continúa su movimiento de precesión alrededor de B_0 una vez que se ha interrumpido el pulso de RF. Puesto que es un campo magnético rotatorio es capaz de generar ondas de RF a una frecuencia ω que es captada por una antena sintonizada obteniéndose de esta forma la señal de RMN.

2.1.4 Tiempo de relajación spin-lattice (T_1)

T_1 es el tiempo que transcurre mientras el sistema regresa a su equilibrio térmico, o M_z tiende a M_0, la cual es descrita por una función de crecimiento exponencial (Figura 2.6). El vector de magnetización longitudinal recupera el 63.2% de su valor de equilibrio en el tiempo t= T_1 después del pulso de excitación. Este tipo de relajación sucede por la interacción de los núcleos y el medio circundante donde intervienen factores como núcleos no excitados y campos eléctricos.

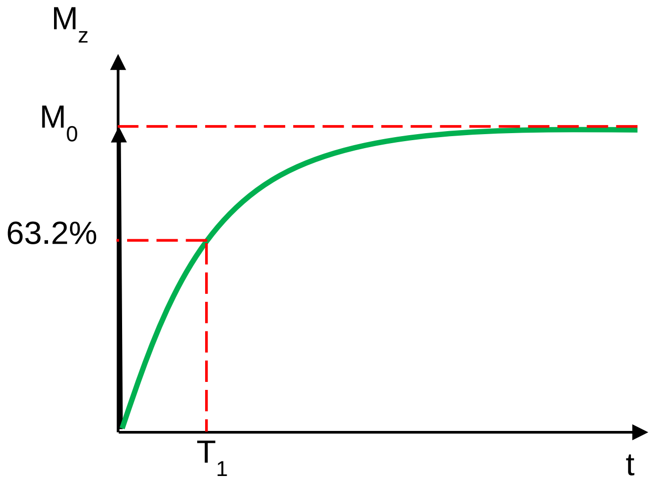

Fig. 2.6 Tiempo de relajación T_1.

La medición de T_1 se realiza usualmente con una secuencia de pulsos conocida como Inversión Recuperación (IR), la cual inicia con un pulso de 180° seguido de un pulso de 90°. El pulso de 180° invierte la magnetización longitudinal del eje +Z al eje -Z y después de un intervalo de tiempo τ se aplica el pulso de 90° que traslada la magnetización longitudinal al eje transversal para poder ser detectada. Una variación de τ permite monitorear la magnitud de la magnetización longitudinal en función de τ durante el proceso de recuperación al equilibrio térmico (Figura 2.7).

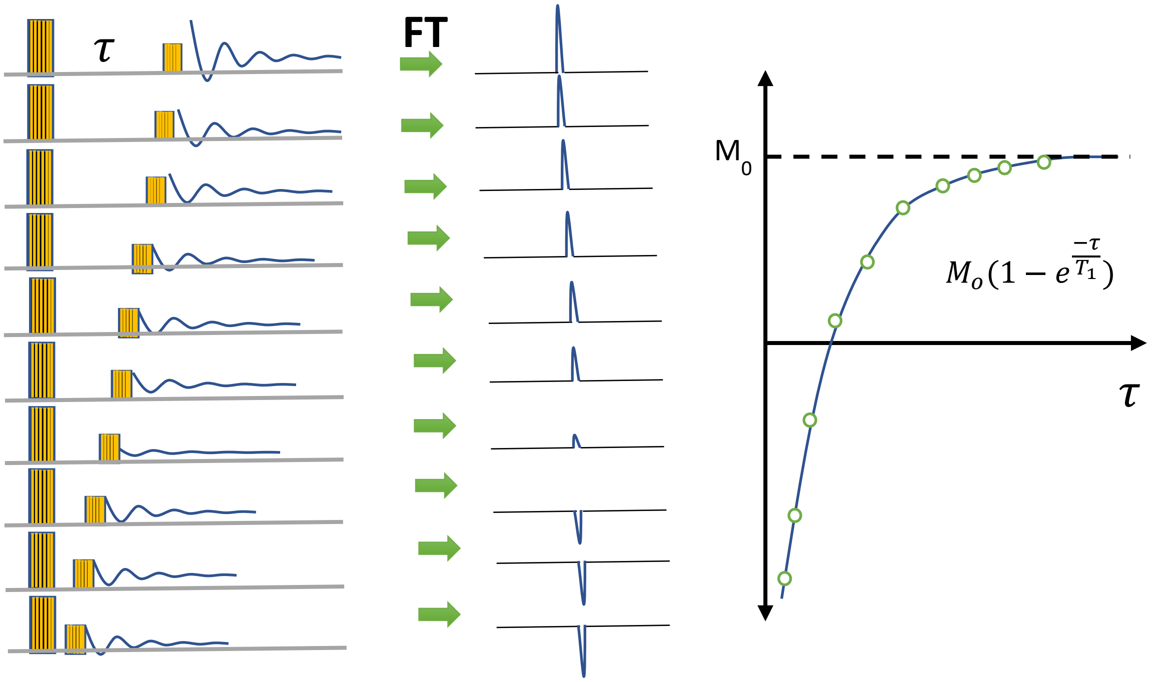

Figura 2.7 Secuencia inversión recuperación (IR) utilizada para la determinación del tiempo de relajación T_1.

2.1.5 Interacción spin-spin y tiempo de relajación T_2

La velocidad de precesión de un protón depende de la intensidad de campo magnético que experimenta, la cual puede variar ligeramente a causa de la interacción Spin-Spin. Esto se debe a que el campo magnético de cada protón interactúa con el campo magnético del protón vecino de tal manera que cuando ambos giran en la misma dirección hay una adición del campo magnético y, por el contrario, si tienen direcciones de giro opuestas hay una sustracción (Figura 2.8). Estas pequeñas variaciones provocan desfasamientos de los vectores de magnetización que precesan a diferentes velocidades pero que regresan rápidamente a la frecuencia original debido a que los protones se encuentran en constante movimiento.

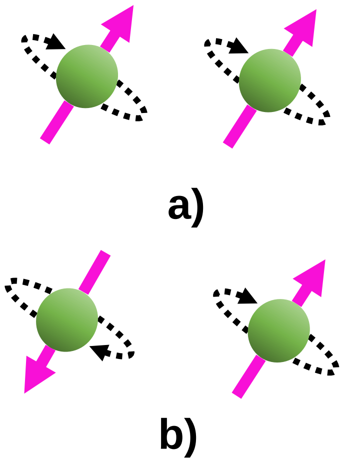

Figura 2.8 Interacción spin-spin a) adición de campo magnético y b) sustracción de campo magnético.

El valor de T_2 es el tiempo que transcurre después del pulso de excitación en que la componente transversal de la magnetización se reduce a 36.8% de su valor original. El decaimiento de la señal está descrito por una curva de decaimiento exponencial (Figura 2.9).

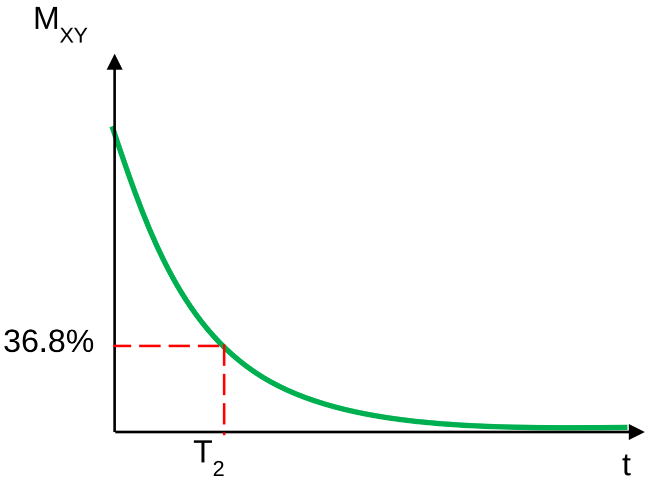

Figura 2.9 Tiempo de relajación T_2.

La técnica ampliamente utilizada para medir el tiempo de relajación spin-spin T_2 es la Carr-Purcell-Meiboom-Gill (CPMG) (Meiboom & Gill, 1958). Consiste en una secuencia de pulsos que inicia con un pulso de 90° seguido por una serie de pulsos de 180º. Los dos primeros pulsos están separados por un período de tiempo τ, mientras que los pulsos restantes son separados por 2τ. Los ecos ocurren a la mitad del tiempo entre pulsos de 180º en 2τ, 4τ, . . . 2τxn, donde n es el número de eco. TE significa el espacio entre eco y es igual a 2τ (Figura 2.10).

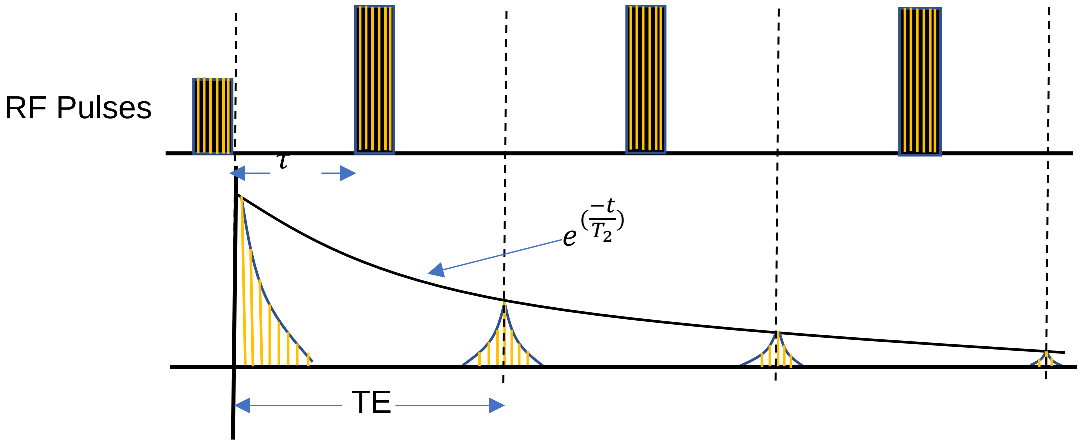

Figura 2.10 Secuencia CPMG utilizada para la determinación del tiempo de relajación T_2.

2.2 Mecanismos de relajación de fluidos en medios porosos

Existen tres mecanismos de relajación de un fluido dentro de los poros de un material poroso, como en el caso de las rocas o el concreto: procesos de relajación global, proceso de relajación por superficie y proceso de relajación por difusión en presencia de gradientes de campo magnético (Coates, Xiao, & Prammer, 1999). El tiempo de relajación transversal T_2 es afectado por los tres mecanismos (Ec.2.3) mientras que al tiempo de relajación T_1 solo es afectado por el mecanismo de relajación de fluido libre y el mecanismo de relajación por superficie (Ec.2.4).

$$\frac{1}{T_2} = \frac{1}{T_{2\,global}} + \frac{1}{T_{2\,superficie}} + \frac{1}{T_{2\,difusión}} \tag{2.3}$$

$$\frac{1}{T_1} = \frac{1}{T_{2\,global}} + \frac{1}{T_{2\,superficie}} \tag{2.4}$$

2.2.1 Mecanismo de relajación de fluido libre

Es la propiedad de relajación intrínseca de un fluido, el cual es controlada por las propiedades físicas del fluido, tales como viscosidad y composición química. Al estar el líquido en un recipiente grande se elimina la relajación de superficie y al ser sometido a un campo homogéneo se elimina la relajación por difusión. Otras condiciones ambientales tales como la temperatura y la presión también afectan a la relajación global de un fluido (Coates et al., 1999). El tiempo de relajación global para el agua está determinado por la ecuación 2.5 y 2.6 para T_1 y T_2 respectivamente.

$$T_{1global} \cong 3\left(\frac{T_K}{298\eta}\right) \tag{2.5}$$

$$T_{2global} \cong T_{1global} \tag{2.6}$$

donde

T_K es la temperatura (°K)

η es la viscosidad (cp)

2.2.2 Mecanismo de relajación por superficie

La relajación por superficie se produce en la interfaz sólido-liquido, el cual es el factor dominante para los tiempos de relajación en lo que se conoce como régimen de difusión rápida(Coates et al., 1999). Este término viene dado para T_1 y T_2 por las ecuaciones 2.7 y 2.8, respectivamente.

$$\frac{1}{T_{2\,superficie}} = \rho_2\left(\frac{S}{V}\right)_{poro} \tag{2.7}$$

$$\frac{1}{T_{1\,surperficie}} = \rho_1\left(\frac{S}{V}\right)_{poro} \tag{2.8}$$

donde

ρ_2 es la relaxividad T_2 de la superficie (fuerza relajante T_2 de las superficies de los poros)

ρ_1 es la relaxividad T_1 de la superficie (fuerza relajante T_1 de las superficies de los poros)

$\left(\frac{S}{V}\right)_{poro}$ es la relación entre la superficie y el volumen del sistema poroso que contiene al fluido

2.2.3 Relajación por difusión

Este proceso de relajación ocurre cuando el fluido se encuentra en un gradiente significativo de campo magnético y se somete a una secuencia CPMG con espaciamiento de tiempo inter-eco. El movimiento de la molécula de una región a otra donde la intensidad de campo magnético es diferente, y por consiguiente en el que la tasa de precesión es diferente, provoca desfase adicional aumentando así la tasa de relajación $1/T_2$ (Coates et al., 1999). Por otra parte, la difusión no tiene influencia en la velocidad de relajación T_1 ($1/T_1$). La velocidad de relajación inducida por difusión ($1/T_{2difusión}$) se calcula con la ecuación 2.9.

$$\frac{1}{T_{2\,difusión}} = \frac{D(\gamma G TE)^2}{12} \tag{2.9}$$

donde

D es el coeficiente de difusión molecular

γ es la relación giromagnética de un protón

G es el gradiente de intensidad de campo

TE es el espaciamiento inter-eco utilizado en la secuencia CPMG

Este proceso de relajación al igual que la relajación global, es afectado por las propiedades físicas del fluido como la viscosidad, la composición molecular y la temperatura. En caso del agua, el coeficiente de difusión (D_w) viene dado por la Ecuación 2.10.

$$D_w \cong 1.2 \left(\frac{T_K}{298\eta}\right) x10^{-5} cm^2/s \qquad (2.10)$$

Donde T_k es la temperatura en grados Kelvin

2.2.4 Naturaleza multi-exponencial del decaimiento de la señal y su relación con la distribución de tamaño de poro

En un material poroso por lo general existe una distribución de tamaño de poro, de tal manera que la señal de decaimiento de la magnetización transversal obtenido con una secuencia CPMG no está compuesta por un solo valor de T_2 sino por una distribución de T_2 (Coates et al., 1999). Esto se puede describir con la Ecuación 2.11.

$$M(t) = \sum M_i(0) e^{\frac{-t}{T_{2i}}} \qquad (2.11)$$

donde

M (t) es la magnetización en función del tiempo t

M_i (0) es la magnetización inicial de la i-ésima componente de relajación

T_{2i} es la constante de decaimiento de la i-ésima componente de la relajación transversal.

Como se mencionó anteriormente, la relajación de superficie es predominante en el régimen de difusión rápida donde el tiempo inter-eco utilizado es corto. Bajo esta condición, T_2 es directamente proporcional al tamaño de poro (Coates et al., 1999). Por lo tanto, asumiendo que todos los poros tienen la misma forma, para poblaciones de poros grandes el decaimiento de la señal será lento (la relación $\frac{S}{V}$ es baja) en cambio para poblaciones de poros pequeños el decaimiento de la señal será más rápido (la relación $\frac{S}{V}$ es alta).

La naturaleza del decaimiento multi-exponencial de un material poroso donde existen diferentes tamaños de poro conteniendo un solo tipo de fluido se puede comprender mejor analizando la Figura 2.11. En la parte superior izquierda de esta figura se tiene un poro 100% saturado con agua, el cual tiene valor único T_2 (centro superior) que depende del tamaño del poro, y por lo tanto su tren CPMG exhibe un decaimiento exponencial simple (superior derecha) que también depende del tamaño de poro. En la parte inferior izquierda se observan poros de diferente tamaño 100% saturados con agua, con lo cual se tiene múltiples valores de T_2 (centro inferior), por lo que su tren CPMG exhibe un decaimiento multi-exponencial (inferior a la derecha), que también depende de los tamaños de poro.

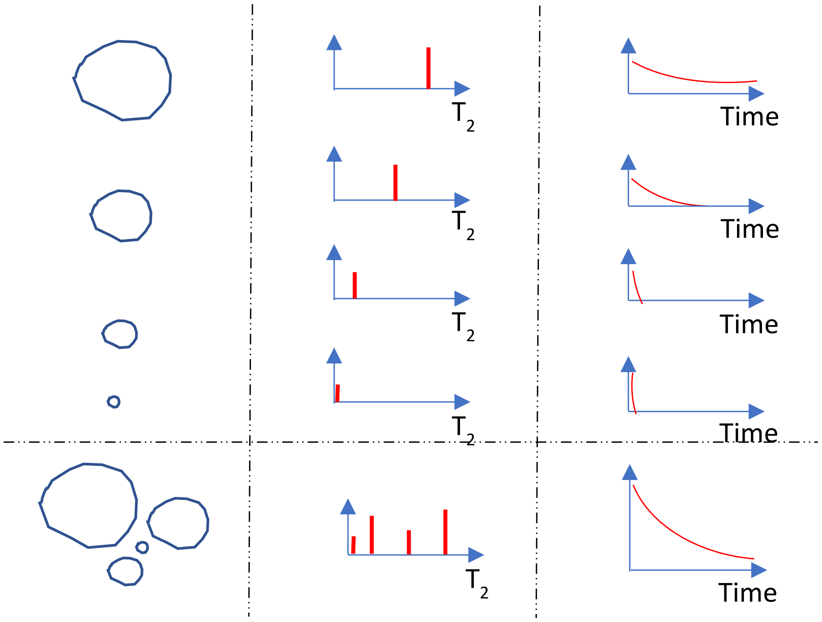

Figura 2.11 Naturaleza de decaimiento multi-exponencial de un medio poroso que contiene un solo tipo de fluido y poros de diferentes tamaños (Coates et al., 1999).

Dado que el valor T_2 de un poro es proporcional a la relación superficie / volumen del sistema poroso, la distribución T_2 observada representa la distribución del tamaño de poro en un material. Para determinar la distribución de T_2 que produce una señal de decaimiento de la magnetización transversal es necesario realizar un ajuste o mapeo. Este proceso es una inversión matemática basada en la transformada inversa de Laplace (ILT) (Borgia, Brown, & Fantazzini, 1998). Un ejemplo se muestra en la Figura 2.12 donde se compara la distribución de T_2 de una roca, saturada con solución salina, con la distribución de tamaño de poro obtenida con la técnica de intrusión de mercurio. Como se observa existe una notable correlación de la distribución de T_2 con la distribución de tamaño de poro.

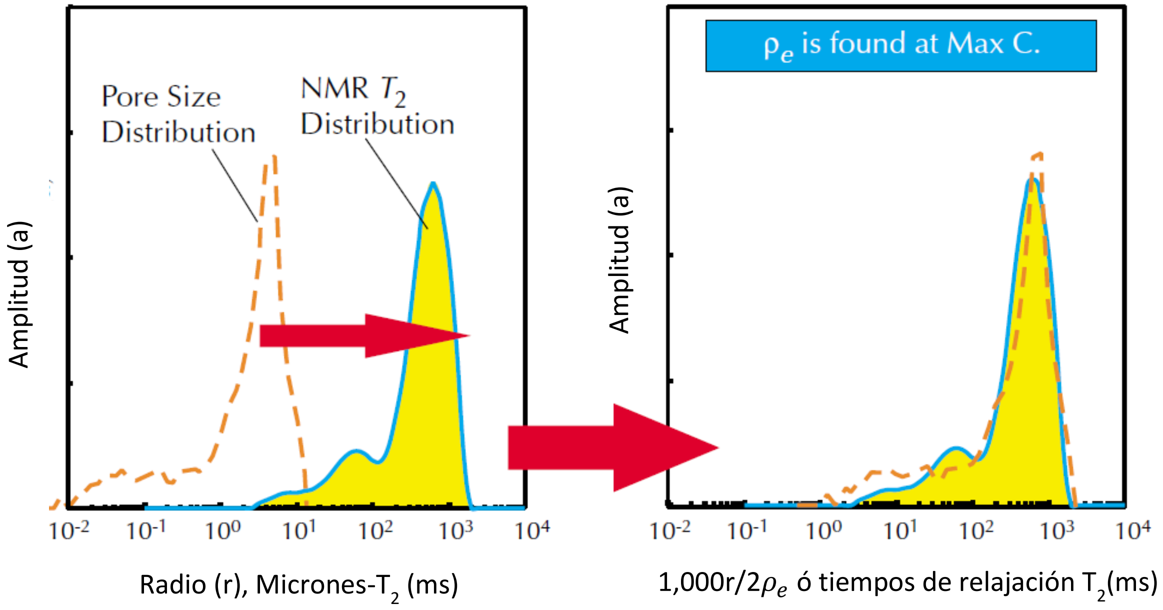

Figura 2.12 Comparación de la distribución de T_2 con la distribución de tamaño de poro determinada con la técnica de intrusión de mercurio (Coates et al., 1999).

2.3 Referencias

Blümich, B., Sabina, H., & Zia, W. (2014). *COMPACT NMR*. Berlin: Walter de Gruyter GmbH.

Borgia, G. C., Brown, R. J. S., & Fantazzini, P. (1998). Uniform-Penalty Inversion of Multiexponential Decay Data. *Journal of Magnetic Resonance*, *132*(1), 65–77. https://doi.org/10.1006/jmre.1998.1387

Brown, R. W., Cheng, Y.-C. N., Haacke, E. M., Thompson, M. R., & Venkatesan, R. (2014). *MRI Physical Principles and Sequence Design*. (J. and sons Wiley, Ed.), *Journal of Chemical Information and Modeling* (Second edi, Vol. 53). Hoboken, New Jersey: John Wiley and sons. https://doi.org/10.1017/CBO9781107415324.004

Coates, G. R., Xiao, L., & Prammer, M. G. (1999). *NMR Logging principles & applications*. (R. F. Sigal & S. J. Bollich, Eds.). Houston, Texas, USA: Halliburton Energy Services.

Fukushima, E., & B.W. Roeder, S. (1981). *Experimental pulse NMR a nuts and bolts aproach*. Reading, Massachusetts, U.S.A.: Addison-Wesley.

Macomber, R. S., & Harbison, G. S. (1997). *A Complete Introduction to Modern NMR Spectroscopy*. *Physics Today*. New York, NY: John Wiley & Sons. https://doi.org/10.1063/1.882558

Meiboom, S., & Gill, D. (1958). Modified spin-echo method for measuring nuclear relaxation times. *Review of Scientific Instruments*, *29*, 688–691.

Capítulo 3. Unilateral low-field magnetic resonance measurements of carbonation depth in unsaturated and saturated Portland cement mortars

Abstract

Unilateral Nuclear Magnetic Resonance is used to characterize the carbonation depth in 0.60 w/c ratio unsaturated/saturated Portland cement mortars. A three-magnet array combined with a surface elliptical coil was utilized to obtain the Nuclear Magnetic Resonance signal at different positions along mortar samples. The T_2 lifetime and signal intensity behaviors in the carbonated and non-carbonated zones were analyzed. Scanning Electron Microscopy images were used to identify the macro-porosity and micro-cracking in the samples. Results confirmed that the crossover point between profiles of T_2 lifetime and signal intensity agree with the carbonation depth obtained by the phenolphthalein test. The carbonation depth at the position where the T_2 lifetime begins to behave nearly constant is about 1.44 times the depth indicated by the phenolphthalein test. The spatial resolution was improved four times in comparison with previous research. Scanning Electron Microscopy images analysis confirmed a significant decrease in local porosity and crack area in the carbonated zone.

Keywords: *carbonation depth, unilateral NMR, mortar, T_2 lifetime, signal intensity, pore size distribution*

3.1. Introduction

Carbonation is one of the major causes of steel corrosion in reinforced concrete structures (Zhou, Gencturk, Willam, & Attar, 2015). The CO_2 penetrating through the concrete cover dissolves in the pore solution and the carbonic acid formed reacts with the hydrated cement. From the hydrated products, calcium hydroxide reacts with the carbonic acid producing calcium carbonate and water. This carbonation process reduces the pH of the pore solution from typical values of 12-13 to less than 9 (Mehta & Monteiro, 2006). Also, carbonation produces changes in the porosity and pore size distribution of the hydrated cement paste (Bier, Kropp, & Hilsdorf, 1989; Pihlajavaara, 1968). Regarding the carbonation of C-S-H, a silica gel with a coarse pore structure is produced (Bier et al., 1989). When the carbonation depth reaches the level of the reinforcing steel, the passive layer that protects the steel is destroyed and corrosion may start.

There are several destructive and non-destructive techniques to determine the carbonation depth in concrete. One of the destructive techniques consists of spraying a 1 % phenolphthalein solution on a freshly broken concrete surface. However, this technique underestimates the carbonation depth by about 50 % (Chang & Chen, 2006; Pacheco Torgal, Miraldo, Labrincha, & De Brito, 2012) in comparison with the depth obtained by other destructive techniques such as Thermo Gravimetric Analysis (TGA), X-Ray Diffraction (XRD) and Fourier Transform Infrared Spectroscopy (FTIR), used on powder samples obtained at different depths of the sample. These techniques allowed identification of three zones related to carbonation: carbonated, transition or partially carbonated and non-carbonated (Chang & Chen, 2006). Since all of these techniques are destructive, it is necessary to explore the use of non-destructive techniques to determine the depth of carbonation in cement-based materials.

Nuclear Magnetic Resonance (NMR) is a non-destructive technique that has been used to study Portland cement hydration (Miljkovic et al., 1988), moisture transport in heated concrete (van der Heijden, van Bijnen, Pel, & Huinink, 2007), chloride and sodium ions penetration profiles (Cano, Bremner, Mcgregor, & Balcom, 2002), moisture content profiles during drying (Cano-Barrita, Balcom, Bremner, MacMillan, & Langley, 2004) and during water absorption (Enjilela, Cano-Barrita, Komar, Boyd, & Balcom, 2018), as well as refinement of porosity and compressive strength development (Díaz-Díaz, Cano-Barrita, Balcom, Solís-Nájera, & Rodríguez, 2013). The carbonation depth has been successfully identified using unilateral magnetic resonance, by measuring NMR T_2 lifetime and signal intensity variations along vacuum saturated Portland cement paste samples subjected to accelerated carbonation (Cano-Barrita, Balcom, & Castellanos, 2017). It was found that there is an increase in the long T_2 lifetime component and also a decrease in the signal intensity in the carbonated zone compared with the non-carbonated one. The position with the highest rate of these changes agreed with the carbonation depth determined by the phenolphthalein test. Given the characteristics of the surface circular radio frequency (RF) coil used, the measurements were undertaken by moving the sample in steps of 1 cm, which was a limitation when the carbonation depth was less than 1 cm.

Evaluation of the carbonation depth in unsaturated samples is desirable, as it would allow time-based carbonation studies on the same sample. However, unsaturated Portland cement mortars are challenging to evaluate due to a low NMR signal intensity, since the main source of the NMR signal in the mortar is the evaporable water from cement paste. A better spatial resolution than the previous study (Cano-Barrita et al., 2017) will permit the measurement of samples with low permeability or samples with high permeability but short exposure times that may have carbonation depths of only a few millimeters. For instance, the carbonation depth in concrete with $w/c = 0.60$ is 15 mm after 15 years, whereas for concrete with $w/c \leq 0.45$, the same carbonation depth will take 100 years to occur (Pacheco Torgal et al., 2012).

The present research aimed to improve application of the unilateral NMR measurements to detect the carbonation depth in unsaturated and saturated

Portland cement mortars, by using a three-magnet array with an elliptical surface RF coil, validating the NMR carbonation depth results with the phenolphthalein test and the carbonation depth reported in the literature using other destructive techniques, and relating the NMR T_2 lifetimes with the microstructure observed in Scanning Electron Microscopy images (SEM).

3.2. Materials and method

3.2.1 Materials

Ordinary Portland cement (OPC) and class F fly ash (FA) with a chemical composition given in Table A.1 in the Appendix, were used. Silica sand with a fineness modulus of 2.79, density of 2.62, and absorption of 0.26 % was used as fine aggregate. Two mortar mixtures at 0.60 w/c ratio by weight were prepared with a cement to sand ratio by weight = 0.50. One mortar was prepared with 100 % OPC and another had 80 % OPC + 20 % FA. The pozzolanic reaction of FA reduces the availability of calcium hydroxide, and carbonation may also attack the C-S-H (Johannesson & Utgenannt, 2001). To ensure a useful NMR signal that comes from the pore water in the hydrated cement paste, these mortars were prepared with a higher cement paste volume per 1 m^3 (0.54 m^3) than those mortars (about 0.43 m^3) recommended by standards such as ISO 679:2009 or ASTM C109 (ASTM C109M-16a, 2016) for compressive and flexural strength testing. The Portland cement, silica sand, and water were mixed according to the standard ASTM C305 (ASTM C305, 2014).

3.2.2 Sample preparation and accelerated carbonation

Cylindrical molds measuring 4.2 cm in diameter and 5 cm in length were used to cast mortar samples in triplicate for each mixture. After 24 hours, the mortar samples were removed from the molds and moist cured in saturated limewater for 60 days at 23 °C. The curing time was chosen to allow for the pozzolanic reaction of FA to progress. After curing, the samples were conditioned at 65 % relative humidity and 35 °C until constant mass.

Once the mortar samples reached constant mass conditions under 65 % RH and 35 ^{o}C, the sample's surface was coated with an epoxy resin, except for one circular face. When the resin hardened, the samples were exposed to a 4 % by volume CO_2 environment at 65 % relative humidity and 35 °C for six months. An OPC + 20 % FA mortar sample was left in the carbonation chamber for about two years. The carbonation conditions were selected to be consistent with previous research (Cano-Barrita et al., 2017). Control samples were kept sealed in polyethylene bags at 35 ^{o}C (without exposition to CO_2).

3.2.3 Three-magnet array and RF coil

A unilateral three-magnet array (Garcia-Naranjo, 2012) that generates a relatively homogeneous magnetic field of 109 mT in a volume displaced 0.9 cm from the top of the magnets, was used (Figure A.1). This volume corresponds to an idealized rectangular prism of approximate dimensions 1.0 cm in width (along Z-axis) × 2.0 cm in length (along X-axis) × 1.0 cm in height (along Y-axis). The direction of the B_0 field is along Z-axis.

An elliptical surface RF coil (Figure 3.1 and Figure A.2 in the Appendix) measuring 0.3 cm and 4.4 cm of minor and major internal diameters, respectively, was built using 0.3 cm wide copper sheet. The elliptical shape was chosen because the minor internal diameter could be oriented parallel to the longitudinal axis of the sample and excite a thinner region of the sample to improve the spatial resolution, compared with the circular surface RF coil used in previous research (Cano-Barrita et al., 2017). The RF coil was tuned to 4.64 MHz that corresponds to the B_0 field of 109 mT produced by the three-magnet array. A Faraday cage was used to reduce the adverse effects of external noise on the NMR signal.

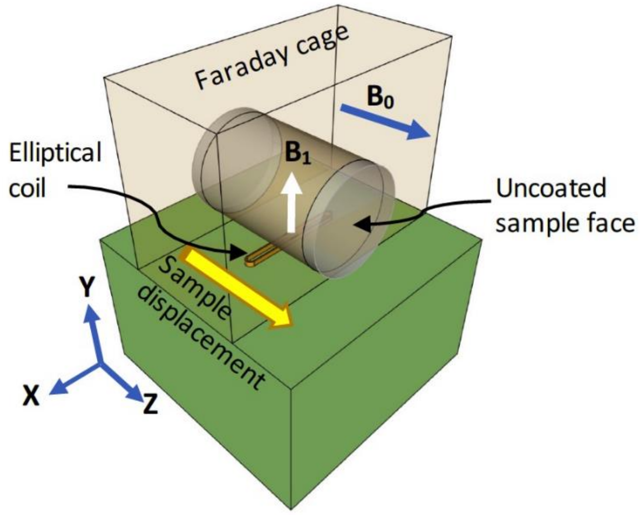

Figure 3.1 Elliptical surface RF coil position on the three-magnet array. The coil, with a quality factor Q of 22, generates the B_1 field perpendicular to the longitudinal axis of the sample. The minor axis of the ellipse is parallel to the sample displacement direction, to excite a thin region of the sample.

3.2.4 NMR measurements

3.2.4.1 Distance of influence of the RF coil

To determine the distance of influence of the coil, an eraser with 0.25 cm in thickness (oriented parallel to the sample displacement), 2.5 cm in height and 1.2 cm width was used (Figure 3.2a). The eraser was selected because it has a homogeneous composition with a constant signal intensity over the duration of the experiment, and its relatively short T_2 lifetime (≈ 6.9 ms), which is in the order of magnitude of the T_2 lifetime of water in the mortars. The center of the eraser was displaced starting from the center of the coil in steps of 0.25 cm, undertaking a CPMG measurement (Meiboom & Gill, 1958) at each position. Subsequently, a phantom consisting of two eraser samples with dimensions of 1 cm in length, 2.5 cm in height and 1.2 cm in width, separated 1.5 cm was used (Figure 3.2b). The phantom was displaced also in steps of 0.25 cm above the center of the coil and a CPMG measurement was undertaken at each position to determine the ability of the device to replicate the shape of the phantom through the signal intensity profile. The three-magnet array with the RF coil only measures a small volume along the Y-axis in the eraser slice and in the eraser phantom.

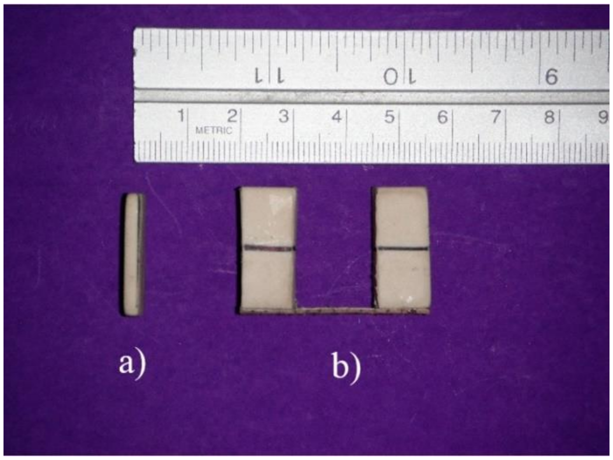

Figure 3.2 Eraser samples used to characterize the distance of influence of the RF coil, a) Eraser slice, and b) Phantom consisting of two separated eraser samples.

All NMR experiments with the three-magnet array were performed using a Kea[2] spectrometer (Magritek Limited, Wellington, New Zealand). The parameters used for the CPMG measurements are given in Table 3.1. The signal intensity at time zero (M_0) and the T_2 lifetime at each point were obtained by fitting the transverse magnetization decay to a single exponential decay function (Eq. 3.1).

$$S(t) = M_0 e^{\left(-\frac{t}{T_2}\right)} \tag{3.1}$$

where S is the signal intensity, t is time, M_0 is the equilibrium sample magnetization, and T_2 is the lifetime decay constant.

Table 3.1 Parameters for the CPMG measurements undertaken on eraser samples and mortars. The echo time and the number of echoes were chosen to cover the full CPMG decay of each material tested. The faster decay of the signals in the mortars required to reduce the echo time to capture signal from both the fast and the slow relaxing spins.

	Eraser samples	Mortars	
Pulse width (μs)	10	10	10
Number of echoes	512	128	128
Echo time (μs)	300	130	80
Number of scans	1024	16384	16384
Acquisition time (min)	15	100	100

3.2.4.2 NMR measurements on carbonated mortar samples

NMR measurements were undertaken on mortar samples with the CPMG technique (Meiboom & Gill, 1958) at carbonation ages of six months and two years. At six months, the carbonated and control OPC and the OPC + 20 % FA samples were water saturated under a pressure of 50 mm Hg (6.7 kPa) for three hours and then kept immersed in water for 18 more hours. This conditioning of the samples filled all the porosity to reveal the actual microstructural changes caused by carbonation (Cano-Barrita et al., 2017). After two years of carbonation, other NMR measurements were undertaken in an OPC + 20 % FA mortar sample under two moisture conditions: unsaturated and saturated. The first measurements were on the unsaturated sample at equilibrium with the environmental conditions used during the carbonation process. This was done to explore differences between the two zones without disturbing the carbonation process by the water vacuum saturation. Then the mortar sample was vacuum-saturated, and the NMR measurements were repeated.

In all cases, the samples were displaced in steps of 0.25 cm on the surface of the elliptical coil (Figure 3.1). The parameters for the CPMG measurements are given in

Table 3.1. To obtain the short and long T_2 lifetime components and their associated signal intensities, the CPMG decays obtained at each position along the samples were fitted to a bi-exponential decay function (Eq. 3.2).

$$S(t) = M_{0,1}e^{\left(-\frac{t}{T_{2,1}}\right)} + M_{0,2}e^{\left(-\frac{t}{T_{2,2}}\right)} \qquad (3.2)$$

where S is the signal intensity (proportional to the water content in the sample), t is time, $M_{0,1}$ and $M_{0,2}$ are the equilibrium sample magnetization components corresponding to the $T_{2,1}$ and $T_{2,2}$ lifetime constants (related to the pore sizes in the cement paste). The T_2 lifetime constants in hydrated Portland cement pastes are associated with water in gel pores (short T_2 lifetime component) and water in capillary pores (long T_2 lifetime component) (Jehng, Sprague, & Halperin, 1996).

3.2.5. Phenolphthalein test

After the NMR measurements were undertaken, the samples were broken longitudinally, and a 1 % phenolphthalein solution was immediately sprayed on the broken surface to reveal the carbonation depth (RILEM Recommendations CPC-18, 1988). Four measurements of the carbonation depth in each sample were performed using a caliper, and the average depth was reported.

3.2.6 Gravimetric porosity

The gravimetric porosity of carbonated and non-carbonated zones of the samples was determined according to the ASTM C642 (ASTM C 642-13, 2013). Vacuum saturation was preferred to saturate the samples with water because it is more efficient to measure the permeable porosity in comparison with immersion in water and boiling that preferentially fill the smaller pores (Bu, Spragg, & Weiss, 2014; Safiuddin & Hearn, 2005). The vacuum saturation conditions were the same as those described in section 2.4.2. The oven-dry mass was found after obtaining the saturated surface-dry mass and the buoyant mass, to avoid generating additional permeable porosity due to microcracking.

3.2.7 SEM studies and image analysis of the capillary macro-porosity

Partially carbonated mortar samples of approximately 2 cm × 2 cm × 0.6 cm were obtained for SEM studies by cutting the original mortar samples. The samples were conditioned, prepared and polished following the procedure given in the literature (Winnefeld, Scholer, & Lothenbach, 2016). The polished samples were coated with a ~30 nm gold layer using a sputter Desk V (Denton Vacuum, NJ, USA). A tungsten JSM-IT300LV scanning electron microscope (JEOL Ltd, Akishima, Japan) was used to obtain a total of 20 images (1764 × 1320 pixels) at 100× magnification with the back-scattered electron detector. These images, with a spatial resolution of 0.88 μm/pixel and a total area of ~ 36 mm^2 (9 % of the sample size area of 400 mm^2), were used to estimate the porosity and cracking area. Also, images at 1000× magnification were obtained to observe microstructural changes.

Capillary macro porosity analysis (Elia, Nativ-Roth, Zeiri, & Porat, 2016; Rimmelé, Barlet-Gouédard, Porcherie, Goffé, & Brunet, 2008; Tovey & Hounslow, 1995; Ziel, Haus, & Tulke, 2008) of the SEM images was done with the ImageJ version 1.46 software. The output of the program provided the Feret's diameter, as well as the area and circularity of the pores. The data were filtered based on a circularity criterion to separate the pores and micro-cracks. Pores were considered having the circularity in the range between 0.46 and 1 (1 corresponds to a perfect circle). Circularity < 046 was considered as crack. The voids percentage, corresponding to capillary pores and microcracks, was calculated in the carbonated and non-carbonated zones. The local porosity was obtained considering the pore area in comparison with the total area of the image.

3.3. Results and discussion

3.3.1 Distance of influence of the rf coil

The CPMG signal intensity profile obtained by moving the thin eraser slice is shown in Figure 3.3. Moving the center of the eraser by 0.25 cm to each side from the center of the coil causes about 45 % signal intensity loss. This means that using a 0.25 cm step size, some signals coming from adjacent zones contribute to the total signal observed at the position of interest. Placing the eraser at 0.50 cm from the center of the coil, produces no signal. Therefore, only sample within a distance less than 0.5 cm from each side of the coil contributes to the detected signal.

The signal to noise ratio (SNR) of the CPMG decays from the eraser slice located at the center of the coil, was 21. However, in spite of the low SNR and considering the 0.25 cm step size movement, there is four times improvement of spatial resolution compared with the circular surface coil used in previous research (Cano-Barrita et al., 2017), where the step movement was 1 cm. The latter precluded the measurement of samples with low permeability or samples with high permeability but short exposure times that may have shallow carbonation depths.

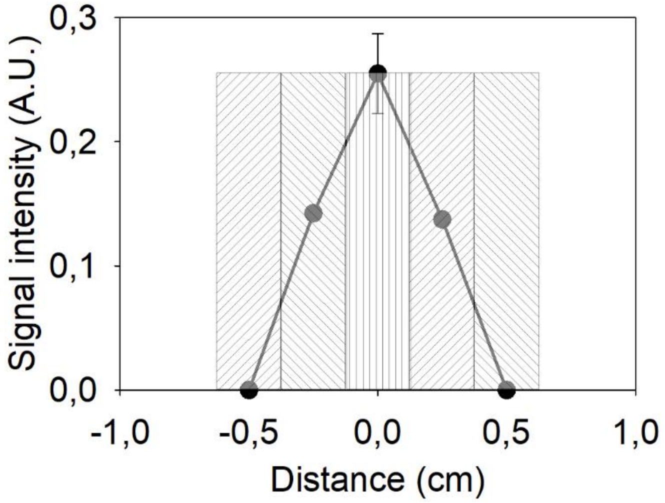

Figure 3.3 Signal intensity of the eraser slice versus distance with respect to the center of the coil (0 cm). The sample used was a thin eraser 0.25 cm in thickness, 2.5 cm in height and 1.2 cm width (Figure 2a). The shaded rectangles represent the thickness of the eraser slice at each position.

Figure 3.4 shows that the normalized CPMG signal intensity profile of the eraser phantom resembles the actual shape of the phantom (Figure 3.2b). These results indicated that the three-magnet array with the elliptical coil provided a more or less reliable indication of the proton distribution in the sample. Furthermore, this device would not have any restriction on the sample size, since the Faraday cage can be easily removed to test larger samples.

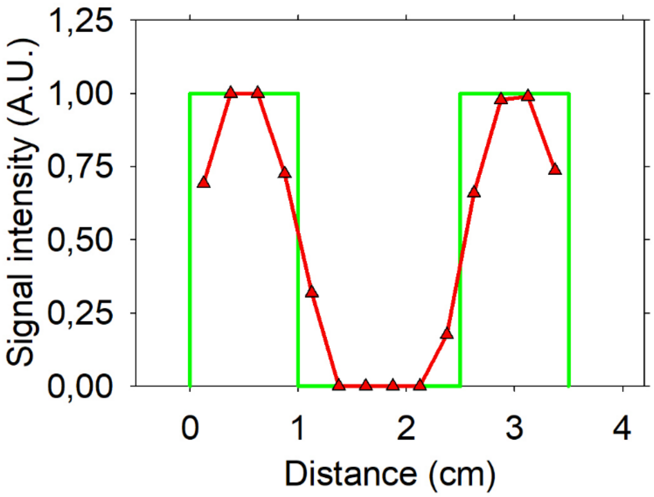

Figure 3.4 Comparison of the normalized CPMG intensity profile (triangles) with the actual shape of the eraser phantom (solid line) shown in Figure 2b.

3.3.2 Carbonation depth from measurements with the three-magnet array and the surface elliptical rf coil

Figure 2.5 shows normalized typical CPMG decays in carbonated and non-carbonated zones of 0.6 w/c ratio unsaturated and vacuum saturated mortar samples, and their corresponding T_2 lifetime distribution obtained by inverse Laplace transformation (ILT) of the CPMG decays. Fitting Eq. 3.2 or using the ILT are two different ways of processing the CPMG decays. Fitting Eq. 3.2 extracts the amplitudes of the signal and their corresponding relaxation times, whereas the ILT gives the distribution of relaxation times, which is a proxy of the pore size distribution. In the unsaturated sample (Figure 3.5a) the signals decayed bi-exponentially. There is a clear difference between the signal decays in the carbonated and non-carbonated zones, outperforming the results from previous work where differences were not observable (Cano-Barrita et al., 2017). This finding means that it will be possible to undertake CPMG measurements over time on the same sample to follow the progression of the carbonation depth in a non-destructive and non-invasive way. The ILT of the decays are shown in Figure 3.5b, revealing two pore populations. In the T_2 distribution corresponding to the non-carbonated zone, the first population comprising interlayer and gel water (T_2 values in the order of 0.1 ms) has a much higher signal intensity than the second population of about 0.4 ms. This is supported by the Kelvin equation, which indicates that pores with a radius smaller than 2.3 nm would be filled with water at 65 % RH and 35 ^{o}C. The T_2 distribution in the carbonated zone shows a significant reduction in the intensity of the first population of pores, which is related to the degradation of the C-S-H that produces a silica gel with coarse pore structure (Bier et al., 1989), which seems to appear on the second population of pores.

The same mortar sample now vacuum saturated with water (Figure 3.5c), where all the pores are filled, provides signals with similar bi-exponential behavior to that shown in Figure 3.5a for the unsaturated sample. The T_2 lifetime distributions in Figure 3.5d exhibit a better definition of the two pore populations than Figure 3.5b. The first pore populations are found below 0.7 ms, while the second ones are above 0.7 ms. The effects of coarsening of the C-S-H pore structure and the changes in surface relaxivity in the carbonated zone (Cano-Barrita et al., 2017) are observed as a shifting of the T_2 lifetimes distributions towards longer times (Figure 3.5d). Fitting Eq. 3.2 to the CPMG decay, results in short and long T_2 components that are related to the first and second population of pores in the T_2 lifetime distributions, respectively.

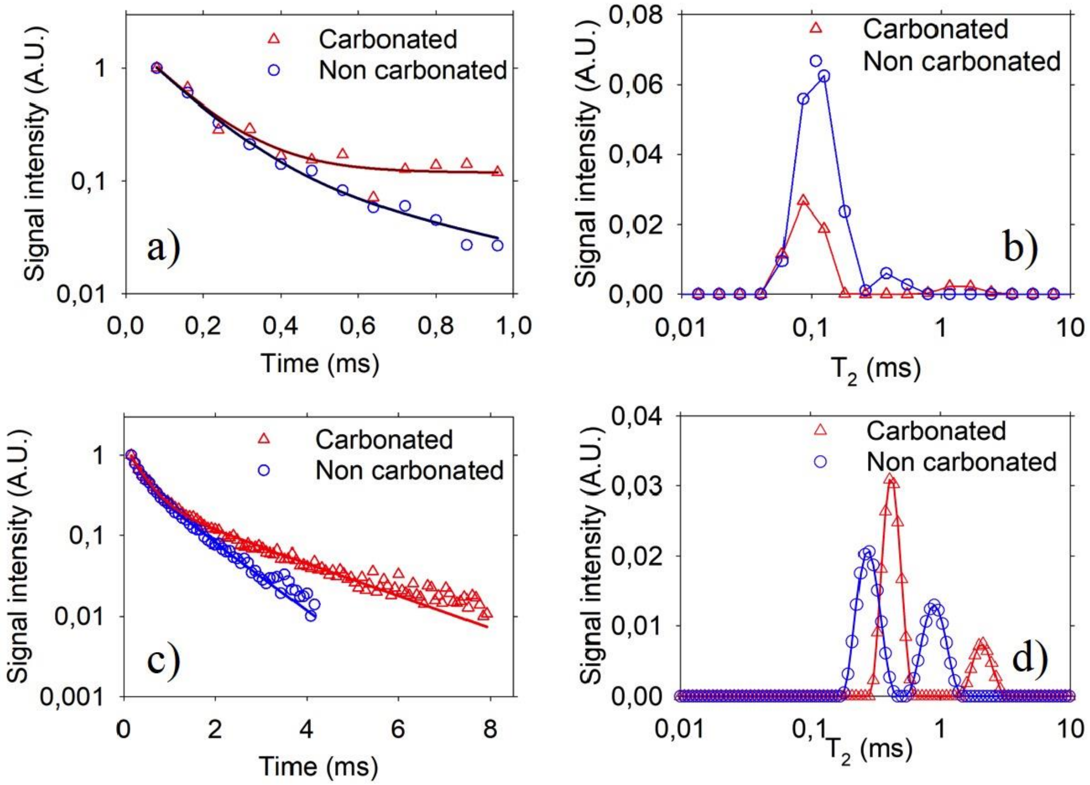

Figure 3.5 Semi log plots of the normalized signal intensity as a function of time (a and c) and the T_2 lifetime distribution obtained with the inverse Laplace Transform (b and d) of CPMG decays observed in carbonated and non-carbonated zones of 0.60 w/c ratio Portland cement mortar + 20 % FA. a and b) Unsaturated and in equilibrium at 65 % RH and 35 °C, and c and d) Water vacuum saturated sample. The solid lines are the best fit of the data to a biexponential decay function. The original CPMG decay data were used for the Inverse Laplace Transformation, not the normalized data shown in a and c.

Results of the long T_2 lifetime component and its corresponding signal intensity at different positions along partially carbonated and control mortar samples (vacuum saturated with water) are shown in Figure 3.6. Signal intensity was lower in the carbonated zone compared with the non-carbonated zone. This is due to the decrease in porosity caused by the precipitation of calcite (Ngalaand & Page, 1997) and it is consistent with the relative changes in porosity determined by the ASTM C642 (ASTM C 642-13, 2013) (Table 3.2). The highest rate of change of T_2 lifetime or in the signal intensity, or more clearly at the crossing point of these two parameters, is in a good agreement with the carbonation depth indicated by the phenolphthalein test. Taking both the T_2 and signal intensity curves in the analysis gives us the possibility of detecting zones with different properties related to carbonation. However, there are other phenomena that also produces microstructural changes, such as deficient curing of the samples and microcracking that would produce changes in T_2 lifetime and signal intensity. In the case of deficient curing, the outer layer would be more porous than the interior, and longer T_2 values in this outer layer would be observed. However, the signal intensity would be also higher in this layer because of more water in the pore space than in the interior layer. In the case of microcracking on the surface, the T_2 and the signal intensity in the outer layer would both be higher than in the interior layer. Based on the aforementioned, the patterns of T_2 lifetime and signal intensity produced by carbonation are unique features that distinguish carbonation from other phenomena occurring in cement-based materials.

Table 3.2 Porosity in carbonated and non-carbonated regions of the mortars

		ASTM C642-13		SEM	
	w/c	**Carbonated (%)**	**Non-carbonated (%)**	**Carbonated (%)**	**Non-carbonated (%)**
OPC + 20 % FA Mortar	0.60	19.0	24.8	8.5	11.8
OPC Mortar	0.60	20.4	24.4	3.5	10.9

The spatial resolution of the profiles was improved compared to previous research (Cano-Barrita et al., 2017) because the elliptical coil has a smaller distance of influence. The sample was displaced in steps of 0.25 cm in the carbonated region where microstructural changes occur, and 1 cm in the non-carbonated region where more uniform T_2 values were expected. However, eight times more scans were necessary to obtain a useful signal due to the reduction in the volume of cement paste caused by the inclusion of silica sand, in comparison with samples of pure cement paste. The main source of NMR signal in the mortar samples is pore water in the hydrated cement paste because the water absorbed by the sand is negligible

(0.26 %). Therefore, the SNR was 54 and 94 in the carbonated and non-carbonated regions, respectively. The carbonation depth in the mortar containing FA (Figure 3.6b) was similar to the depth in the OPC mortar (Figure 3.6a). This was not expected, because FA normally increases the carbonation depth in cement-based materials (Papadakis, 2000). The long moist curing time probably made the mortar impermeable enough to exhibit similar carbonation depth as the OPC mortar.

Results of NMR measurements along the unsaturated sample at two years of carbonation are given in Figure 3.7. The short T_2 lifetime component (Figure 3.7a), which is associated with interlayer water and water in gel pores, did not have an observable difference between the carbonated and non-carbonated zones. This may be explained by the fact that carbonation produces changes in the microstructure, precipitating calcium carbonate crystals in capillary pores, rather than in gel pores. However, the signal intensity was lower in the carbonated zone. This may be explained by the carbonation of the C-S-H, which produces silica gel with a coarse pore structure of about 300 nm (Pihlajavaara, 1968), thus reducing the number of gel pores in the carbonated zone and increasing the coarse porosity characteristic of the silica gel.

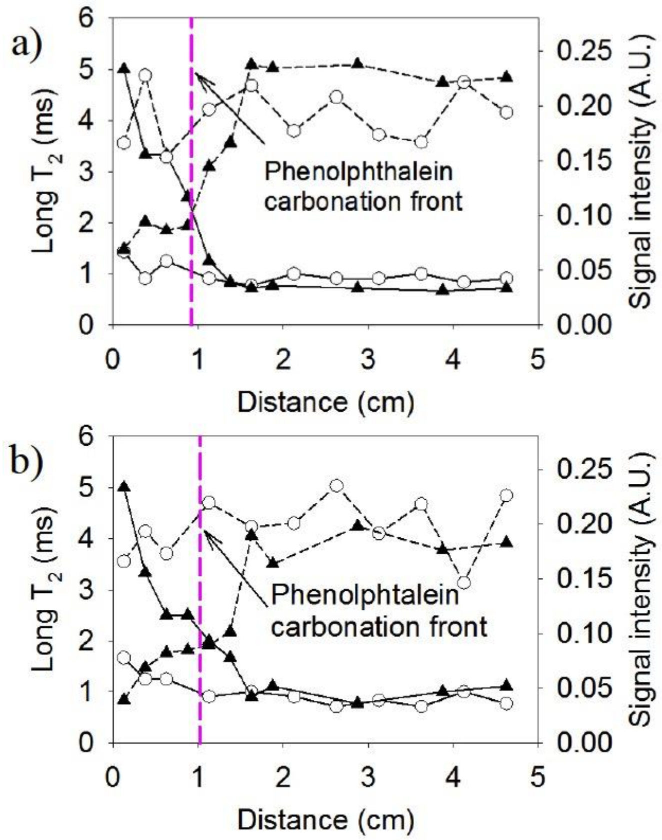

Figure 3.6 Long T_2 lifetime component (solid line) and signal intensity (dashed line) versus distance in vacuum saturated partially carbonated mortars (triangles) and control (circles), a) 0.60 w/c ratio OPC mortar, b) 0.60 w/c ratio OPC + 20% FA mortar. The echo time used in the CPMG acquisition was 130 μs. Photographs of the samples after spraying with phenolphthalein are shown in Figure A.3 in the Appendix.

The long T_2 lifetime component (Figure 3.7b) is longer in the carbonated zone than in the non-carbonated one. This may be the result of the well-known porosity and pore size distribution changes produced by carbonation (large pores in the silica gel) and also by changes in surface relaxivity of the pore space produced by the precipitation of calcium carbonate crystals, mainly calcite (Cano-Barrita et al., 2017). The surface relaxivity depends on the chemical composition of the surface interacting with the pore water molecules. It has been reported that the surface relaxation capacity of synthetic calcite and C-S-H is 2.74 and 5.51 μm/s, respectively (Dalas et al., 2014). In this context, the presence of calcite crystals should increase the T_2 lifetime of water in the pore solution in the carbonated zone (Cano-Barrita et al., 2017). The relationship between the surface relaxivity (ρ), surface to volume ratio

(S/V) of the pore space and the relaxation rate ($1/T_2$) is expressed by Eq. 3.3 (Coates, Xiao, & Prammer, 1999).

$$\frac{1}{T_2} = \rho \cdot \frac{S}{V} \tag{3.3}$$

The signal intensity was lower in the carbonated zone (see Figure 3.7b), which is consistent with a decrease of capillary porosity caused by carbonation. This same behavior was observed by Pihlajavaara (Pihlajavaara, 1968), who observed a reduction of pore volume caused by carbonation, in porosity ranging from 100-12.5 nm in diameter. This porosity is considered part of the capillary porosity.

Results from the vacuum saturated mortar are shown in Figure 3.8. There is an observable trend in the short T_2 lifetime component (Figure 3.8a), similar to the behavior exhibited by the long lifetime component (Figure 3.6). However, the signal intensity in this zone is slightly higher than in the non-carbonated zone, which corresponds to the coarse porosity of the silica gel produced as a result of C-S-H carbonation. Looking at the long T_2 lifetime component and its corresponding signal intensity (Figure 3.8b), it has the same behavior reported previously on Portland cement pastes (Cano-Barrita et al., 2017), which is an increase in the T_2 lifetime component and a decrease in the signal intensity.

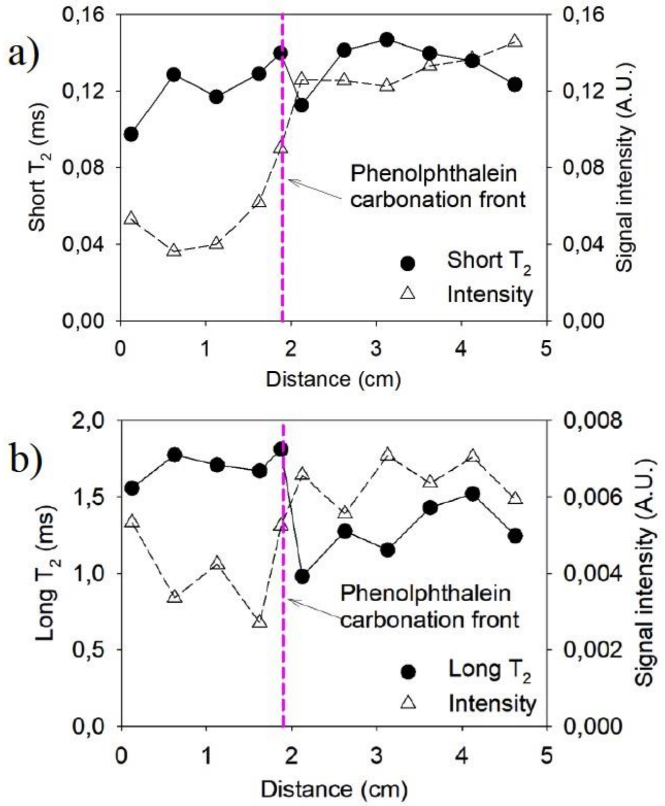

Figure 3.7 T_2 lifetime components (circles) and signal intensity (triangles) versus distance in 5 cm long unsaturated and partially carbonated 0.60 w/c ratio OPC + 20 % FA mortar, a) Short lifetime component and its corresponding signal intensity, and b) Long lifetime component and its corresponding signal intensity. The echo time used in these CPMG measurements was 80 μs, the shortest possible to capture the signal from the fast-relaxing spins in the sample assigned to water in the gel and small capillary pores.

The T_2 lifetime curve has a bent shape, which is similar to the shape of the $CaCO_3$ content as a function of depth observed by other researchers using techniques such as TGA (Chang & Chen, 2006) and gamma densitometry (Thiery, Villain, Dangla, & Platret, 2007). Thiery et al (Thiery et al., 2007) suggested that the observed shape results from the kinetics of the chemical reactions during the carbonation that become rate-controlling processes rather than the diffusion of CO_2 through the air in the pore system. Averaging the carbonation depth position in different parts of the mortar sample would produce a more reliable profile shape, especially when testing concrete that contains larger aggregates (coarse aggregate > 4.75 mm). In the same way, the resulting profile would be more reliable than just one profile per sample, due to the random location of aggregates that do not contribute to the NMR signal.

As shown by other researchers, the phenolphthalein test underestimates de carbonation depth by as much as 50 % (Chang & Chen, 2006) when compared with results obtained using other techniques such as TGA, XRD, and FTIR on powder samples collected at different depths of a carbonated specimen. Figure 3.10 shows a comparison between the carbonation depth obtained at the crossing point of the long T_2 lifetime component and the signal intensity curves and the carbonation depth determined with the phenolphthalein test. There is a good agreement between these carbonation depths that fall within the line of equality. In this case, the slope of the fitted line is 1.07 with an $r^2 = 0.95$. Another criterion was to take the carbonation depth as the position where the T_2 starts to behave nearly constant, indicating a deeper penetration of the carbonation. The slope of the fitted line is now 1.44 with an $r^2 = 0.90$. In both fittings, the line was forced to pass through the origin. The actual carbonation depth taken as the position where the T_2 starts to behave nearly constant provides values in between the line of equality (slope = 1) and the carbonation depth estimated according to Chang and Chen (Chang & Chen, 2006) (slope = 2). This result demonstrates the ability of the NMR measurements to detect, in a nondestructive and non-invasive manner, the progressive microstructural changes in the mortars caused by carbonation, which occur deeper than indicated by the phenolphthalein test.

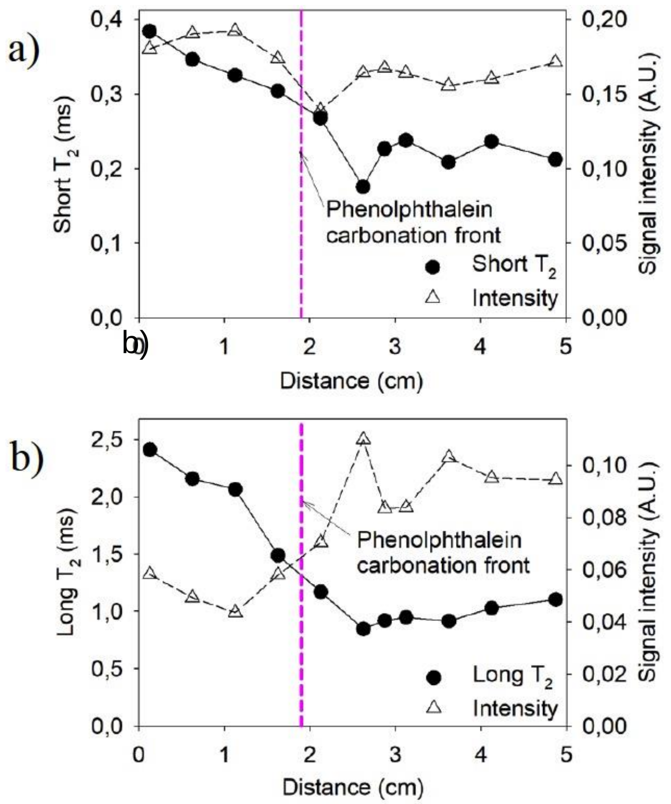

Figure 3.8 T_2 lifetime components (circles) and signal intensity (triangles) versus distance in 5 cm long vacuum-saturated and partially carbonated 0.60 w/c ratio OPC + 20 % FA mortar, a) Short lifetime component and its corresponding signal intensity b) Long lifetime component and its corresponding signal intensity. The echo time used in these CPMG measurements was 80 μs. A photograph of the sample after spraying with phenolphthalein is shown in Figure A.4 in the Appendix.

Another way of visualizing the NMR results is by the stack plot of the T_2 lifetime distributions along the length of the samples (Figure 3.9). In the 2D contour plots the major changes are shown in the long T_2 lifetime population at about 2 cm from the mortar surface, as shown in Figures 3.7 and 3.8. The population of interlayer water and gel pores remain relatively constant along the length of the sample (both are considered in the first pore population because the low SNR of the decay does not allow separation of those pore populations that are very close to each other).

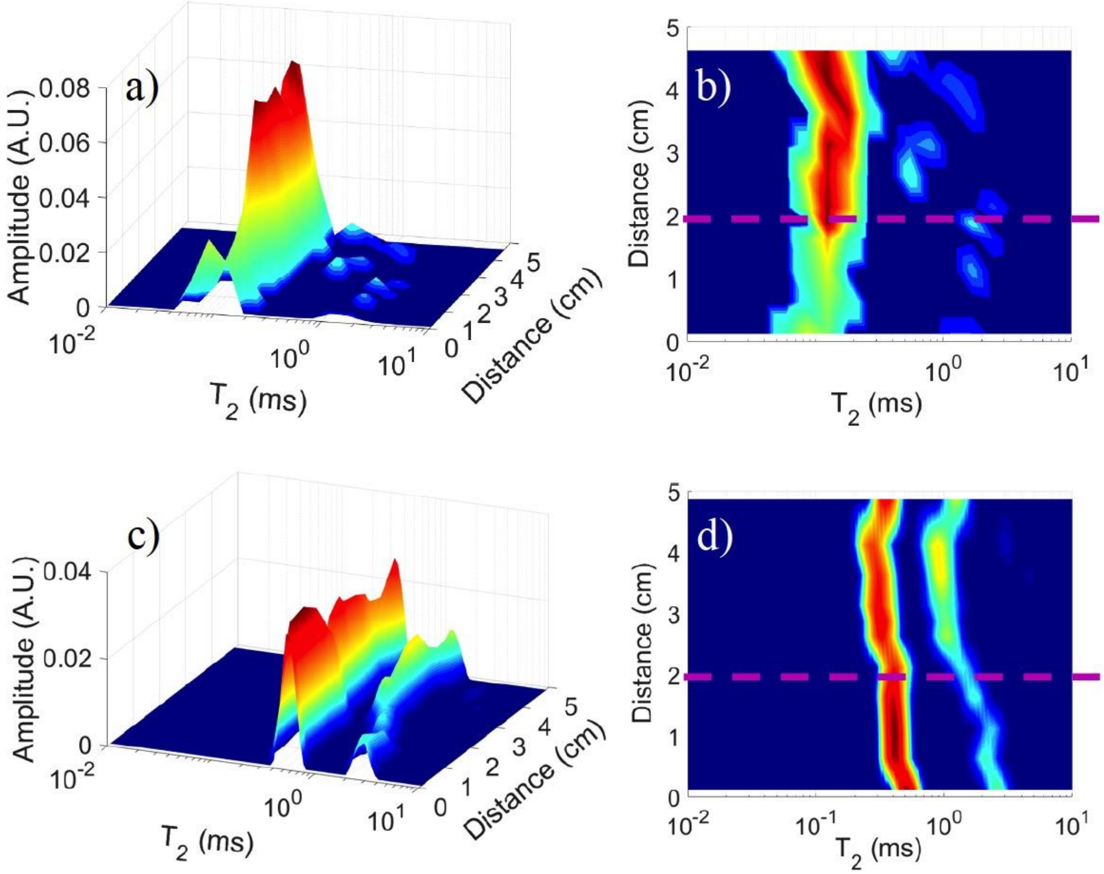

Figure 3.9 3D stack plot and 2D contour map of the T_2 lifetime distributions for the unsaturated a) and b), and vacuum saturated c) and d) mortar sample containing 20 % FA. The surface of the mortar is at 0 cm. The pink line is the carbonation depth determined by the phenolphthalein test.

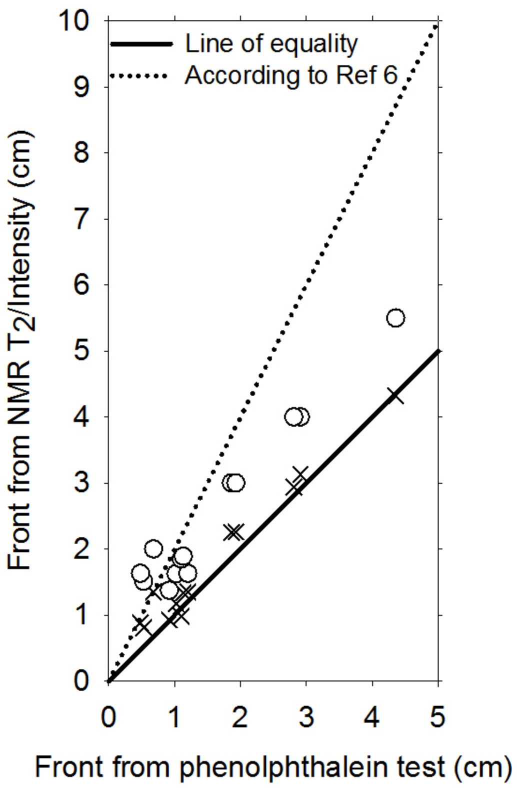

Figure 3.10 Comparison of the carbonation depths in cement pastes (tested but not reported in this paper) and mortars obtained with the phenolphthalein test and from the Long T_2 component. The crosses indicate the carbonation depth obtained by the crossing of the T_2 and signal intensity profiles, whereas the circles represent the carbonation depth at which T_2 starts to behave nearly constant in the non-carbonated zone.

3.3.3 Analysis of the capillary macro-porosity from SEM images

Conditioning the mortar samples at 65 % RH and 35 °C caused drying shrinkage micro-cracking. Figure 3.11 shows SEM images at 1000× of the carbonated, transition and non-carbonated zones of a polished section of the OPC mortar sample, where micro-cracking is observed. The quantity of cracks and the crack width is significantly reduced in the carbonated zone as a result of precipitation of calcium carbonate, compared with the non-carbonated zone. Microcrack indicated with the letter f in Figure 3.11 (center image) shows it is being filled with calcium carbonate. Microcracks in the carbonated region are filled, whereas microcracks in the non-carbonated region remain open. The width of the micro-cracks estimated from the SEM images is in the range of 0.3 to 1.3 μm and 0.4 to 2.8 μm in the carbonated and non-carbonated zones, respectively.

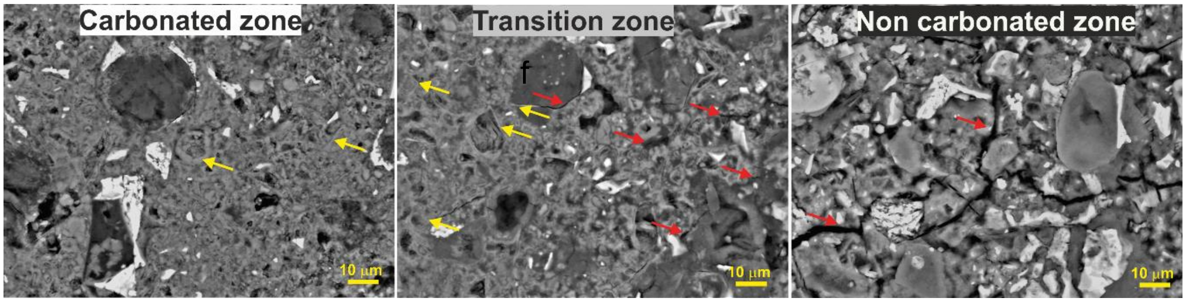

Figure 3.11 SEM images of a polished section of an OPC mortar sample subjected to accelerated carbonation. Arrows indicate non-sealed microcracking (red) and sealed microcracking (yellow) by calcium carbonate.

Figure 3.12 shows the results of the SEM image analysis. Figure 3.12a presents the capillary macropore size analysis (Figure 3.12a) and micro-crack length distribution (Figure 3.12b). There is a reduction in the percentage of the total void area (pores + micro-cracks) compared with the total image area in the carbonated zone (3.5 %) compared with the non-carbonated zone (10.9 %). In the noncarbonated zone, 68.8 % of the total voids correspond to micro-cracks, and 31.2 % correspond to the capillary macropores. On the other hand, in the carbonated zone, 47.8 % correspond to micro-cracks, and 52.2 % correspond to capillary macropores. The local porosity by SEM images analysis is smaller than the permeable porosity determined with the ASTM C642 (ASTM C 642-13, 2013) standard since SEM images even at 1200× magnification only captured the capillary macropores from approximately 1 to 10 μm (Diamond & Leeman, 1995), similar to our results. It is important to consider that the local porosity obtained by SEM image analysis corresponds to a two-dimensional porosity value, therefore it does not consider the pore volume (Diamond & Leeman, 1995). However, the difference in the percentage of porosity obtained by ASTM C642 between carbonated and non-carbonated mortars with 0.60 w/c ratio is on the same order of magnitude as the difference observed from the SEM image analysis (Figure 3.12c).

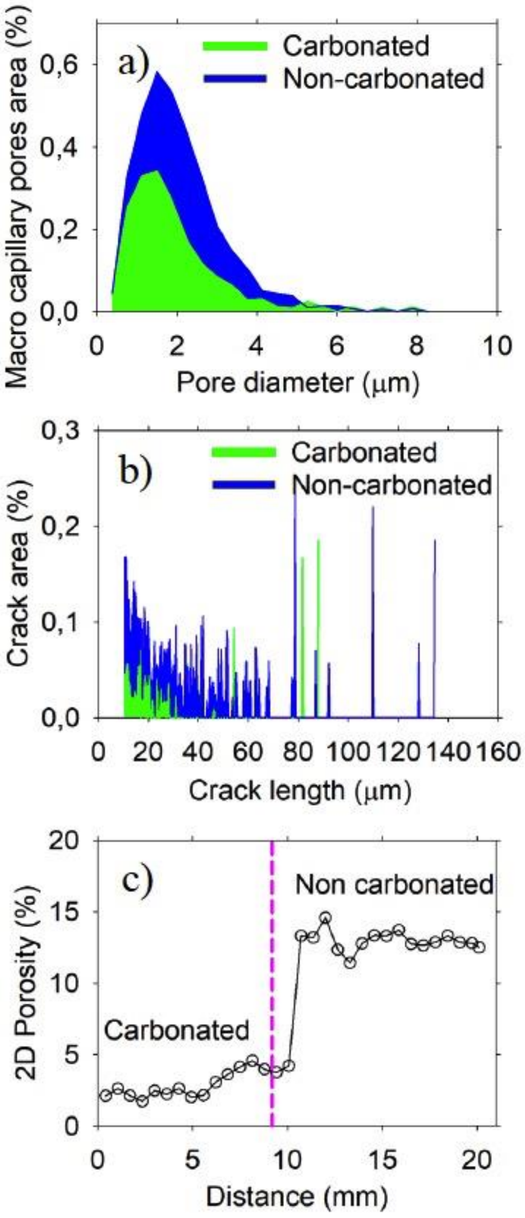

Figure 3.12 SEM image analysis of the carbonated and non-carbonated region of an OPC mortar sample, a) Macro capillary pore size distribution, b) Crack length distribution, and c) 2D macro-porosity obtained from SEM images in the carbonated and non-carbonated regions along the length of the sample shown in Figure 2.6a.

Figure 3.12c indicates a good agreement between the crossing point of the T_2 lifetime and signal intensity curves with both the phenolphthalein depth and the point where the porosity from the SEM images changes from low to high values.

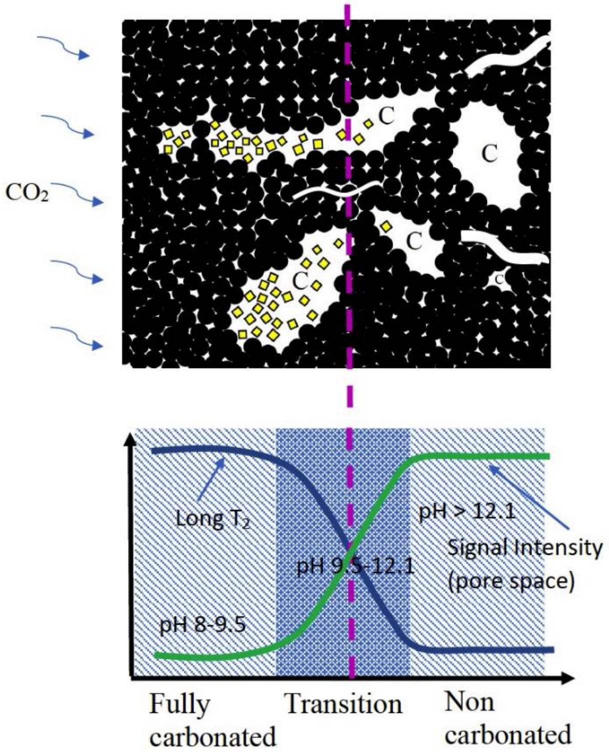

Figure 3.13 Simplified microstructure model of hydrated cement paste based on ref (Powers, 1958) and its relation with the NMR parameters (Long T_2 lifetime and signal intensity) in a carbonated cement paste. Solid circles represent the C-S-H, interstitial spaces are gel pores, spaces marked with C are capillary pores. The pink dashed line indicates the carbonation depth detected with the phenolphthalein test: Yellow squares represent the calcite formed during the carbonation process, and the white curves represent micro-cracks. All the features shown are not on scale.

Based on the NMR results and the SEM images that show the macropores and micro-cracking, it is suggested that microcracking influences the long T_2 values, as the cracks have a width in the range of 0.3 to 2.8 μm that are much larger than the capillary pores in the hydrated cement paste. The NMR T_2 lifetimes values are directly proportional to the crack width (Cano-Barrita et al., 2015). Figure 3.13 shows a graphical representation of the hydrated cement paste in the carbonated, transition and non-carbonated zones, relating the gel and capillary pores, as well as the cracks, with the T_2 lifetimes and signal intensities observed in the NMR measurements. Notice that the longer T_2 in the carbonated region does not necessarily imply larger pores or wider cracks, according to Eq. 2.3, because the surface relaxivity decreases in comparison with the non-carbonated region. It is important to mention that the T_2 lifetime and signal intensity curves exhibit similar behavior as those curves of degree of carbonation and the pH of a carbonated sample reported in the literature (Chang & Chen, 2006; Liu, Niu, Li, Lv, & Fu, 2018), respectively.

3.4 Conclusions

A three-magnet array combined with an elliptical RF coil was used to improve the NMR measurements to detect the carbonation depth in carbonated saturated/unsaturated Portland cement mortars. Based on the results, the following conclusions are drawn:

The spatial resolution (0.25 cm) was improved four times using the proposed elliptical surface RF coil, compared to previous research (Cano-Barrita et al., 2017). The improvement was mainly because the coil shape allowed excitation of a thin region of the sample.

CPMG measurements were successfully undertaken in unsaturated and vacuum-saturated mortar, revealing differences in the CPMG decays in carbonated and non-carbonated zones, caused by changes in surface relaxivities, porosity, and pore size distribution. Detecting carbonation depth in unsaturated samples would permit time-based studies in mortars and possibly concrete materials.

The crossover point between the curves of long T_2 lifetime component and its corresponding signal intensity as a function of distance, was in good agreement with the carbonation depth indicated by the phenolphthalein test, whereas if the position where the T_2 lifetime starts to behave nearly constant is considered, the carbonation depth is 1.44 times higher than the depth obtained by the phenolphthalein test, indicating a more realistic carbonation depth.

SEM images analysis revealed that there was a significant change of local porosity in the carbonated region in comparison with the non-carbonated region, reducing the frequency and size of cracks and pores.

Future applications of the three-magnet array with the elliptical coil would permit obtaining moisture content profiles of long mortar or concrete samples under drying or water absorption conditions.

Acknowledgments

P. Cano acknowledges Dr. Bruce J. Balcom, Director of the MRI Centre of the University of New Brunswick, for donating the three-magnet array to our lab. P. Cano also acknowledges the Consejo Nacional de Ciencia y Tecnología (CONACYT) of Mexico and SIP from Instituto Politécnico Nacional for funding the projects with ID code 239727 and 20170803, respectively. F. Diaz acknowledges CONACYT for a graduate studies scholarship and to the COFAA-IPN for a BEIFI scholarship for his doctoral studies.

3.5 References

ASTM C 642-13. (2013). Standard test method for density, absorption, and voids in hardened concrete. *ASTM International, West Conshohocken, PA*, 1–3.

ASTM C109M-16a. (2016). Standard Test Method for Compressive Strength of Hydraulic Cement Mortars. *ASTM International, West Conshohocken, PA*. https://doi.org/10.1520/C0305-06.2

ASTM C305. (2014). Standard Practice for Mechanical Mixing of Hydraulic Cement Pastes and Mortars of Plastic Consistency. *ASTM International, West Conshohocken, PA*. https://doi.org/10.1520/C0305-13.2

Bier, T. A., Kropp, J., & Hilsdorf, H. K. (1989). The formation of silica gel during carbonation of cementitious systems containing slag cements. In *Proceedings of the 3rd International Conference on the Use of Fly Ash, Silica Fume, Slag, and Natural Pozzolans in Concrete* (Vol. SP 114-69, pp. 1413–1428). Trondheim.

Bu, Y., Spragg, R., & Weiss, W. J. (2014). Comparison of the pore volume in concrete as determined using ASTM C642 and vacuum saturation. *Advances in Civil Engineering Materials*, *3*(1), 308–315.

Cano-Barrita, P. F. de J., Balcom, B. J., Bremner, T. W., MacMillan, M. B., & Langley, W. S. (2004). Moisture distribution in drying ordinary and high performance concrete cured in a simulated hot dry climate. *Materials and Structures/Materiaux et Constructions*, *37*(272), 522–531. https://doi.org/10.1617/13968

Cano-Barrita, P. F. de J., Balcom, B. J., & Castellanos, F. (2017). Carbonation front in cement paste detected by T 2 NMR measurements using a low field unilateral magnet. *Materials and Structures*, *50*, 1–8. https://doi.org/10.1617/s11527-017-1019-5

Cano-Barrita, P. F. de J., Castellanos, F., Ramírez-Arellanes, S., Cosmes-López, M. F., Reyes-Estevez, L. R., Hernández-Arrazola, S. E., & Ramírez-Ortíz, A. E. (2015). Monitoring Compressive Strength of Concrete by Nuclear Magnetic Resonance, Ultrasound, and Rebound Hammer. *Materials Journal*, *112*(1), 147–154.

Cano, F. de J., Bremner, T. W., Mcgregor, R. P., & Balcom, B. J. (2002). Magnetic resonance imaging of 1H , 23Na , and 35Cl penetration in Portland cement mortar. *Cement and Concrete Research*, *32*, 1067–1070.

Chang, C. F., & Chen, J. W. (2006). The experimental investigation of concrete carbonation depth. *Cement and Concrete Research*, *36*(9), 1760–1767. https://doi.org/10.1016/j.cemconres.2004.07.025

Coates, G. R., Xiao, L., & Prammer, M. G. (1999). *NMR Logging principles & applications*. (R. F. Sigal & S. J. Bollich, Eds.). Houston, Texas, USA: Halliburton Energy Services.

Dalas, F., Korb, J., Pourchet, S., Nonat, A., Rinaldi, D., & Mosquet, M. (2014). Surface Relaxivity of Cement Hydrates. https://doi.org/10.1021/jp500055p

Diamond, S., & Leeman, M. E. (1995). Pore size distribution in hardened cement paste by SEM image analysis. In *MRS Proceedings* (Vol. 370, pp. 217–226). Cambridge University Press. https://doi.org/doi:10.1557/PROC-370-217

Díaz-Díaz, F., Cano-Barrita, P. F. de J., Balcom, B. J., Solís-Nájera, S. E., & Rodríguez, A. O. (2013). Embedded NMR sensor to monitor compressive strength development and pore size distribution in hydrating concrete. *Sensors (Switzerland)*, *13*(12), 15985–15999. https://doi.org/10.3390/s131215985

Elia, P., Nativ-Roth, E., Zeiri, Y., & Porat, Z. (2016). Determination of the average pore-size and total porosity in porous silicon layers by image processing of SEM micrographs. *Microporous and*

Mesoporous Materials, *225*, 465–471. https://doi.org/10.1016/j.micromeso.2016.01.007

Enjilela, R., Cano-Barrita, P. F. de J., Komar, A., Boyd, A. J., & Balcom, B. J. (2018). Wet front penetration with unsteady state wicking in mortar studied by Magnetic Resonance Imaging (MRI). *Materials and Structures/Materiaux et Constructions*, *51*, 1–16. https://doi.org/10.1617/s11527-018-1142-y

Garcia-Naranjo, J. C. (2012). *Three-Magnet Arrays for Unilateral Magnetic Resonance*. PhD Thesis, University of New Brunswick, Canada.

Jehng, J. Y., Sprague, D. T., & Halperin, W. P. (1996). Pore structure of hydrating cement paste by magnetic resonance relaxation analysis and freezing. *Magnetic Resonance Imaging*, *14*(7–8), 785–791. https://doi.org/10.1016/S0730-725X(96)00164-6

Johannesson, B., & Utgenannt, P. (2001). Microstructural changes caused by carbonation of cement mortar. *Cement and Concrete Research*, *31*, 925–931. https://doi.org/10.1016/S0008-8846(01)00498-7

Liu, X., Niu, D., Li, X., Lv, Y., & Fu, Q. (2018). Pore solution pH for the corrosion initiation of rebars embedded in concrete under a long-term natural carbonation reaction. *Applied Sciences (Switzerland)*, *8*(128), 1–15. https://doi.org/10.3390/app8010128

Mehta, P. K., & Monteiro, P. J. M. (2006). *Concrete: Microstructure, properties and materials* (3rd ed.). New York: McGraw-Hil. https://doi.org/10.1036/0071462899

Meiboom, S., & Gill, D. (1958). Modified Spin-Echo Method for Measuring Nuclear Relaxation Times. *Review of Scientific Instruments*, *29*(8), 688–91.

Miljkovic, L., Lasic, D., MacTavish, J. C., Pintar, M. M., Blinc, R., & Lahajnar, G. (1988). NMR studies of hydrating cement: a spin-spin relalxation study of the early hydration stage. *Cement and Concrete Research*, *18*(6), 951–956.

Ngalaand, V. T., & Page, C. L. (1997). Effect of carbonation pore structure and diffusional properties of hydrated cement pastes. *Cement and Concrete Research*, *27*(7), 995–1007.

Pacheco Torgal, F., Miraldo, S., Labrincha, J. A., & De Brito, J. (2012). An overview on concrete carbonation in the context of eco-efficient construction: Evaluation, use of SCMs and/or RAC. *Construction and Building Materials*, *36*, 141–150.

Papadakis, V. G. (2000). Effect of supplementary cementing materials on concrete resistance against carbonation and chloride ingress. *Cement and Concrete Research*, *30*(2), 291–299. https://doi.org/10.1016/S0008-8846(99)00249-5

Pihlajavaara, S. E. (1968). Some results of the effect of carbonation on the porosity and pore size distribution of cement paste. *Materiaux et Constructions*, *1*(6), 521–527. https://doi.org/10.1007/BF02473640

Powers, T. C. (1958). Structure and Physical Properties of Hardened Portland Cement Paste. *Journal of the American Ceramic Society*, *41*(1), 1–6.

RILEM Recommendations CPC-18. (1988). CPC-18 Measurement of hardened concrete carbonation depth. *Materials and Structures*, *21*(6), 453–455.

Rimmelé, G., Barlet-Gouédard, V., Porcherie, O., Goffé, B., & Brunet, F. (2008). Heterogeneous porosity distribution in Portland cement exposed to CO2-rich fluids. *Cement and Concrete Research*, *38*(8–9), 1038–1048. https://doi.org/10.1016/j.cemconres.2008.03.022

Safiuddin, M., & Hearn, N. (2005). Comparison of ASTM saturation techniques for measuring the permeable porosity of concrete. *Cement and Concrete Research*, *35*(5), 1008–1013.

Thiery, M., Villain, G., Dangla, P., & Platret, G. (2007). Investigation of the carbonation front shape on cementitious materials: Effects of the chemical kinetics. *Cement and Concrete Research*, *37*(7), 1047–1058.

Tovey, N. K., & Hounslow, M. W. (1995). Quantitative Microporosity and Orientation Analysis in Soils and Sediments. *Journal of the Geological Society of London*, *152*, 119–129.

van der Heijden, G. H. A., van Bijnen, R. M. W., Pel, L., & Huinink, H. P. (2007). Moisture transport in heated concrete, as studied by NMR, and its consequences for fire spalling. *Cement and Concrete Research*, *37*(6), 894–901. https://doi.org/10.1016/j.cemconres.2007.03.004

Winnefeld, F., Scholer, A., & Lothenbach, B. (2016). Chapter 1: Sample preparation. In K. Scrivener, R. Snellings, & B. Lothenbach (Eds.), *A Practical Guide to Microstructural Analysis of Cementitious Materials* (p. 540). CRC Press, Taylor & Francis Group.

Zhou, Y., Gencturk, B., Willam, K., & Attar, A. (2015). Carbonation-Induced and Chloride-Induced Corrosion in Reinforced Concrete Structures. *Journal of Materials in Civil Engineering*, *27*(9), 04014245. https://doi.org/10.1061/(ASCE)MT.1943-5533.0001209

Ziel, R., Haus, A., & Tulke, A. (2008). Quantification of the pore size distribution (porosity profiles) in microfiltration membranes by SEM, TEM and computer image analysis. *Journal of Membrane Science*, *323*(2), 241–246. https://doi.org/10.1016/j.memsci.2008.05.057

Appendix

Table A.1. Oxide content of the Portland cement and the class F fly ash

Oxide	OPC (weight %)	FA (weight %)
SiO_2	21.07	62.28
Al_2O_3	3.69	20.38
Fe_2O_3	4.50	4.09
CaO	61.93	4.68
TiO_2	0.97	0.94
P_2O_5	0.10	0.38
MgO	1.83	0.98
Na_2O	0.09	0.31
K_2O	0.30	0.99
SO_3	2.54	-
LOI	4.38	3.43

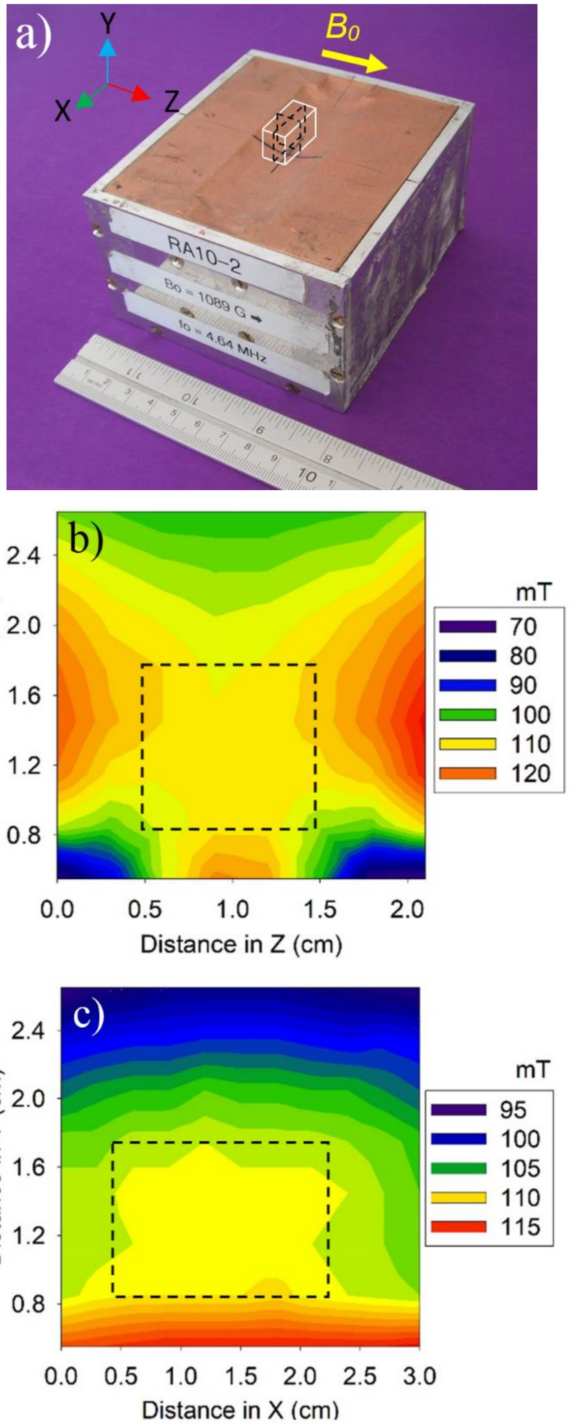

Figure A.1 (a) The three-magnet array generates a volume of relatively homogeneous magnetic field of 109 mT at a distance of 0.9 cm from the surface of the magnet, (b) magnetic field in the plane YZ, and (c) Magnetic field in the plane YX. The dotted square and rectangle show the more homogeneous magnetic field in each plane. The magnetic field was measured in the planes XY and YZ by manually displacing an HT-20 handheld single axis gaussmeter (Hangzhou Best Magnet Co. Ltd, Zhejiang, China) with a resolution of 0.1 mT, in a 3 mm grid size on graph paper.

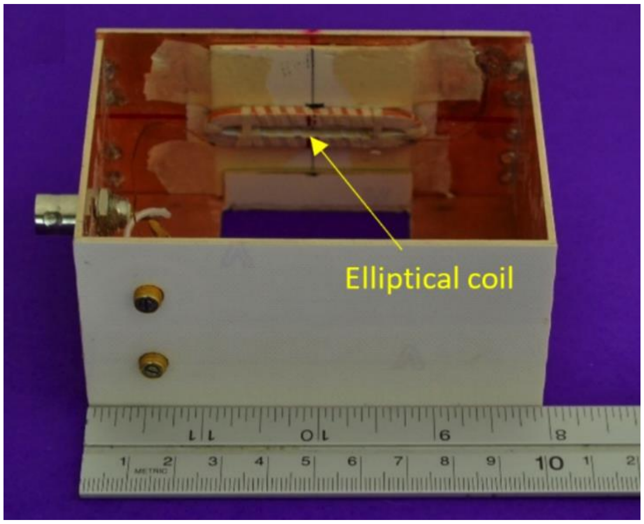

Figure A.2 Elliptical surface RF coil placed inside a Faraday cage to reduce external noise.

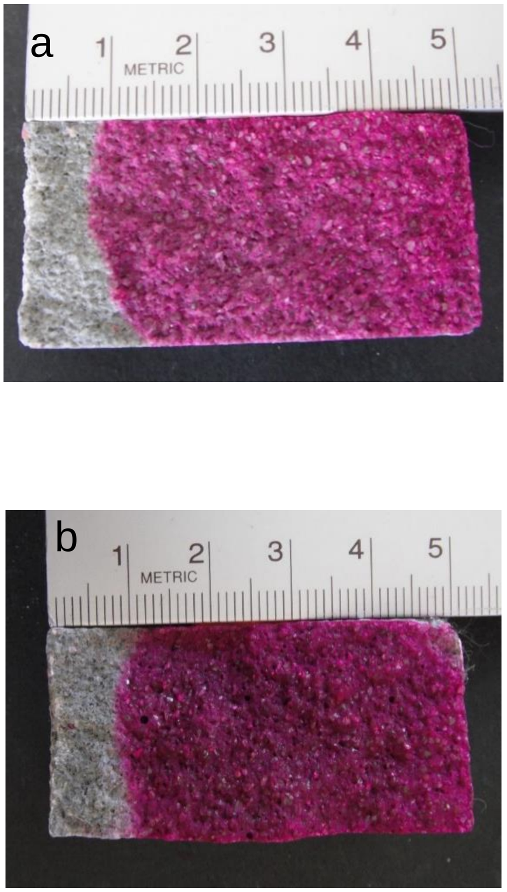

Figure A.3. Photographs of the mortar samples at six months of carbonation after spraying with phenolphthalein, corresponding to Figure 3.6, a) OPC mortar, and b) OPC + 20 % FA mortar.

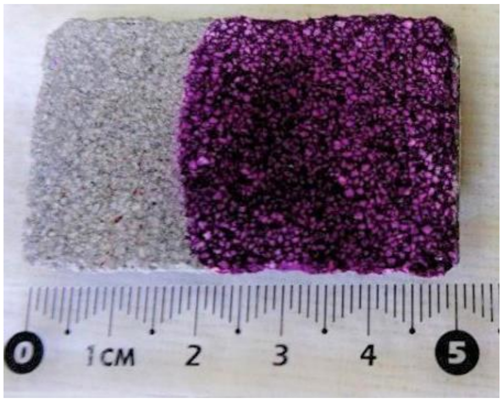

Figure A.4. Photograph of the OPC + 20 % FA mortar sample at two years of carbonation after spraying with phenolphthalein, corresponding to the sample used in Figures 3.7 and 3.8.

Capítulo 4. Moisture distribution profiles during water absorption of mortars obtained nondestructively by low-field unilateral magnetic resonance

Abstract

Moisture distribution in cement-based materials is important from the durability point of view. In the present study, a portable three-magnet array with an elliptical surface RF coil was used to undertake magnetic resonance measurements of moisture content in mortar and concrete samples. Measurements along the length of the samples during capillary water absorption produced moisture content profiles that were compared with reference profiles acquired using a magnetic resonance imaging instrument. Profiles obtained with the three-magnet array were similar in shape and in penetration depth to those acquired with magnetic resonance imaging. The correlation coefficient between the moisture content measured with both techniques was $r^2 = 0.97$. Similar values of saturated hydraulic conductivity of the mortars with identical w/c ratio were computed with the Hydrus 1D software based on the moisture content profiles. Additionally, Inverse Laplace Transformation of the signal decays provided the water-filled pore size distribution in saturated and unsaturated regions of the samples. The three-magnet array did not have sample size restriction, compared with traditional magnetic resonance imaging instruments.

Keywords: *Three-magnet array; elliptical RF coil; water absorption; pore water; moisture content; T_2 lifetime; hydraulic conductivity*

4.1 Introduction

Water plays a crucial role in reinforced concrete deterioration processes that reduce the service life of concrete structures. Knowing the moisture distribution during curing, as well as during drying or during water absorption processes is important for the evaluation of durability properties or modeling deterioration processes of cement-based materials. This is especially true for the cover concrete that resists the penetration of aggressive agents like chloride ions or carbon dioxide (Hilsdorf & Kropp, 2004) that diffuse through the pore water and may lead to reinforcing steel corrosion. During capillary water absorption, a simple visual inspection of the wet front movement in cement paste, mortar or concrete samples by observation of the color change is not a reliable measure of the true depth of water penetration (Fischer, Haerdtl, & McDonald, 2015a). The gravimetric method is traditionally used to determine the moisture content of cement-based materials by oven-drying samples at 105 ^{o}C until constant mass. If the moisture distribution is required, the sample is cut in slices at least 10 mm thick. With different slices along the length of the sample, the spatial moisture distribution is obtained, although with a low resolution (Šelih & Bremner, 2006). Neutron radiography is a nondestructive technique that has been occasionally used to obtain moisture distribution profiles in drying mortar (Villmann, Slowik, Wittmann, Vontobel, & Hovind, 2014). However, some corrections on the measured neutron intensity are necessary, which may be a source of uncertainties on the measured profiles. Another nondestructive technique is magnetic resonance imaging (MRI), which can be used to obtain images in 1, 2 and 3 dimensions with millimetric resolution (Balcom et al., 2003). The sample size in low-field MRI systems varies from about 13 mm up to 150 mm in diameter. Larger samples can be analyzed in expensive systems with superconducting magnets with larger bore sizes. Another alternative is the use of low-field unilateral nuclear magnetic resonance (NMR) devices (Garcia-Naranjo, 2012) that have no restriction on sample size. They have been successfully used to characterize porosity and T_2 distribution of core plugs (García-naranjo, Guo, Marica, Liao, & Balcom, 2014), water content in wood (Lamason, Macmillan, Balcom, Leblon, & Pirouz, 2015) and carbonation of cement-based materials (Cano-Barrita, Balcom, & Castellanos, 2017; Díaz-Díaz, Cano-Barrita, León-Martínez, & Castellanos, 2020).

In this paper we present results from the use of a three-magnet array (García-naranjo et al., 2014) combined with an elliptical surface RF coil (Díaz-Díaz et al., 2020) to undertake NMR measurements of moisture content profiles in mortar and concrete samples. These profiles are compared with the reference true water content profiles obtained using the SPI T_2^* mapping MRI technique (Beyea et al., 1998). The saturated hydraulic conductivity (K_s) was extracted from the profiles by inverse modeling with the Hydrus 1D software (Radcliffe & Simunek, 2010). The three-magnet array was in addition used to obtain a moisture content profile in an ordinary concrete sample, which contained cement and aggregates normally used by the construction industry.

4.2 Materials and method

4.2.1 Materials

Ordinary Portland cement was employed to prepare the mortar mixtures. The chemical composition of the Portland cement was SiO_2 = 21.07 %, Al_2O_3 = 3.69 %, Fe_2O_3 = 4.50 %, CaO = 61.93 %, MgO = 1.83 %, Na_2O = 0.09 %, K_2O = 0.30 %, SO_3 = 2.54 %, and LOI = 4.38 %. Silica sand with water absorption of 0.22 %, density of 2.7, and fineness modulus of 2.86 was used as fine aggregate. Distilled water was used as mixing water, and for the capillary water absorption experiments.

4.2.2 Sample preparation and conditioning

Mortar mixtures at w/c ratios of 0.60 and 0.35, with cement to sand ratio by mass of 1:1.5, were prepared using a planetary motion mixer. These w/c ratio values represented high and low values that are of interest in the construction industry. Mortar samples at 0.60 w/c ratio, measuring 50 mm in diameter and 53 mm in length were cast in triplicate using PVC molds. Other 0.60 and 0.35 w/c ratio mortar samples, measuring 50 mm in diameter and 100 mm in length were cast in triplicate using PVC molds. All the samples were moist cured at room temperature in saturated lime water for 28 days. At the end of the moist curing period, the specimens measuring 100 mm in length were oven-dried at 50 °C until constant mass to minimize microcracking. The 0.60 w/c ratio samples measuring 50 mm in length were stored under laboratory ambient conditions for about one year to achieve a uniform moisture content. This conditioning simulated drying of the mortar under real conditions before undertaking the water absorption experiments. The saturated porosities measured gravimetrically were 0.179 and 0.269 for the 0.35 and 0.60 w/c ratio mortar samples, respectively. The curved surface of the samples was coated with epoxy resin to allow for unidirectional water absorption. The NMR signal from the epoxy resin was negligible compared with the signal of absorbed water (less than 1 % of the total signal).

A prismatic concrete sample was cut from an old 0.60 w/c ratio concrete cylinder. The cross-section area of the sample was 40 mm x 40 mm and 150 mm in length. This concrete contained ordinary Portland cement, natural river sand and crushed limestone aggregates normally used in the local construction industry. The saturated porosity of the sample was 0.148. The same conditioning procedure described for the mortar samples was followed for the concrete sample.

4.2.3 Water absorption experiments and NMR/MRI measurements

4.2.3.1 Water absorption experiments

The mortar samples were placed in contact with distilled water at 24 ^{o}C according to the method proposed by Hall (Hall, 1989) and also described in the ASTM C1585 standard (ASTM C1585-13, 2013). Mass measurements were undertaken at various absorption times. When the samples were used for NMR/MRI testing, a piece of duct tape was placed on the absorbing face to avoid drying during the measurements.

4.2.3.2 NMR measurements with the three-magnet array

A three-magnet array (García-naranjo et al., 2014) with an elliptical surface RF coil measuring 3 mm and 44 mm in minor and major internal diameters, respectively, was used with a Kea^2 spectrometer (Magritek Limited, Wellington, New Zealand) to undertake the NMR measurements. The three-magnet array generated a nearly homogeneous spot centered at 4.64 MHz (109 mT) See supplementary material in (Díaz-Díaz et al., 2020). The minor axis of the coil was oriented parallel to the sample displacement direction (Figure 4.1). This permitted reducing the width of the excited region of the sample (Díaz-Díaz et al., 2020), thus a profile of signal intensity versus distance could be obtained with an adequate resolution. The sample was displaced in steps of five mm with respect to the center of the elliptical RF coil. The CPMG technique (Meiboom & Gill, 1958) was employed to obtain the transverse magnetization decay at each position along the longitudinal axis of the sample. The parameters employed for these measurements were as follows: pulse width = 12 μs, number of echoes = 32, echo time = 80 μs, repetition time = 150 ms, number of scans = 16384, acquisition time = 63 minutes. To improve the signal to noise ratio of the NMR signal, a Faraday cage was built with aluminum foil to cover the three-magnet array system.

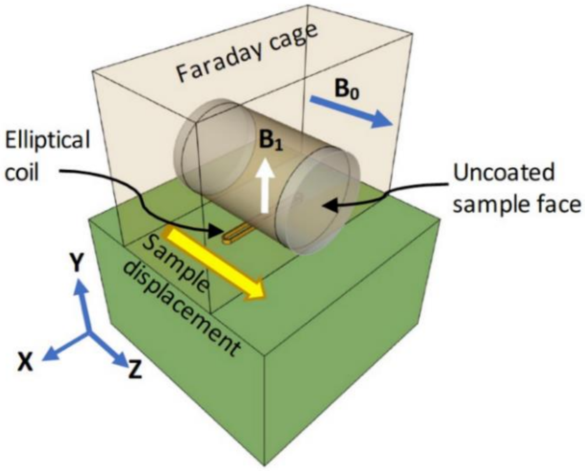

Figure 4.1. Three-magnet array (García-naranjo et al., 2014) with the elliptical surface RF coil to excite a thin region of the sample perpendicular to the sample displacement (Díaz-Díaz et al., 2020). Reproduced from (Díaz-Díaz et al., 2020)

The CPMG decays were fitted to a biexponential decay function (Eq 4.1) to obtain the T_2 lifetime constants and their corresponding signal intensities. The Inverse Laplace Transformation was additionally used to determine the T_2 lifetime distribution (Coates, Xiao, & Prammer, 1999), which is a proxy of the pore size distribution of the water-filled porosity in the sample.

$$S(t) = M_{0,1}e^{\left(-\frac{t}{T_{2,1}}\right)} + M_{0,2}e^{\left(-\frac{t}{T_{2,2}}\right)} \tag{4.1}$$

where S is the signal intensity, t is time, $M_{0,1}$ and $M_{0,2}$ are the equilibrium sample magnetization components corresponding to the $T_{2,1}$ and $T_{2,2}$ lifetime constants.

4.2.3.3 Low-field MRI measurements

To compare the moisture content profiles obtained with the three-magnet array, the Single Point Imaging (SPI) technique (Emid & Creyghton, 1985) was employed to undertake T_2^* mapping measurements (Beyea et al., 1998). These measurements were required to obtain true water content profiles that were used as a reference. The instrument used was a Maran DRX HF 12/50 MRI spectrometer (Oxford Instruments Ltd, Abingdon, Oxford, UK) operating at 12.9 MHz. The instrument was equipped with Techron gradient amplifiers 7782 (AE Techron, Elkhart, IN, USA). Parameters employed were pulse duration = 4 μs, fifteen encoding times (t_p) ranging from 50 to 290 ms, field of view (FOV) = 7 cm, number of scans = 512, number of points = 64, and a repetition time of 1.1 seconds. The total measurement time was 2.4 hours. Because of the variable t_p, the gradient step was adjusted to maintain a constant image FOV. The maximum sample length that could be tested with the MRI instrument was less than 50 mm. When the wet front was deeper than 50 mm, the SPI T_2^* mapping was undertaken in two movements of the sample. In this manner, the acquired profiles overlapped 30 mm and allowed obtaining the final profile (R. Enjilela, Cano-Barrita, Komar, Boyd, & Balcom, 2017). The set of acquired data at each t_p was Fourier transformed to obtain T_2^* weighted 1D images. The image intensity at each point in the profiles was plotted versus the encoding time. The observed decays were fitted to a single exponential decay function and back extrapolated to obtain the T_2^* lifetime and its signal amplitude at each spatial point in the profile (Beyea et al., 1998).

The NMR/MRI measurements on the 10 cm long mortar samples were undertaken at four days of water absorption. This time was long enough to have the movement of the wet front without significant change, about two or three millimeters per day. This condition was necessary to ensure a realistic moisture distribution profile comparable to the one acquired with the SPI T_2^* mapping. Measurements on the five cm long 0.60 w/c ratio were undertaken at two days. Only one of the three samples was also tested at 12 days. This was performed to demonstrate the use of the three-magnet array on time-based studies.

4-2.3.4 Saturated hydraulic conductivity of mortars

Moisture content profiles obtained with both techniques were processed using the Hydrus 1D software (Šimůnek, van Genuchten, & Šejna, 2016). This software, based on Richard´s equation (Eq. 4.2), was used in the inverse modeling mode to extract the saturated hydraulic conductivity (K_s) of the mortar samples. The parameters employed for the 0.35 w/c ratio mortar samples were saturated water content $q_s = 0.179\ m^3/m^3$, residual water content $q_r = 0.02\ m^3/m^3$, tortuosity l (-) = -0.50, a parameter describing the pore structure of the medium n (-) = 3.25, and a scale parameter inversely proportional to the mean pore diameter a (m^{-1}). For the 0.60 w/c ratio mortar samples, the parameters were $q_s = 0.269\ m^3/m^3$, $q_r = 0.02\ m^3/m^3$, l (-) = -0.50, n (-) = 3.25. In both cases the fitting parameters were a and K_s. Details about the Hydrus software and the meaning of parameters required by the model can be found elsewhere (Radcliffe & Simunek, 2010).

$$\frac{\partial \theta}{\partial t} = \frac{\partial}{\partial x}\left(K(h)\frac{\partial h}{\partial x}\right) - S(h) \tag{4.2}$$

Where θ is the normalized moisture content, t is time after first contact of the sample with the external water reservoir, x is distance, h $[m]$ is pressure head, $K(h)$ $[m\ s^{-1}]$ is the unsaturated hydraulic conductivity, and $S(h)$ $[m^3\ m^{-3}s^{-1}]$ is a sink function.

4.3. Results and discussion

Figure 4.2 shows a typical behavior of the water absorption process in the mortar samples. A higher primary sorptivity was exhibited by the 0.60 w/c ratio sample, compared with the 0.35 w/c ratio mortar. This was expected due to the higher porosity of the 0.60 w/c ratio mortar. However, in both mortars the secondary sorptivities were similar, as found in previous research (Razieh Enjilela, Cano-Barrita, Komar, Boyd, & Balcom, 2018). These lower secondary sorptivities, observed after two days of testing, resulted from a lower rate of water absorption, which in turn means a lower rate of penetration of the wet front. This was the reason to undertake the NMR/MRI measurements after two days of water absorption.

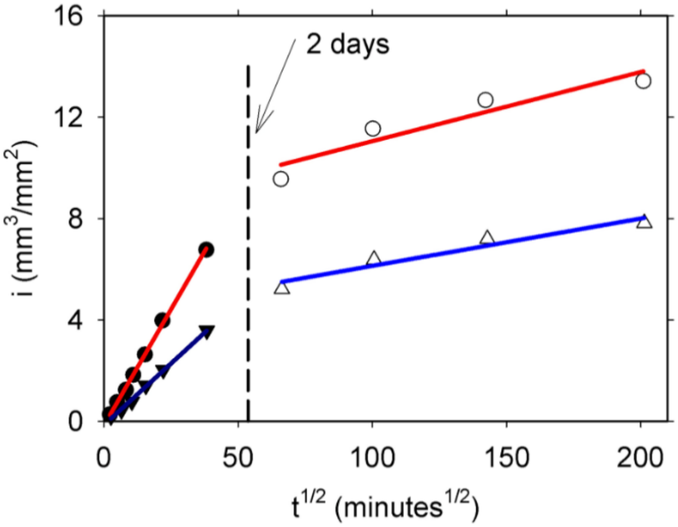

Figure 4.2. Cumulative water absorption per unit area versus the square root of time for 0.60 (circles) and 0.35 (triangles) w/c ratio mortars. Primary sorptivity (filled symbols) and secondary sorptivity (empty symbols).

Figure 4.3a shows CPMG decays in saturated and unsaturated regions of a 0.60 w/c ratio mortar sample. It was observed a faster decay of the CPMG measurement undertaken in the unsaturated region, compared with the decay in the saturated region. In the unsaturated region, the smallest pores (gel and small capillary pores) would be filled with water. In some cases, the high noise present in the CPMG decay made it difficult to observe the second pore population which always had low signal intensity. On the other hand, in the saturated region most of the pores were filled with water, including the large capillary pores. In these pores the water molecules relaxed slower than the small capillaries and gel pores, according to Equation 4.3 (Halperin, Jehng, & Song, 1994).

$$\frac{1}{T_2} = \rho \frac{S}{V} \tag{4.3}$$

where $1/T_2$ is the relaxation rate, r is the surface relaxivity, and S/V is the surface-to-volume ratio of the pore system.

The inverse Laplace Transform of the decays presented in Figure 4.3a, are given in Figure 4.3b. It is considered a proxy of the water-filled pore size distribution. It was assumed that at the beginning of the water absorption process, the microstructure at various positions along the sample was similar. However, as water entered there was a pore size rearrangement in the wet region (Fischer, Haerdtl, & McDonald, 2015b), as well as filling the empty pore space that contributed to the CPMG signal. A higher signal intensity was observed in the saturated zone, indicating a higher amount of water in the pore space compared with the unsaturated zone, as expected.

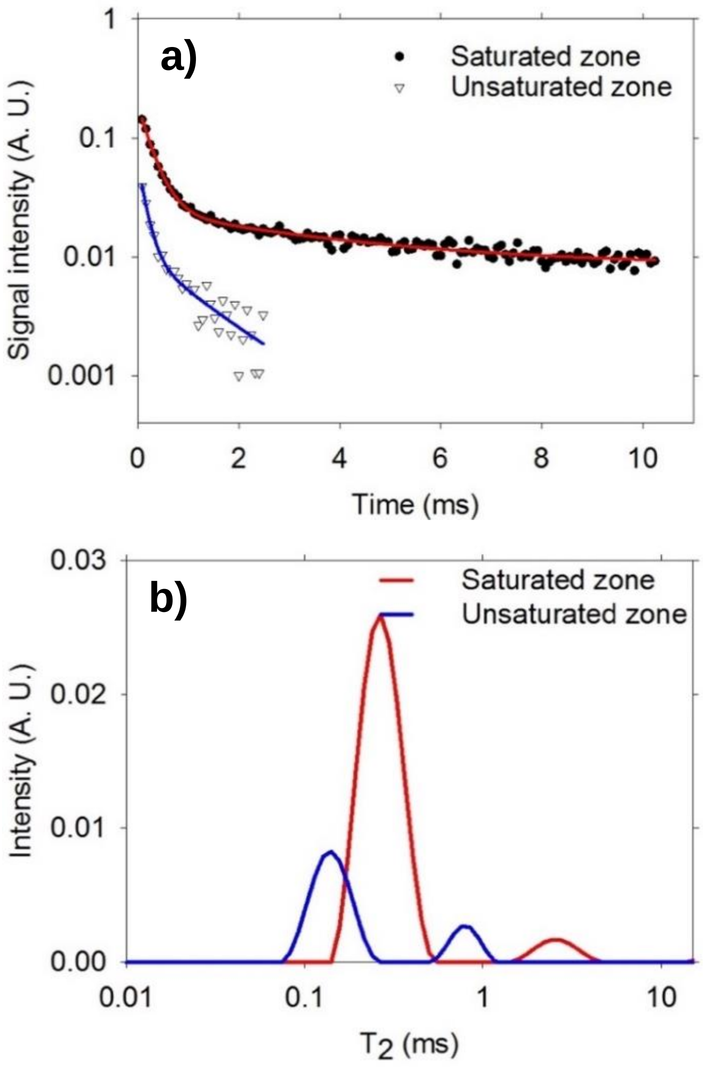

Figure 4.3. a) CPMG decay in saturated and unsaturated zones of a 0.60 w/c ratio mortar sample, and b) T_2 distributions corresponding to the CPMG decays shown in a).

Figure 4.4 shows the moisture profiles of the 0.60 w/c ratio samples with 100 mm in length. The T_2^* mapping was necessary to eliminate the T_2^* weighting affecting the NMR signal, which in turn would affect the shape of the profile in zones with different T_2^* lifetimes (Razieh Enjilela et al., 2018). In case of the MRI measurements, the sample was displaced three centimeters from the first position to acquire a second profile that overlapped with the first one. However, the sample length was not a problem when using the three-magnet array that did not have any restriction on the sample size. The profiles obtained with both techniques were remarkably similar in regions of higher water content but did not agree completely in the lower water content region.

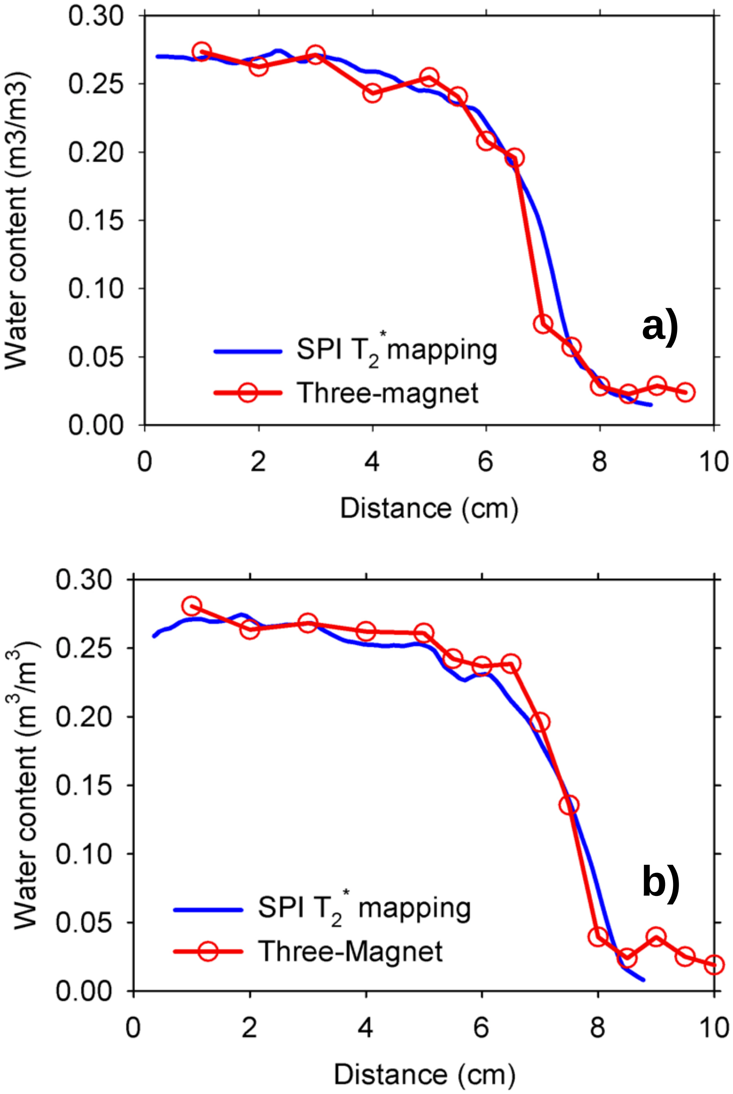

Figure 4.4 Water content distribution from SPI T_2^* mapping and CPMG signal intensity for the 0.60 w/c ratio, 100 mm long similar mortar samples (a and b) at four days of water absorption. Profiles with the T_2^* mapping were obtained by moving the sample in two steps due to the sample length restriction of the MRI instrument.

Results of the 0.35 w/c ratio, 100 mm mortar samples are shown in Figure 4.5. In spite of the lower water content compared with the 0.60 w/c ratio samples, the NMR measurements with the three-magnet array was nevertheless possible on these samples. Penetration of the wet front was reduced compared with the samples shown in Figure 4.4, as expected, because of the lower permeability of low w/c ratio cement-based materials. A similar moisture content profile was obtained, compared with the profile acquired with the SPI T_2^* mapping technique. Because of the inferior quality of the CPMG signal acquired at the lower moisture content region (right-hand side), fitting a bi-exponential decay function was not possible. Alternatively, the signal intensity of the first echo was taken as the moisture content in those point positions.

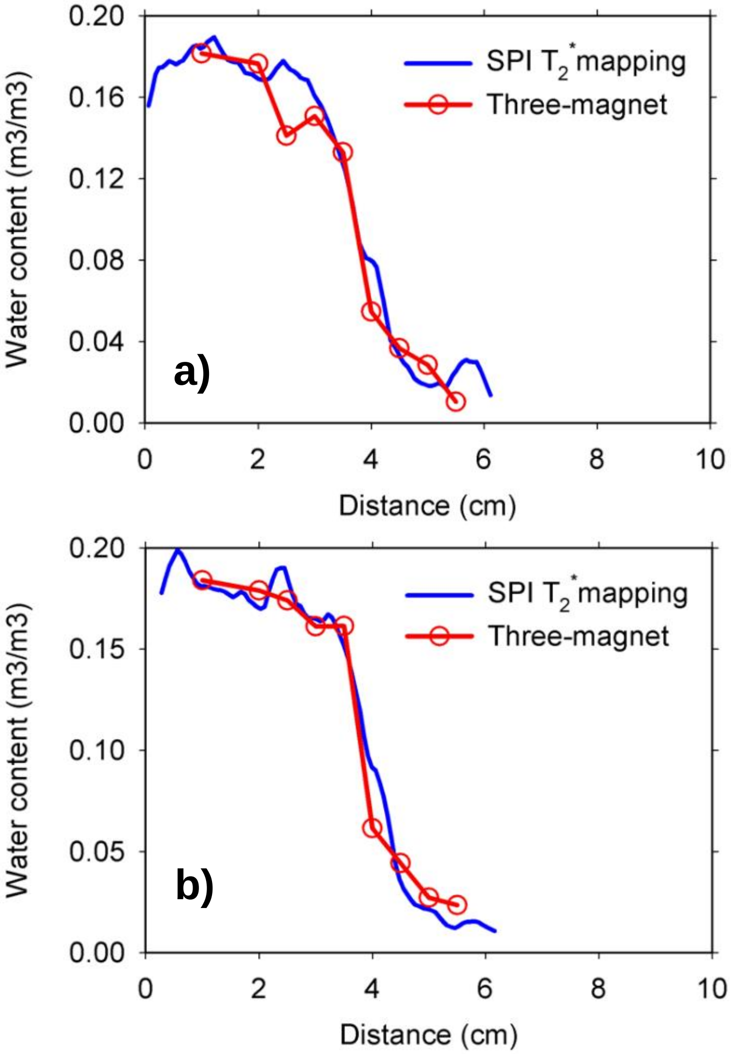

Figure 4.5. Water content distribution from SPI T_2^* mapping and CPMG signal intensity for the 0.35 w/c ratio, 100 mm long similar mortar samples (a and b) at four days of water absorption.

Figure 4.6 shows an example of the results obtained with the inverse modeling procedure with the Hydrus 1D software (Šimůnek et al., 2016). These results correspond to the 0.60 w/c ratio mortar. The r^2 for regression of fitted versus experimental data in the profiles from all the samples was higher than 0.96. The K_s values obtained from the SPI profiles and the CPMG signal intensities for the four samples are given in Table 4.1. It showed similar K_s values for samples with identical w/c ratio, as expected. The mortar with a lower w/c ratio possessed a lower saturated hydraulic conductivity than the high w/c ratio mortar, as it is already established in the literature (Neville, 1995). These results demonstrated the capability of the three-magnet array to acquire valuable data to extract transport properties of the mortars.

Table 4.1. Saturated hydraulic conductivity K_s values of the 0.60 and 0.35 w/c ratio mortars, obtained from inverse modeling using the Hydrus 1D software.

Sample	w/c ratio	K_s (m/s) SPI-MRI	K_s (m/s) Three-Magnet array
1	0.60	7.63×10^{-12}	7.33×10^{-12}
2	0.60	7.97×10^{-12}	7.88×10^{-12}
3	0.35	1.37×10^{-12}	1.36×10^{-12}
4	0.35	1.55×10^{-12}	1.35×10^{-12}

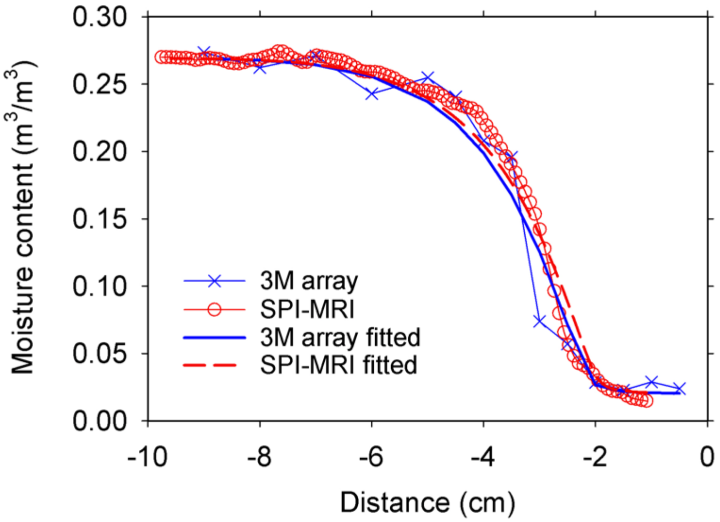

Figure 4.6. Experimental and fitted moisture distribution profiles of a 0.60 w/c ratio mortar sample. The experimental profiles were acquired with the three-magnet array and the SPI T_2^* mapping MRI technique. Fitted profiles were obtained by inverse modeling with the Hydrus software.

A comparison of the profiles obtained with the three-magnet array and the T_2^* mapping on the 5 cm long samples is presented in Figure 4.7. The three samples showed similar moisture distribution and wet front position. These 0.60 w/c ratio mortar samples were conditioned at ambient laboratory environment for one year before undertaking the water absorption experiments. The effect of this conditioning on the samples is shown as a relatively high moisture content in right-hand side of figures 4.7a, 4.7b, and 4.7c. This moisture content represents a more realistic level of moisture this mortar would have in the field, compared with oven drying at 50 ^{o}C. Additionally, the three-magnet array may be used to undertake time-based studies, as shown in Figure 4.7c (profiles obtained at 2 and 12 days of water absorption).

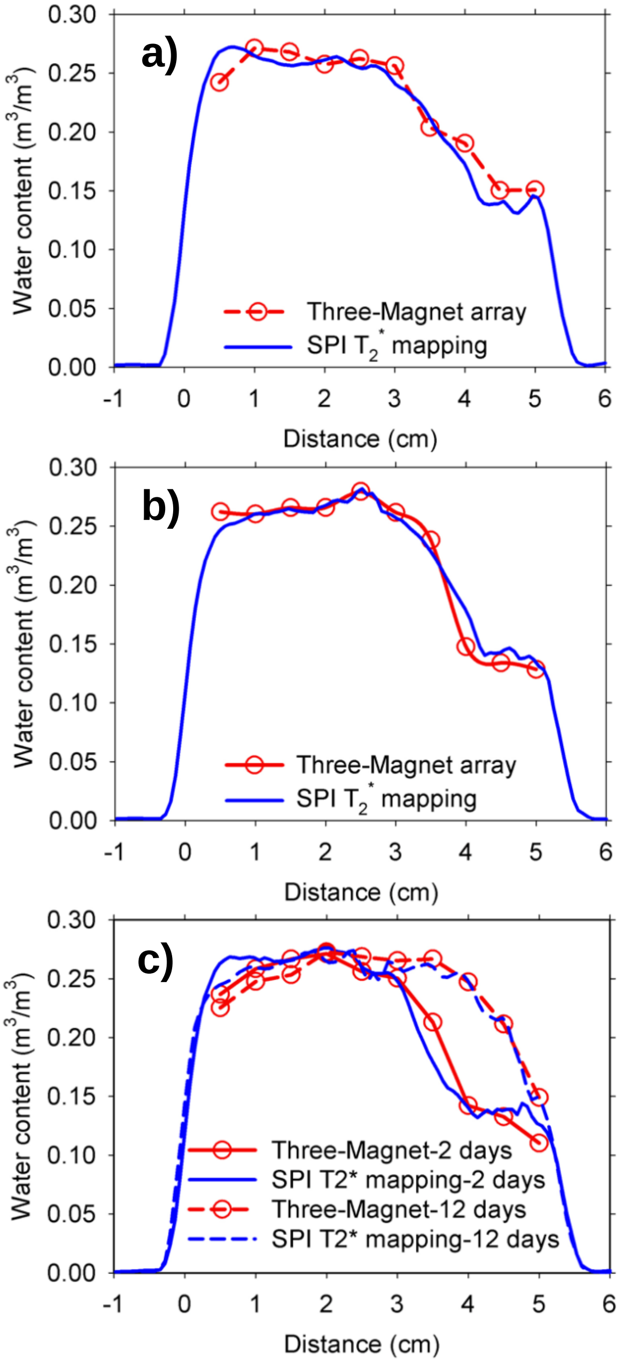

Figure 4.7. Moisture content profiles obtained with the Three-magnet array with an elliptical surface RF coil, and the T_2^* mapping with the SPI technique on three 0.60 w/c ratio mortar samples, a) and b) at two days of water absorption, and c) at two and 12 days of water absorption.

Figure 4.8 shows the ILT of the CPMG decays obtained along the length of one of the samples shown in Figure 4.7. There were two pore populations with longer T_2 values starting at the absorbing face and continuing along the region with high water content. This indicated that most of the pore space (gel and capillary) is filled with water. In some cases, only one pore population was observed (e.g. 1.5 cm and 2.5 cm). This was because of the noise in the signal that made it difficult to resolve the second pore population. In contrast, the unsaturated zone exhibits mainly one pore population with shorter T_2 values comprising mainly small pores (gel and small capillaries) filled with water during conditioning at ambient temperature and relative humidity.

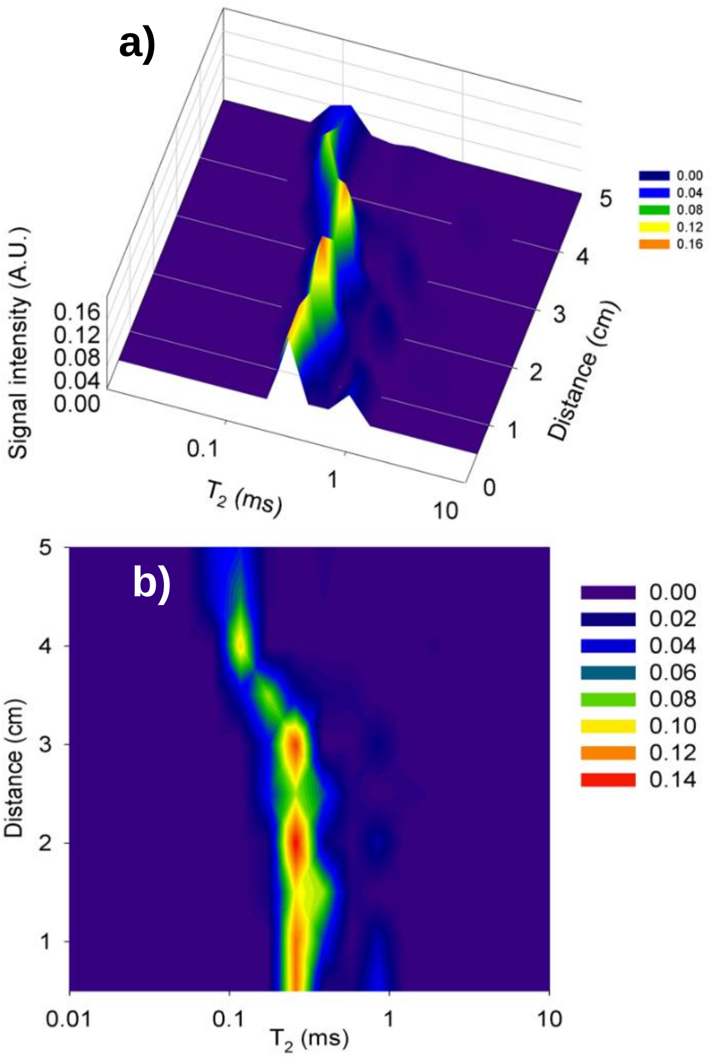

Figure 4.8. T_2 lifetime distributions along the length of a 0.60 w/c ratio mortar sample obtained by Inverse Laplace Transformation of the CPMG decays from the mortar sample shown in Figure 7a, at 2 days of water absorption a) 3D view and b) 2D view.

The correlation between the moisture content obtained at the same position in the mortar samples, using both techniques is shown in Figure 4.9. A high determination coefficient was obtained (r^2 = 0.97), indicating the suitability of the three-magnet array to acquire relative moisture content values that are comparable to those obtained with magnetic resonance imaging techniques like SPI T_2^* mapping. The three-magnet array does not have restriction on the sample size, compared with the MRI system used for imaging the moisture content profiles. In addition, its nondestructive nature is advantageous compared with destructive techniques like slicing the sample for oven drying (Šelih & Bremner, 2006), which requires preparing several samples to be tested, in addition to a lower spatial resolution of the profile. The CPMG decays do not require corrections like those needed on the measured intensity in neutron radiography, which may be a source of uncertainties on the moisture profiles (Villmann et al., 2014). The three-magnet array with the elliptical RF coil can be even used in spatial movements of 0.25 cm, which will increase the spatial resolution as demonstrated in previous research (Díaz-Díaz et al., 2020). These measurements were not aimed for water absorption times when the wet front position changed rapidly during the NMR measurements. This is because the shape of the signal intensity profiles (evaporable water content) would be unreliable.

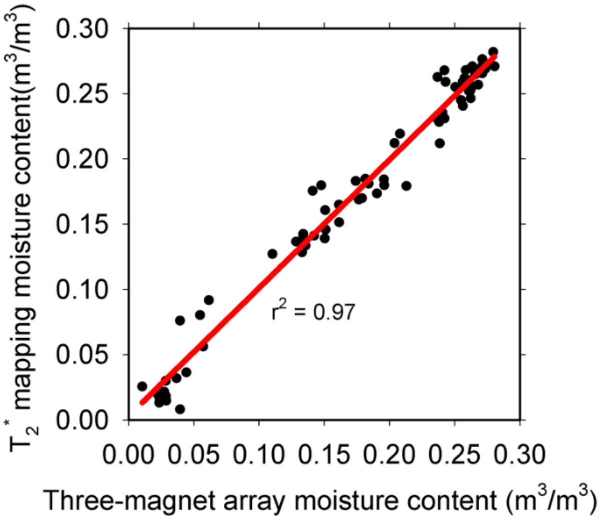

Figure 4.9. Three-magnet array moisture content versus the moisture content obtained with the T_2^* mapping of all the mortar samples tested.

The T_2^* of water in the concrete sample, obtained by a free induction decay with the Maran DRX HF 12/50 instrument, was in the order of 20 μs. This very short T_2^* lifetime precluded acquisition of an SPI profile even with the shortest encoding time (t_p = 50 μs) that could be used in this system. This sample contained normal weight aggregate (river sand and crushed limestone coarse aggregate) used in commercial concrete production. These aggregates typically contain iron oxide in its composition in a range of about 1 % to even 10 %. This amount of iron, additional to the iron present in the ordinary Portland cement, enhanced relaxation of the protons, therefore reducing the T_2^* and T_2 lifetimes. Figure 4.10a is a photograph of the concrete sample used for the NMR measurements, clearly showing the coarse aggregates. Figure 4.10b is the CPMG signal intensity (moisture content) profile along the length of the sample. The dips observed in the profile (e.g. at 1.5 and 3.5 cm) corresponded to the presence of coarse aggregates that reduced the intensity of the NMR signal. The reason for this was the low absorption of the aggregates, usually less than 2 %. The CPMG profiles in concrete samples could be improved by undertaking a second or a third measurement at the same distances but in another line in the rotated sample (90 º or 180 º). An average of the signal intensities at each point position can be taken. This will undoubtedly increase the measurement time for each sample but would produce a better profile.

Finally, the NMR measurements using the three-magnet array with the elliptical surface RF coil can be extended to monitoring moisture distribution in processes like drying of cement-based materials or other porous materials like wood, rocks or food. It can also be used to monitor microstructural changes in samples as a function of position (effect of curing conditions on the cover concrete) or as a function of time. Measurements in samples much larger than the ones used in this study still possible by displacing the three-magnet array over the sample´s surface.

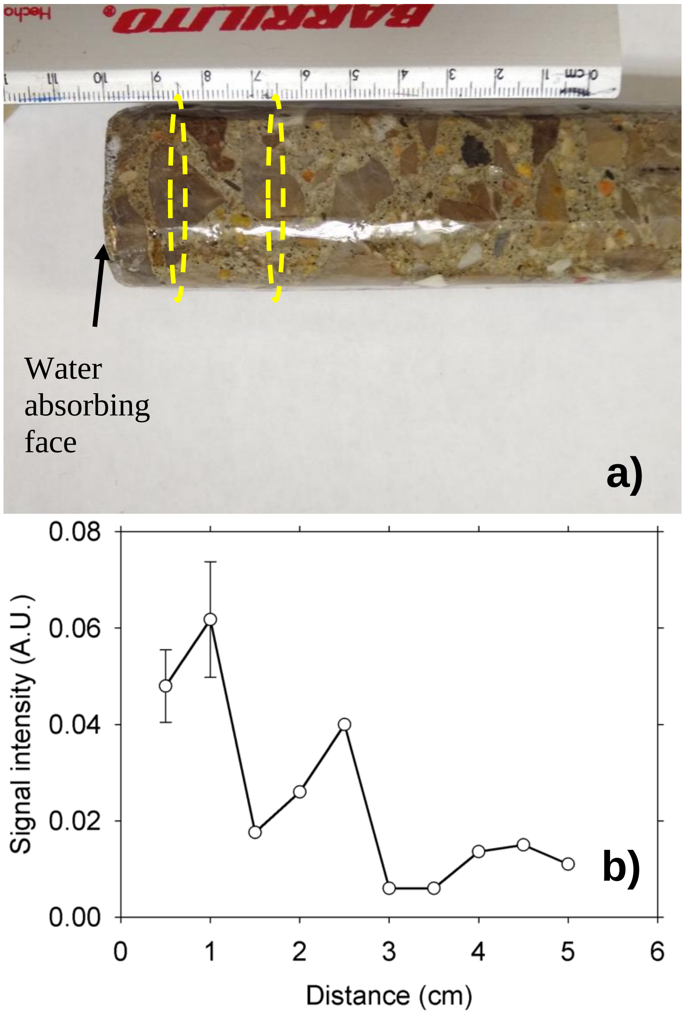

Figure 4.10. a) Picture of the 0.60 w/c ratio concrete sample. The dotted ellipses show the approximate position of the RF coil during the NMR measurements at positions 1.5 and 3.5 cm where the presence of coarse aggregates reduced the signal intensity, and b) CPMG signal intensity after five days of water absorption. The sample error bars represent the uncertainty in the estimation of the intensity. In the low signal intensity points (≥ 3 cm), an average of the first two echoes of the CPMG decay was taken because of the low signal to noise ratio that precluded fitting of the data to an exponential decay function.

4.4 Conclusions

This paper has shown the use of a three-magnet array with an elliptical surface RF coil to determine moisture content at various positions along mortar and concrete samples during water absorption experiments. Based on this study, the following conclusions are drawn:

- A three-magnet array with an elliptical surface RF coil operating at a frequency of 4.67 MHz, allows determination of the NMR signal along mortar and concrete samples containing ordinary materials and with no limitation on the sample size.
- In the concrete sample the very short NMR signal lifetime (T_2^* = 20 ms) caused by the paramagnetic impurities in the material precluded the acquisition of an MRI profile.
- There is a linear relationship between the signal intensities (moisture content) obtained with the three-magnet array and the corresponding signal intensities from MRI profiles taken as a reference (r^2 = 0.97).
- Similar values of saturated hydraulic conductivity (K_S) of mortar samples with identical w/c ratio were obtained from the profiles acquired by the two techniques outlined in this paper, demonstrating the feasibility of the three-magnet array with an elliptical surface RF coil to acquire valuable data for transport properties determination of cement-based materials.

Acknowledgements

P. Cano acknowledges funding by Conacyt from Mexico under grant number 239727, and by SIP from Instituto Politécnico Nacional (IPN) under the grant 20180029. F. Diaz acknowledges Conacyt for the scholarship given for his PhD studies, as well as to IPN for the BEIFI scholarship.

4.5 References

ASTM C1585-13. (2013). *Standard Test Method for Measurement of Rate of Absorption of Water by Hydraulic Cement Concretes*. *ASTM International* (Vol. 41). West Conshohocken, PA,USA. https://doi.org/10.1520/C1585-13.2

Balcom, B. J., Barrita, J. C., Choi, C., Beyea, S. D., Goodyear, D. J., & Bremner, T. W. (2003). Single-point magnetic resonance imaging (MRI) of cement based materials. *Materials and Structures*, *36*(257), 166–182.

Beyea, S. D., Balcom, B. J., Prado, P. J., Cross, A. R., Kennedy, C. B., Armstrong, R. L., & Bremner, T. W. (1998). Relaxation time mapping of short T*2 nuclei with single-point imaging (SPI) methods. *Journal of Magnetic Resonance*, *135*, 156–164. https://doi.org/10.1006/jmre.1998.1537

Cano-Barrita, P. F. de J., Balcom, B. J., & Castellanos, F. (2017). Carbonation front in cement paste detected by T 2 NMR measurements using a low field unilateral magnet. *Materials and Structures*, *50*, 1–8. https://doi.org/10.1617/s11527-017-1019-5

Coates, G. R., Xiao, L., & Prammer, M. G. (1999). *NMR Logging principles & applications*. (R. F. Sigal & S. J. Bollich, Eds.). Houston, Texas, USA: Halliburton Energy Services.

Díaz-Díaz, F., Cano-Barrita, P. F. D. J., León-Martínez, F. M., & Castellanos, F. (2020). Unilateral low-field magnetic resonance measurements of carbonation depth in unsaturated and saturated Portland cement mortars. *Cement and Concrete Research*, *138*. https://doi.org/10.1016/j.cemconres.2020.106237

Emid, S., & Creyghton, J. H. N. (1985). High Resolution NMR Imaging in Solids. *Physica*, *128B*, 81–83. https://doi.org/10.1016/0378-4363(85)90087-7

Enjilela, R., Cano-Barrita, P. . de J., Komar, A., Boyd, A. J., & Balcom, B. J. (2017). Monitoring steady state moisture distribution during wick action in mortar by magnetic resonance imaging (MRI). *Materials and Structures*. https://doi.org/10.1617/s11527-017-1017-7

Enjilela, Razieh, Cano-Barrita, P. F. de J., Komar, A., Boyd, A. J., & Balcom, B. J. (2018). Wet front penetration with unsteady state wicking in mortar studied by Magnetic Resonance Imaging (MRI). *Materials and Structures*, *51*. https://doi.org/10.1617/s11527-018-1142-y

Fischer, N., Haerdtl, R., & McDonald, P. J. (2015a). Is colour change a good measure of a water penetration front? *Magazine of Concrete Research*, *67*(19), 1048–1053. https://doi.org/10.1680/macr.14.00354

Fischer, N., Haerdtl, R., & McDonald, P. J. (2015b). Observation of the redistribution of nanoscale water filled porosity in cement based materials during wetting. *Cement and Concrete Research*, *68*, 148–155. https://doi.org/10.1016/j.cemconres.2014.10.013

Garcia-Naranjo, J. C. (2012). *Three-Magnet Arrays for Unilateral Magnetic Resonance*. PhD Thesis, University of New Brunswick, Canada.

García-naranjo, J. C., Guo, P., Marica, F., Liao, G., & Balcom, B. J. (2014). Magnetic Resonance Core-Plug Analysis with the Three-Magnet Array Unilateral Magnet. *Petrophysics*, *55*(3), 229–239.

Hall, C. (1989). Water sorptivity of mortars and concretes: a review. *Magazine of Concrete Research*, *41*(147), 51–61. https://doi.org/10.1680/macr.1989.41.147.51

Halperin, W. P., Jehng, J. Y., & Song, Y. Q. (1994). Application of spin-spin relaxation to measurement of surface area and pore size distributions in a hydrating cement paste. *Magnetic Resonance Imaging*, *12*, 169–173.

Hilsdorf, H., & Kropp, J. (2004). *Performance Criteria for Concrete Durability*. Taylor & Francis.

Lamason, C., Macmillan, B., Balcom, B., Leblon, B., & Pirouz, Z. (2015). Water content measurement in black spruce and aspen sapwood with benchtop and portable magnetic resonance devices. *Wood Material Science & Engineering*, *10*(1), 86–93. https://doi.org/10.1080/17480272.2015.1010573

Meiboom, S., & Gill, D. (1958). Modified Spin-Echo Method for Measuring Nuclear Relaxation Times. *Review of Scientific Instruments*, *29*(8), 688–91.

Neville, A. M. (1995). *Properties of Concrete* (4Thl Editi). Harlow, Essex, England: Longman Group Limited.

Radcliffe, D. E., & Simunek, J. (2010). *Soil Physics with Hydrus - Modeling and Applications*. New York, USA: CRC Press, Taylor & Francis Group.

Šelih, J., & Bremner, T. W. (2006). Drying of saturated lightweight concrete: an experimental investigation. *Materials and Structures*, *29*(7), 401–405. https://doi.org/10.1007/bf02485989

Šimůnek, J., van Genuchten, M. T., & Šejna, M. (2016). Recent Developments and Applications of the HYDRUS Computer Software Packages. *Vadose Zone Journal*, *15*(7), 1–25. https://doi.org/10.2136/vzj2016.04.0033

Villmann, B., Slowik, V., Wittmann, F. H., Vontobel, P., & Hovind, J. (2014). Time-dependent moisture distribution in drying cement mortars: results of neutron radiography and inverse analysis of drying tests. *Restoration of Buildings and Monuments*, *20*(1), 49–62. https://doi.org/10.12900/RBM14.20.1-0004

Capítulo 5. Detección de ^{35}Cl y ^{23}Na en soluciones de NaCl y en pastas de cemento saturadas con NaCl

Resumen

La penetración de iones cloruro es importante en estudios de durabilidad de estructuras de concreto, y su determinación es comúnmente a través de técnicas destructivas como la extracción de polvo de concreto a distintas profundidades para conocer la concentración espacial del ion cloruro. Esta investigación exploró la detección de señales de RMN de ^{23}Na y ^{35}Cl en campo magnético bajo. Se utilizó un arreglo de magnetos de un sistema de imagenología por RMN comercial con campo $B_0 = 0.302$ T, con *shims* activos para homogeneizar el campo B_0. También se utilizó un arreglo Halbach de magnetos con $B_0 = 1.028$ T. Para cada arreglo se diseñaron y construyeron dos antenas de RF, una para ^{23}Na y la otra para ^{35}Cl. Se prepararon disoluciones con diferente concentración de NaCl y tres especímenes de pasta de cemento (relación a/c = 0.55) saturadas con soluciones de NaCl. Se realizaron mediciones FID y CPMG para obtener señales RMN que fueron ajustadas a una función de decaimiento exponencial para obtener T_2^* y T_2, así como sus respectivas intensidades. Se obtuvo, para ambos núcleos, una relación lineal entre la intensidad de la señal de RMN con las concentraciones de disoluciones de NaCl desde 0.175 M hasta 5.6 M ($r^2 > 0.96$). Con las antenas construidas para el arreglo con *shims* activos fue posible obtener señal de ^{23}Na de las pastas de cemento saturadas al vacío con distintas soluciones de NaCl, pero no del ^{35}Cl, lo cual se explica por la baja sensibilidad de este núcleo comparado con el ^{1}H y el ^{23}Na. Con el arreglo Halbach solo se pudo detectar señal de ^{23}Na y de ^{35}Cl en las soluciones de NaCl.

Palabras clave: *RMN, cloruro, sodio, tiempo de vida* T_2^* *y* T_2

5.1 Introducción

Una de las principales causas de deterioro del concreto reforzado es la corrosión del acero de refuerzo ocasionada por el ataque de iones cloruro (Neville, 1995). Estos ingresan por medio de absorción capilar y difusión a través del recubrimiento del concreto hasta alcanzar la superficie del acero de refuerzo. Con cierta concentración de cloruros al nivel del acero de refuerzo, se destruye la capa pasiva de óxido de fierro que protege al acero y en presencia de agua y oxigeno se inicia la corrosión (Neville, 1995).

Los métodos más comunes utilizados para medir la profundidad de penetración de cloruros en el concreto son destructivos. Tal es el caso del método colorimétrico (Baroghel-Bouny, Belin, Maultzsch, & Henry, 2007) que consiste en rociar una solución de nitrato de plata en la superficie de una muestra recién fracturada, donde la parte cerca de la superficie del concreto se torna en un color blanquecino. Esto indica la presencia de iones cloruro, mientras que la parte que se torna color marrón corresponde a la zona libre de iones cloruro. Otra técnica ampliamente utilizada para determinar la profundidad de penetración de consiste en la extracción de muestras de polvo de concreto a distintas profundidades. La concentración de iones cloruro se determina por medio de titulación potenciométrica. De la concentración de iones cloruro versus profundidad se estima el coeficiente de difusión de cloruros (NT Build 443, 1995) y la concentración en la superficie al ajustar los datos a la solución de la segunda ley de Fick. Sin embargo, esta técnica también es destructiva y requiere de tiempo considerable para su realización.

La resonancia magnética nuclear (RMN) es una técnica no destructiva que ha sido utilizada para estudiar la hidratación de cemento Portland (Lahajnar et al., 1977; Miljkovc, Lasic, MacTavish, & Pintar, 1988) y el desarrollo de su estructura porosa (Plassais et al., 2001). También ha sido utilizada para estudiar iones cloruro (^{35}Cl) en cemento hidratado (Yun et al., 2004) y la detección de ^{23}Na en rocas (Rijniers, Magusin, Huinink, Pel, & Kopinga, 2004). La imagenología por RMN ha sido utilizada para obtener perfiles de humedad en concreto durante secado (Balcom et al., 2003), absorción capilar de agua (R. Enjilela, Cano-Barrita, Komar, Boyd, & Balcom, 2018; Razieh Enjilela, Cano-Barrita, Komar, Boyd, & Balcom, 2017), así como para obtener perfiles durante la penetración de iones cloruro y sodio en materiales base cemento (Cano, Bremner, Mcgregor, & Balcom, 2002; Pel, Donkers, Kopinga, & Noijen, 2016). No obstante, estos estudios normalmente han sido realizados utilizando sistemas de RMN de campo alto con magnetos superconductores, los cuales tienen el inconveniente de ser de alto costo de adquisición y de mantenimiento. A pesar de que algunos sistemas ya utilizan magnetos permanentes de bajo campo como el MOLE (Manz et al., 2006) y el MOUSE (Blümich et al., 1998), actualmente su costo en el mercado sigue siendo relativamente alto. También se han desarrollado otros sistemas unilaterales de bajo campo como el arreglo de tres magnetos (García-Naranjo, Guo, Marica, Liao, & Balcom, 2014), el cual genera un campo relativamente homogéneo para una frecuencia de 2.25 MHz. Por otra parte, estos sensores están diseñados sólo para detectar señal del hidrógeno (^1H).

Por lo tanto, el presente trabajo explora la posibilidad de obtener señales de RMN de los núcleos ^{23}Na y ^{35}Cl en campo magnético bajo, utilizando los magnetos permanentes (B_0 = 0.302 Teslas) de un sistema comercial que posee shims activos para homogeneizar el campo B_0 , así como un arreglo Halbach de magnetos que genera un campo magnético B_0 de 1.028 Teslas.

5.2 Materiales y método

5.2.1 Diseño y construcción de antenas para el arreglo de magnetos del sistema comercial Maran DRX HF 12/50

Se utilizó el arreglo de magnetos de un sistema MARAN DRX-HF 12/50 (Oxford Instruments Ltd, Abingdon, Oxford, UK) que opera a una frecuencia de 12.9 MHz (B_0 = 0.302 Teslas) mostrado en la Figura 5.1. Este arreglo cuenta con *shims* activos que consiste en un set de pequeñas bobinas utilizadas para incrementar la homogeneidad del campo magnético. Los magnetos permanentes se mantienen a 35 °C por medio de un sistema de control de temperatura.

Figura 5.1 Arreglo de magnetos permanentes de un espectrómetro MARAN DRX-HF 12/50

Se construyó una antena de radio frecuencia tipo solenoide con lámina de cobre de 0.1 mm de espesor y 5 cm de ancho, la cual consistió en 13 espiras, con una longitud de 11 cm y diámetro de 5.4 cm. La frecuencia de resonancia (3.4 MHz) para el ^{23}Na se calculó con la ecuación de Larmor (Ecuación. 5.1), utilizando la relación giromagnética γ = 11.26 MHz/T y el campo magnético B_0 = 0.302 T generado por el arreglo de magnetos. Esta antena fue montada sobre una base cilíndrica de acetato y fue colocada en el interior de una caja de Faraday construida con placas de circuito impreso, como se muestra en la figura 5.2a. La antena se sintonizó a la frecuencia calculada utilizando capacitores cerámicos fijos y variables (Voltronics Corp, Salisbury, Maryland, USA), de acuerdo con el diagrama eléctrico de la figura 5.2b.

$$\omega = \gamma . B_0 \tag{5.1}$$

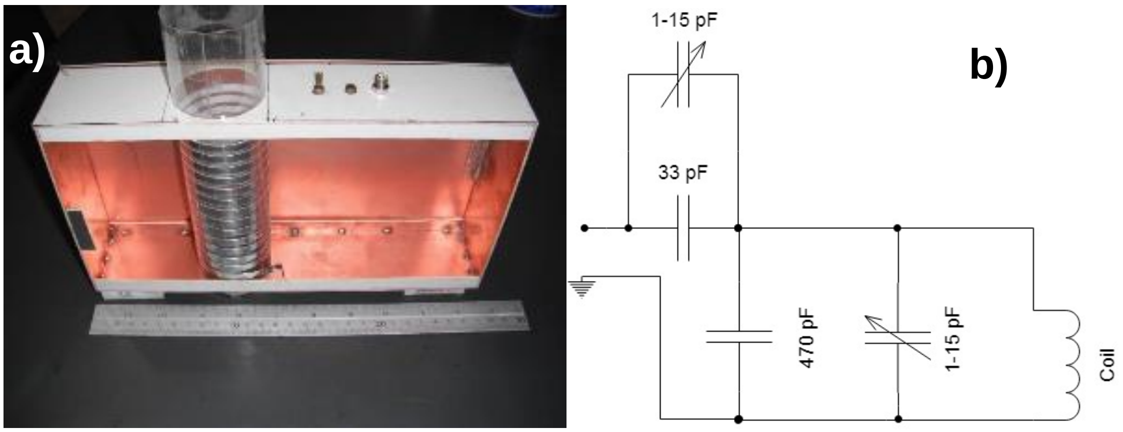

Figura 5.2 Antena de RF sintonizada a la frecuencia del ^{23}Na para el arreglo de magnetos del sistema comercial Maran DRX HF 12/50, a) Caja de Faraday con la antena y capacitores fijos y variables y b) Circuito equivalente de la antena.

El factor de calidad Q de la antena, calculado con las ecuaciones 5.2 y 5.3 fue igual a 11.

$$Q = \frac{f_0}{\Delta f} \tag{5.2}$$

$$\Delta f = f_2 - f_1 \tag{5.3}$$

donde f_0 es la frecuencia central, Δf es el ancho de banda la cual se obtiene con la ecuación 5.3, f_1 y f_2 son las frecuencias en donde la señal reflejada decae 3 dB (Figura 5.3).

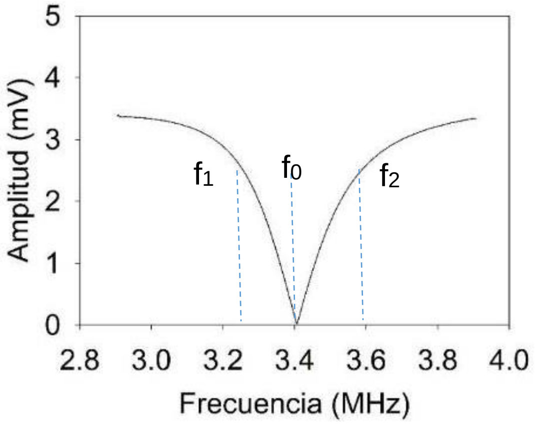

Figura 5.3 Respuesta en frecuencia de la antena para sodio ^{23}Na.

De igual manera se construyó una caja de Faraday para una antena sintonizada a la frecuencia de 1.26 MHz para el ^{35}Cl, cuya relación giromagnética es de γ = 4.17 MHz/T. En este caso el solenoide fue de las mismas dimensiones que la descrita anteriormente para el ^{23}Na, pero con 17 vueltas y la anchura de la cinta de cobre empleada para su construcción fue de 0.3 cm (Figura 5.4a). Los valores de capacitores empleados se muestran en el diagrama eléctrico de la figura 5.4b. El factor Q calculado con la ecuación 5.2 para esta antena fue de 6.63.

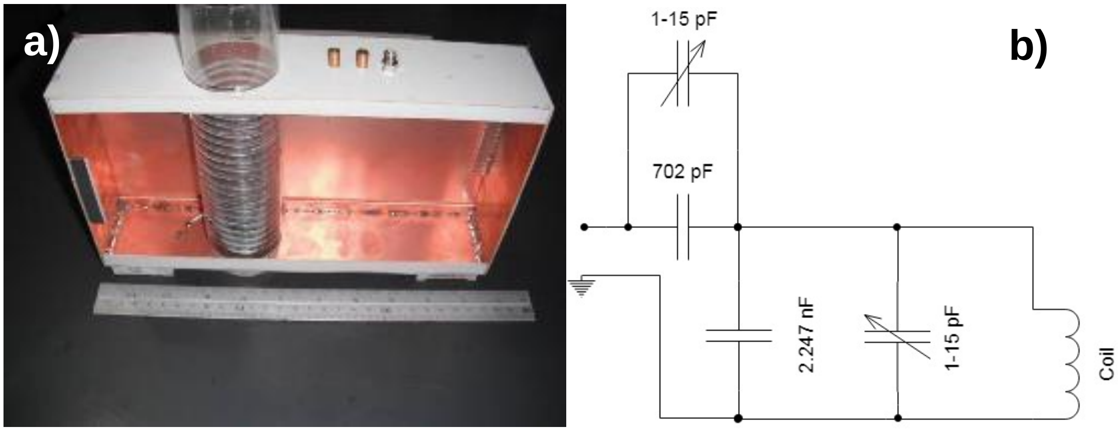

Figura 5.4 Antena de RF sintonizada a la frecuencia del ^{35}Cl para el arreglo de magnetos del sistema comercial Maran DRX HF 12/50, a) Caja de Faraday con la antena y b) Circuito equivalente de la antena.

5.2.2 Antenas para el arreglo Halbach de magnetos

Se utilizó un arreglo Halbach de magnetos comercial (e-Magnets UKTM, Berkhamsted, UK) mostrado en la Figura 5.5a donde las flechas indican la dirección de magnetización de cada pieza de magneto que conforman el arreglo y la dirección del campo magnético B_0 que se produce en el interior es a lo largo del eje Z.

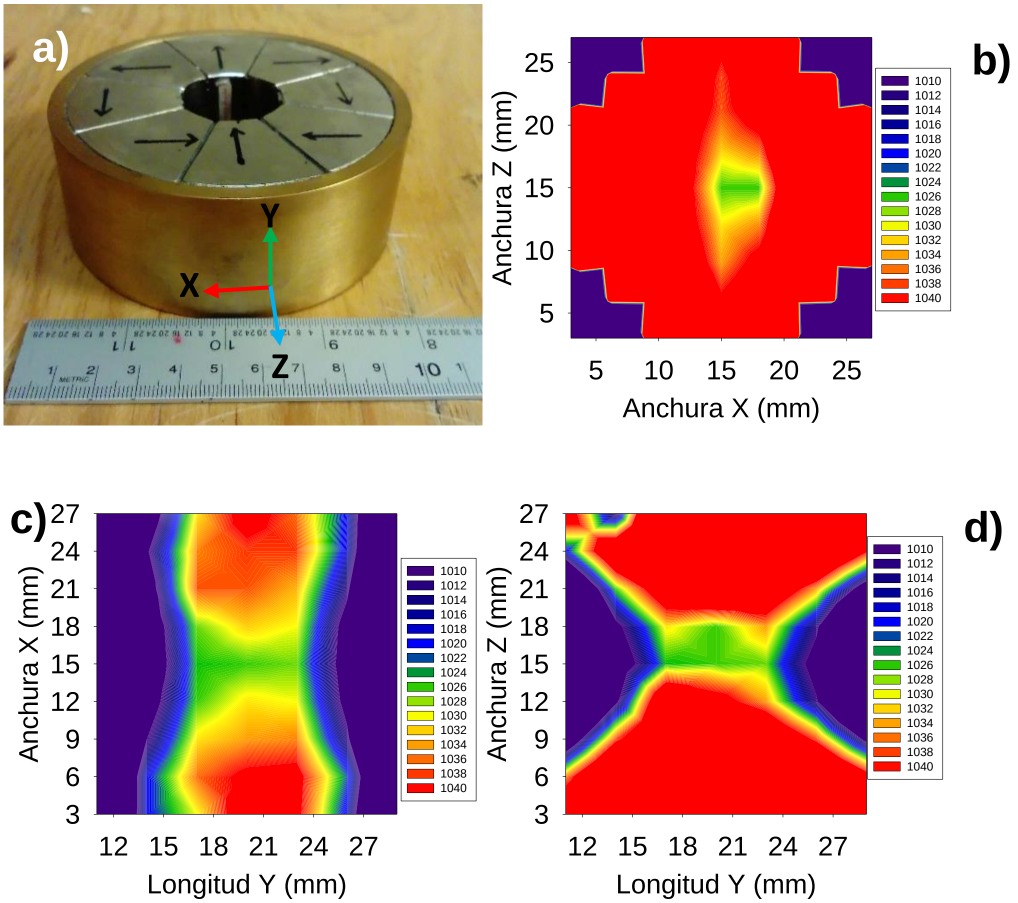

Figura 5.5 a) Arreglo Halbach de magnetos, b) Campo magnético medido en el plano XZ, c) Campo magnético medido en el plano YX y d) Campo magnético medido en el plano YZ.

Se realizaron mediciones del campo magnético en el interior del arreglo en los planos XZ, XY e YZ (Figura 5.5b, 5.5c y 5.5d) empleando una hoja cuadriculada a cada 3 mm y un gaussimetro HT-20 (Hangzhou Best Magnet Co. Ltd, Zhejiang, China) el cual tiene una resolución de 0.1mT. De esta manera se determinó una zona relativamente homogénea con forma similar a un cilindro de dimensiones 5 mm de diámetro por 10 mm de longitud en el interior del arreglo con un campo magnético B_0 de 1.028 T.

Se utilizó alambre de cobre calibre 32 AWG para construir dos antenas de RF tipo solenoide. La primera antena consistió en 17 espiras, con dimensiones de 13.5 mm de diámetro y 10 mm de longitud, que fue sintonizada para detectar núcleos de ^{23}Na a la frecuencia de 11.58 MHz (Figura 5.6a). La segunda consistió en 31 espiras, sus dimensiones fueron de 13.5 mm diámetro y 15 mm de longitud, la cual fue sintonizada a la frecuencia de 4.3 MHz para núcleos de ^{35}Cl (Figura 5.6b). En cada caso la frecuencia de sintonía fue calculada con la ecuación de Larmor de acuerdo con el campo magnético B_0 que se genera en el interior del arreglo Halbach y la relación giromagnética (γ) de cada núcleo.

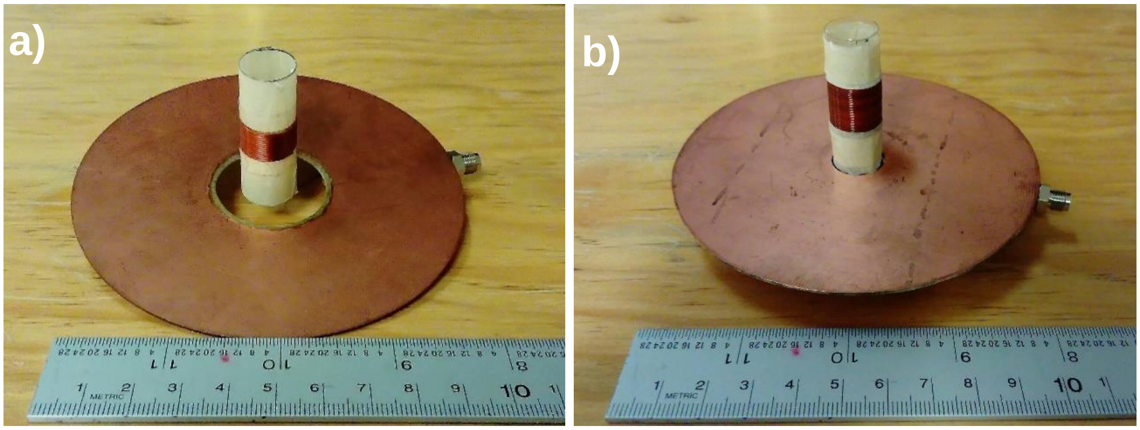

Figura 5.6 Antenas de RF construidas para el arreglo Halbach de magnetos, a) Antena sintonizada a la frecuencia del ^{23}Na y b) Antena sintonizada a la frecuencia del ^{35}Cl.

5.2.3 Preparación de las muestras

Se utilizó agua destilada y cloruro de sodio para preparar soluciones con diferente concentración molar de 0.175, 0.35, 0.70, 1.40, 2.10, 2.80, 3.50, 4.20, 4.90, y 5.60 M. Posteriormente las soluciones fueron colocadas en dos tamaños de portamuestras cilíndricas, unas de 5.35 cm de diámetro por 22.5 cm de altura (Figura 5.7a) y otras de 1 cm de diámetro por 9 cm de longitud (Figura 5.7b), de acuerdo con el espacio disponible en las antenas construidas para el arreglo de magnetos del sistema comercial MARAN DRX HF 12/50 y para el arreglo Halbach de magnetos, respectivamente.

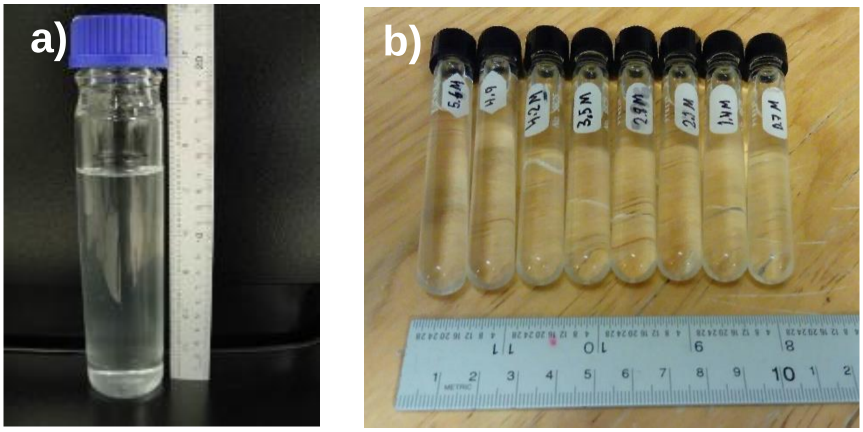

Figura 5.7 Portamuestras utilizadas para las soluciones de NaCl, a) para el arreglo de magnetos del sistema MARAN y b) para el arreglo Halbach de magnetos

También se prepararon tres especímenes de pasta de cemento Portland con relación a/c = 0.55 (Figura 5.8b), los cuales se secaron en horno a 80 ℃ durante 24 horas para eliminar parte del agua evaporable. Posteriormente fueron saturados al vacío con soluciones de NaCl a concentraciones de 1.4 M, 2.8 M y 4.9 M, con el objetivo de tener muestras con diferentes concentraciones de ^{23}Na y ^{35}Cl en su interior, lo cual debería reflejarse en la intensidad de la señal. Se realizaron mediciones con la técnica de decaimiento libre de la inducción (FID) para obtener el tiempo de relajación transversal efectivo T_2^* de las diferentes soluciones y de los especímenes de pasta de cemento, con las antenas construidas para el arreglo de magnetos del sistema Maran DRX HF 12/50. Por otra parte, se empleó la técnica CPMG para determinar tiempos de relajación T_2 de las diferentes soluciones con las antenas construidas para el arreglo Halbach de magnetos debido a que la homogeneidad de B_0 no fue suficiente para obtener FID. Los parámetros de medición se muestran en la Tabla 5.1.

Para determinar la amplitud y el tiempo de vida T_2^* y T_2 de las señales FID y CPMG respectivamente, las señales obtenidas fueron ajustadas a una función de decaimiento exponencial de una componente de acuerdo con la Ecuación 5.4.

$$S = S_0 \cdot e^{-\frac{t}{b}} \tag{5.4}$$

donde S es la intensidad de la señal, S_0 es la amplitud y b es T_2^* o T_2 según sea el caso de una FID o un CPMG.

Tabla 5.1. Parámetros empleados para la adquisición de señales FID y CPMG con los magnetos del sistema Maran y Halbach con las antenas construidas.

	Magneto Maran DRX HF 12/50			**Arreglo Halbach**	
	^{23}Na (3.41 MHz)		**^{35}Cl (1.26 MHz)**	**^{23}Na (11.58 MHz)**	**^{35}Cl (4.3 MHz)**
	Soluciones	**Pastas**	**Soluciones**	**Soluciones**	
Ancho de pulso (μs)	64	64	250	12	20
Amplitud de pulso (dB)	-1	-1	-1	-6	-6
Número de ecos	-	-	-	256	128
Tiempo de eco τ (μs)	-	-	-	300	1300
Número de escaneos	4096	4096	4096	4096	4096

5.3 Resultados y discusión

5.3.1 Tiempo de relajación T_2^* e intensidad para ^{23}Na y ^{35}Cl obtenido con el arreglo de magnetos del sistema Maran

Un ejemplo de señal del decaimiento libre de la inducción (FID) del ^{23}Na adquirida se muestra en la Figura 5.8 para una concentración de 5.6 M. La Figura 5.9 muestra la relación entre la amplitud de la señal con la concentración de NaCl. Se observó un incremento proporcional de la intensidad de la señal con un incremento de la concentración de NaCl en las soluciones, lo cual es debido a la presencia de una mayor cantidad de núcleos de sodio conforme se incrementa la concentración en las soluciones. Al realizar una regresión lineal de los datos, se obtuvo un coeficiente de determinación r^2 de 0.997l. Esta tendencia también se observó en los valores de amplitud de la señal detectadas en las pastas de cemento saturadas con soluciones de diferente concentración molar de NaCl (Figura 5.9b).

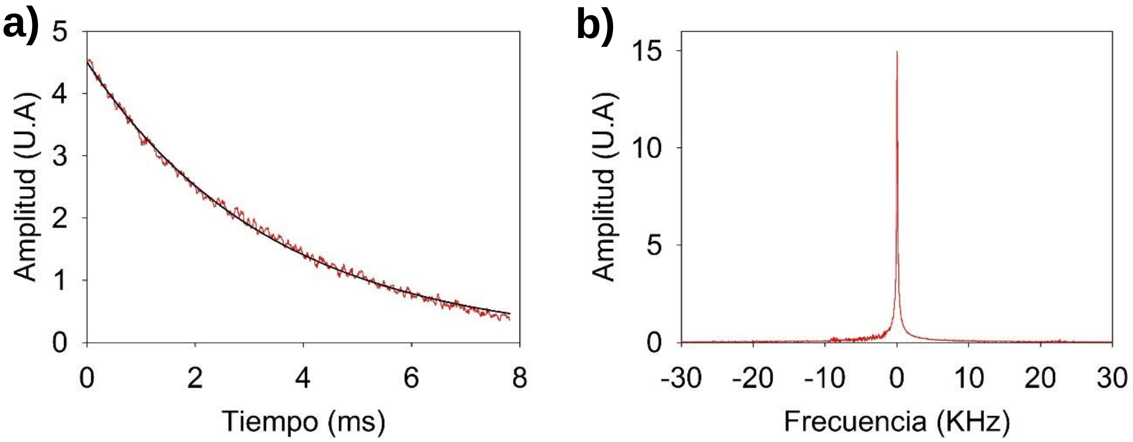

Figura 5.8. Señal de ^{23}Na detectada con la antena construida para los magnetos del sistema comercial Maran, a) Decaimiento de inducción libre (FID) y b) Espectro en frecuencia de la señal

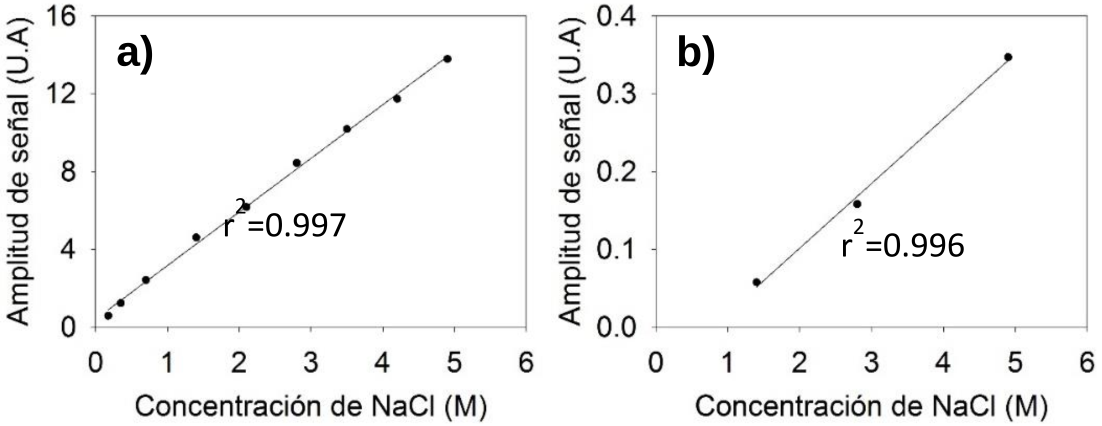

Figura 5.9. Amplitud de la señal ^{23}Na en función de la concentración molar de NaCl, a) En soluciones acuosas y b) En pastas de cemento Portland (a/c = 0.55) saturadas con soluciones a diferentes concentraciones de NaCl.

Por otra parte, los valores de T_2^* tanto en soluciones como en pastas saturadas (en estas últimas en menor medida) presentaron un comportamiento decreciente conforme incrementó la concentración del NaCl en las soluciones (Figura 5.10). Este comportamiento fue similar a lo reportado por Rijniers et al (Rijniers et al., 2004) con valores T_2 del ^{23}Na en soluciones a diferentes concentraciones de NaCl y en pastas saturadas con soluciones de NaCl. Este comportamiento se atribuyó a una mayor interacción spin-spin de los núcleos conforme se incrementa la concentración del NaCl, lo que ocasiona una mayor velocidad de decaimiento de la señal.

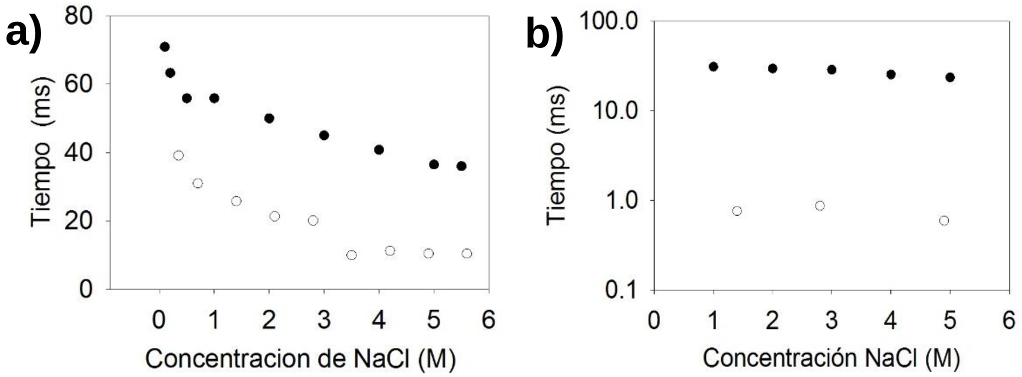

Figura 5.10 T_2^* (círculos vacíos) medidos comparados con los valores T_2 (círculos llenos) reportados por Rijniers et al., 2004, correspondiente a ^{23}Na, a) en soluciones y b) en pastas saturadas con soluciones de NaCl.

La amplitud de señal detectada del ^{35}Cl presenta también una relación lineal con la concentración molar de NaCl en las soluciones (r^2 =0.997) (Figura 5.11a). La Figura 5.11b no muestra una tendencia del comportamiento de T_2^* con relación a la concentración, a diferencia de lo observado en el ^{23}Na. La baja sensibilidad del ^{35}Cl no permitió detectar señal proveniente de la solución en los poros de las pastas de cemento al ser saturadas con soluciones a diferentes concentraciones de NaCl.

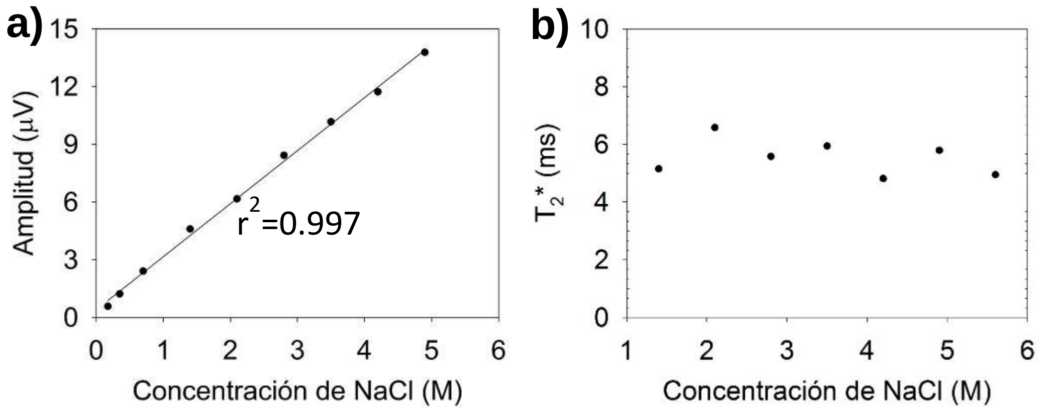

Figura 5.11 a) Amplitud de la señal de ^{35}Cl en función de la concentración molar de NaCl en soluciones y b) Tiempo de decaimiento T_2^* en función de la concentración molar de NaCl en soluciones.

5.3.2 Tiempos de relajación T_2 e intensidades de la señal para ^{23}Na y ^{35}Cl obtenidos con el arreglo Halbach de magnetos

La figura 5.12 muestra las señales típicas de decaimiento para ^{23}Na y ^{35}Cl obtenidas con la técnica CPMG en la solución de NaCl a 5.6 M. La relación señal/ruido fue 138 para el sodio mientras que para el cloro fue 31. Se obtuvo una mejor calidad de señal para el ^{23}Na debido a que tiene mayor sensibilidad y abundancia natural (100%) comparado con el ^{35}Cl que tiene menor sensibilidad y una abundancia natural de 75.53 %.

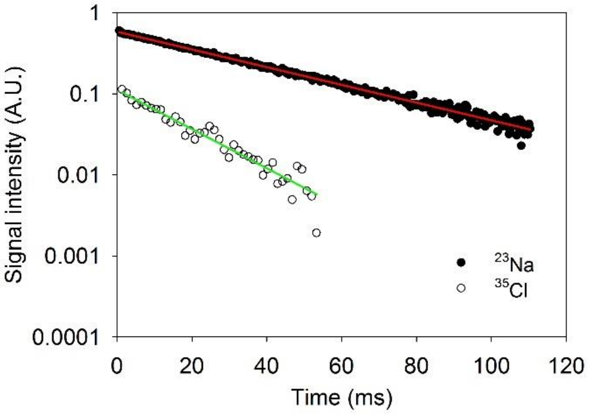

Figura 5.12. Decaimiento de la magnetización transversal obtenida de una solución de 5.6M con la técnica CPMG para núcleos de ^{23}Na y ^{35}Cl.

El comportamiento de la amplitud de las señales para cloro y sodio detectadas mediante la técnica CPMG con las antenas construidas para el arreglo Halbach (Figura 5.13) es similar a lo observado con las señales FID obtenidas en la sección 5.3.1. Existe una relación lineal entre la intensidad de la señal y la concentración molar de NaCl en las soluciones, donde se obtuvieron coeficientes de determinación r^2 de 0.997 y 0.975 para el ^{23}Na y el ^{35}Cl, respectivamente.

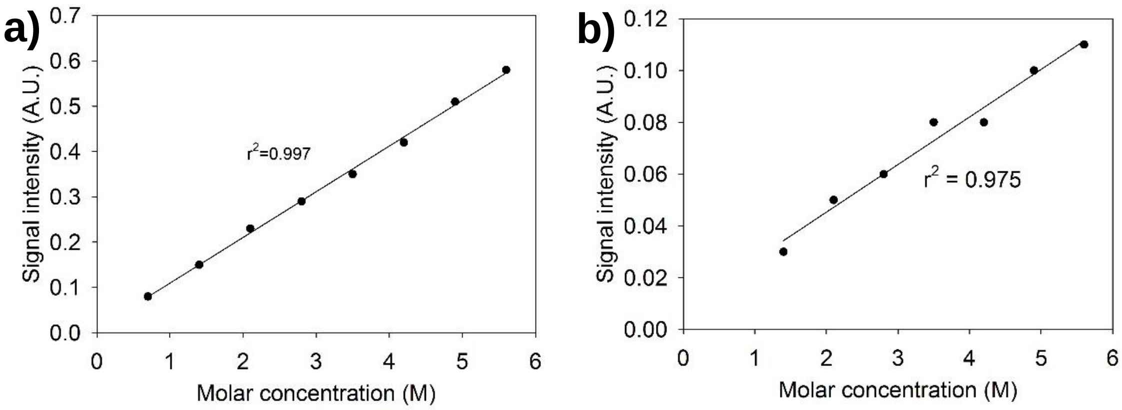

Figura 5.13 Intensidad de señal CPMG en función de la concentración molar de NaCl en soluciones, a) para el ^{23}Na y b) para el ^{35}Cl.

La Figura 5.14 muestra la relación entre el tiempo de decaimiento T_2 (del ^{23}Na y el ^{35}Cl) y la concentración molar de NaCl en soluciones. Se observa el mismo comportamiento observado en T_2^* de las señales FID, para el ^{35}Cl no fue posible observar una tendencia en el comportamiento de T_2 en relación con la concentración molar (Figura 5.14a) mientras que para el ^{23}Na T_2 tiende a disminuir en función de la concentración molar (Figura 5.14b). También se observa que los valores obtenidos de T_2 para el sodio son similares en tendencia y magnitud con los valores de T_2 reportados por Rijniers et al (Rijniers et al., 2004).

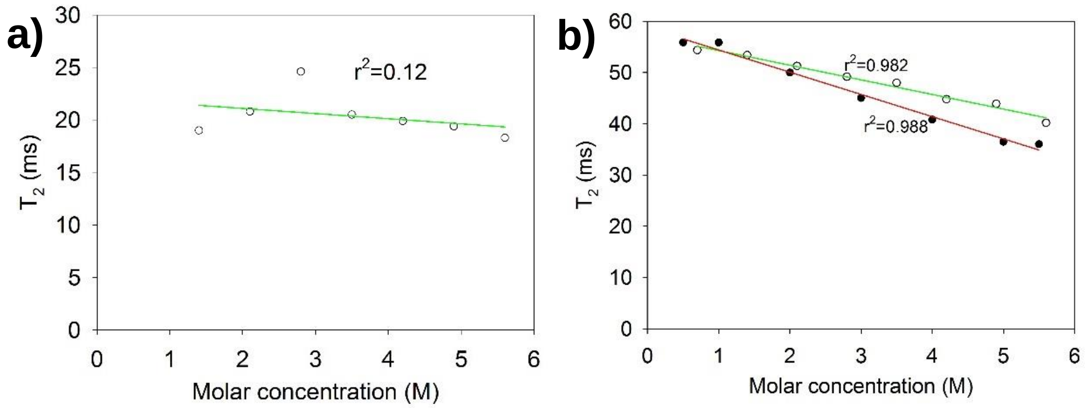

Figura 5.14 Tiempo de decaimiento T_2 en función de la concentración molar de NaCl en soluciones, a) T_2 (círculos vacíos) medidos comparados con los valores T_2 (círculos llenos) reportados por Rijniers et al., 2004, correspondiente a ^{23}Na y b) T_2 medidos para el ^{35}Cl.

5.4 Conclusiones

Los resultados indican que es posible obtener señales de RMN de ^{23}Na y ^{35}Cl en soluciones de NaCl utilizando un sistema de campo bajo. Como se esperaba, las señales obtenidas mostraron una relación lineal entre la intensidad de las señales de RMN y la concentración molar de NaCl en soluciones acuosas, obteniendo para ambos núcleos un alto coeficiente de determinación en concentraciones de NaCl desde 0.175 M hasta 5.6 M ($r^2 > 0.96$). También fue posible detectar señal de ^{23}Na, con la antena construida para el arreglo de magnetos comercial del sistema Maran,con *shims* activos, en pastas de cemento saturadas con soluciones a diferente concentración molar de NaCl. Sin embargo, no se obtuvo señal para el ^{35}Cl debido a su baja sensibilidad y baja abundancia natural. Con relación a las antenas construidas para el arreglo Halbach de magnetos, se obtuvo señal de ambos núcleos en las soluciones, pero no fue posible detectar señal de ^{35}Cl y ^{23}Na en las pastas de cemento saturadas, a pesar de que el arreglo genera un campo B_0 más intenso, pero menos homogéneo. Por lo tanto, se debe considerar en futuros diseños la implementación de *shims* activos o pasivos en la construcción de arreglos de magnetos permanentes para obtener mayor intensidad y homogeneidad del campo magnético.

5.5 Recomendaciones

Se recomienda continuar con la utilización del arreglo tipo Halbach o bien construir una antena de RF para el arreglo de tres magnetos que permita obtener perfiles de la señal de ^{23}Na y correlacionar los resultados con los perfiles de concentración de cloruros obtenidos con técnicas tradicionales de titulación potenciométrica y frente de penetración por colorimetría.

Agradecimientos

P. Cano agradece al Consejo Nacional de Ciencia y Tecnología (CONACYT) de México y al SIP-IPN por financiar los proyectos con claves 239727 y 20170803, respectivamente. F. Díaz agradece a Conacyt por la beca de estudios de doctorado y a la COFAA-IPN por la beca BEIFI.

5.6 Referencias

Balcom, B. J., Cano-Barrita, P. F. D. J., Choi, C., Beyea, D., Goodyear, D. J., & Bremer, T. W. (2003). Single-point Magnetic Resonance Imaging (MRI) of cement based materials. *Materials and Structures/Materiaux et Constructions*, *36*(257), 166–182. https://doi.org/10.1007/BF02479555

Baroghel-Bouny, V., Belin, P., Maultzsch, M., & Henry, D. (2007). AgNO3 spray tests: Advantages, weaknesses, and various applications to quantify chloride ingress into concrete. Part 2: Non-steady-state migration tests and chloride diffusion coefficients. *Materials and Structures/Materiaux et Constructions*, *40*(8), 783–799. https://doi.org/10.1617/s11527-007-9236-y

Blümich, B., Blümler, P., Eidmann, G., Guthausen, A., Haken, R., Schmitz, U., … Zimmer, G. (1998). The NMR-MOUSE: Construction, excitation, and applications. *Magnetic Resonance Imaging*, *16*(5–6), 479–484. https://doi.org/10.1016/S0730-725X(98)00069-1

Cano, F. de J., Bremner, T. W., Mcgregor, R. P., & Balcom, B. J. (2002). Magnetic resonance imaging of 1H , 23Na , and 35Cl penetration in Portland cement mortar. *Cement and Concrete Research*, *32*, 1067–1070.

Enjilela, R., Cano-Barrita, P. F. de J., Komar, A., Boyd, A. J., & Balcom, B. J. (2018). Wet front penetration with unsteady state wicking in mortar studied by Magnetic Resonance Imaging (MRI). *Materials and Structures/Materiaux et Constructions*, *51*, 1–16. https://doi.org/10.1617/s11527-018-1142-y

Enjilela, Razieh, Cano-Barrita, P. F. J., Komar, A., Boyd, A. J., & Balcom, B. J. (2017). Monitoring steady state moisture distribution during wick action in mortar by magnetic resonance imaging (MRI). *Materials and Structures/Materiaux et Constructions*, *50*(2), 1–12. https://doi.org/10.1617/s11527-017-1017-7

García-Naranjo, J. C., Guo, P., Marica, F., Liao, G., & Balcom, B. J. (2014). Magnetic Resonance Core-Plug Analysis with the Three-Magnet Array Unilateral Magnet. *Petrophysics*, *55*(3), 229–239.

Lahajnar, G., Blinc, R., Rutar, V., Smolej, V., Zupančič, I., Kocuvan, I., & Uršič, J. (1977). On the use of pulse NMR techniques for the study of cement hydration. *Cement and Concrete Research*, *7*(4), 385–394. https://doi.org/10.1016/0008-8846(77)90066-7

Manz, B., Coy, A., Dykstra, R., Eccles, C. D., Hunter, M. W., Parkinson, B. J., & Callaghan, P. T. (2006). A mobile one-sided NMR sensor with a homogeneous magnetic field: The NMR-MOLE. *Journal of Magnetic Resonance*, *183*(1), 25–31. https://doi.org/10.1016/j.jmr.2006.07.017

Miljkovc, L., Lasic, D., MacTavish, J. C., & Pintar, M. M. (1988). NMR STUDIES OF HYDRATING CEMENT: A SPIN-SPIN RELAXATION STUDY OF THE EARLY HYDRATION STAGE L. *CEMENT and CONCRETE RESEARCH.*, *18*, 951–956.

Neville, A. (1995). Chloride attack of reinforced concrete: an overview. *Materials and Structures*, *28*(2), 63–70. https://doi.org/10.1007/BF02473172

NT Build 443. CONCRETE, HARDENED: ACCELERATED CHLORIDE PENETRATION Key (1995).

Pel, L., Donkers, P. A. J., Kopinga, K., & Noijen, J. J. (2016). 1H, 23Na and 35Cl Imaging in Cementitious Materials with NMR. *Applied Magnetic Resonance*, *47*(3), 265–276. https://doi.org/10.1007/s00723-015-0752-6

Plassais, A., Pomiès, M. P., Lequeux, N., Boch, P., Korb, J. P., & Petit, D. (2001). Micropore size analysis in hydrated cement paste by NMR. *Magnetic Resonance Imaging*, *4*(11), 493–495. https://doi.org/10.1016/S1387-1609(01)01328-7

Rijniers, L. A., Magusin, P. C. M. M., Huinink, H. P., Pel, L., & Kopinga, K. (2004). Sodium NMR relaxation in porous materials. *Journal of Cardiovascular Magnetic Resonance*, *167*, 25–30. https://doi.org/10.1016/j.jmr.2003.11.008

Yun, H., Patton, M. E., Garrett, J. H., Fedder, G. K., Frederick, K. M., Hsu, J., … Sides, P. J. (2004). Detection of free chloride in concrete by NMR. *Cement and Concrete Research*, *34*, 379–390. https://doi.org/10.1016/j.cemconres.2003.08.020

Capítulo 6. Crack width estimation in cement paste and mortar by low field magnetic resonance

Abstract

Cracking produced by several processes negatively affects durability of concrete structures by increasing the permeability of the cover concrete. Traditional evaluation of the crack width is done using clear plastic cards or hand-held microscopes. Other techniques involve nondestructive examination or image processing. In this paper, low field nuclear magnetic resonance is used to measure the CPMG decay of water-filled artificial cracks in cement paste samples to relate the T_2 lifetime with the crack width. Specimens of 0.50 w/c ratio cement paste were made in triplicate, using ordinary Portland cement, white Portland cement, ordinary Portland cement plus 10 % silica fume, and ordinary Portland cement plus 20 % fly ash. Also, a set of mortar specimens with the same w/c ratio were prepared with Ordinary Portland cement and silica sand. Different gauge stainless steel shims were used to generate artificial cracks in the specimens. After the curing period, the samples were vacuum saturated with water and NMR measurements were performed with the CPMG technique. The results showed that one of the T_2 components has a linear relationship with the crack width, as well as with the signal intensity, that is related with the volume of the cracks.

Keywords: *crack width, magnetic resonance, cement paste*

6.1. Introduction

Cracking of concrete is caused by different factors occurring in both plastic and hardened state. In the plastic state, cracking is the result of plastic shrinkage or settlement, whereas in the hardened state it is caused by restrained drying shrinkage, thermal stresses, deleterious chemical reactions, weathering, corrosion of reinforcement, carbonation, construction overloads, and externally applied loads (ACI Committee 224, 2007). Cracks directly affect the durability of concrete structures by significantly increasing the permeability of the material to aggressive species (Aldea, Shah, & Karr, 1999), especially cracks having a width > 200 μm. The location and extent of cracking can be determined by direct and indirect observations, as well as by destructive and nondestructive testing (ACI Committee 224, 2007). Direct observations are undertaken using hand-held microscopes or clear plastic cards that provide an accuracy in the measurement of crack width of approximately 25 μm (Figure 6.1). Other techniques involve the processing of high-resolution images to detect cracks as narrow as 250 μm (Rivera, Josipovic, Lejeune, Luna, & Whittaker, 2015) and others where the resolution of the image was about 300 μm (Zhang, Zhang, Qi, & Liu, 2014), which precludes its application for the detection of narrower cracks that are of interest from the point of view of durability. MRI has been used to detect cracks but the limitation of resolution of the images restricts the application to observe only wide cracks (Young, Szomolanyi, Bremner, & Balcom, 2004). This paper presents an application of low field NMR to relate the crack width in cement pastes and mortars with the T_2 lifetime component and its corresponding contribution to the signal intensity.

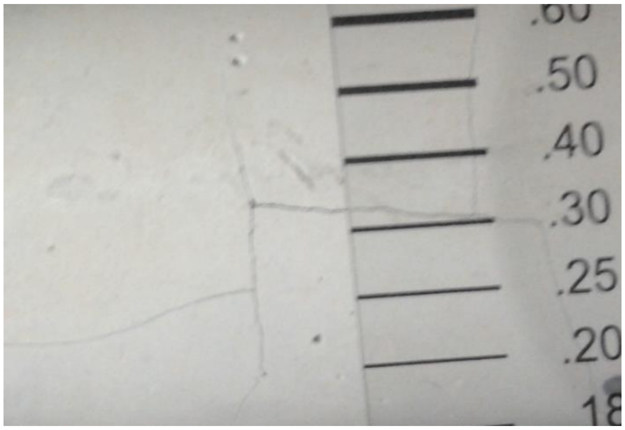

Figure 6.1 Crack comparator to estimate crack width in concrete materials.

6.2. Materials and method

A set of 22 cement paste specimens (w/c = 0.50) measuring 40 mm in length and 36 mm in diameter was prepared for each of the following mixtures: ordinary Portland cement, white cement, ordinary Portland cement with 10% silica fume (SF), ordinary Portland cement with 20% class F fly ash (FA). A set of 22 mortar samples (w/c = 0.50) and sand/cement ratio (w/w) of 2 were also prepared. After casting, stainless steel shims were placed inside the pastes to simulate cracks with 10 different widths (See Figure 6.2) with depth of 3 cm. The control specimens were without stainless steel shims. Additionally, a set of 27 specimens of ordinary Portland cement paste (w/c = 0.50) were prepared to create artificial cracks with 1.5 cm, 2.5 cm and 3.5 cm in depth using three thicknesses of stainless-steel shims (0.076 mm, 0.127 mm and 0.254 mm). Then the specimens were stored inside a plastic bag with a saturated cloth to provide a high humidity to prevent moisture loss from the specimens. After 24 hours, the specimens were demolded and moist cured in lime-saturated distilled water for seven days.

Figure 6.2 Artificial cracks in Portland cement and mortar specimens. The crack width was formed with stainless-steel shim inserted in the fresh cement paste and then extracted after the final setting of the cement paste.

After the moist curing period, NMR measurements were performed using a MARAN DRX-HF 12/50 NMR system (Oxford Instruments Ltd, Abingdon, Oxford, UK) operating at a resonant frequency of 12.9 MHz. To ensure that the crack would be completely saturated with water, the specimens were vacuum saturated before the NMR measurements. The CPMG sequence was used to obtain the transverse magnetization decay, using the parameters shown in Table 6.1. The CPMG signal was best fitted to a four components exponential decay curve (Eq. 6. 1) to obtain the T_2 lifetimes and their corresponding signal intensities.

$$S(t) = M_{0,1} * e^{-\frac{t}{T_{2,1}}} + M_{0,2} * e^{-\frac{t}{T_{2,2}}} + M_{0,3} * e^{-\frac{t}{T_{2,3}}} + M_{0,4} * e^{-\frac{t}{T_{2,4}}} \tag{6.1}$$

where S is the signal intensity, t is time, $M_{0,1}$, $M_{0,2}$, $M_{0,3}$ and $M_{0,4}$ are the equilibrium sample magnetization components corresponding to the $T_{2,1}$, $T_{2,2}$, $T_{2,3}$ and $T_{2,4}$ lifetime constants, respectively.

Table 6.1 Parameters used for the CPMG measurements

Parameters	ID	Value
90 degree pulse (μs)	P90	18.5
180 degree pulse (μs)	P180	37
Number of echoes	NECH	2048
Number of scans	NS	256
Recycle delay (s)	RD	1.5
Echo time (μs)	TAU	150

Because it was necessary to know the behavior of the magnetic field within the crack, the finite element software COMSOL Multiphysics® (COMSOL, Burlington, MA, USA) was used to simulate the B_0 magnetic field profile through the cracks. The geometry of a pair of circular permanent magnets of 30 cm in diameter and 2.5 cm thick was used with a separation of 4 cm generating a relatively uniform magnetic field of 0.3 T. To simulate the specimens with a crack, a rectangular prism with dimensions of 3.0 cm in width x 3 cm in length x 4 cm in height, having a relative permeability of 1.1 for concrete (Brake, 2016) was used. To simulate the crack in the center of the specimen, a rectangular prism with dimensions of 1.29 cm in length x 3 cm in height x t cm in thickness corresponding to the artificial cracks. The relative permeability of this volume was 0.999991, which is for the water filling the crack. All the elements were enclosed within a sphere of air with 30 cm in radius.

6.4 Analysis of NMR relaxation in the cement paste and in the cracks

There are three relaxation mechanisms of a fluid within a porous material such as rocks or concrete: bulk fluid processes (T_{2Bulk}), surface relaxation ($T_{2Surface}$) and diffusion in the presence of a magnetic field gradient ($T_{2Diffusion}$). The T_2 lifetime in a pore is affected by the three mechanisms according to equation 6.2 (Blümich et al., 2004; Coates, Xiao, & Prammer, 1999).

$$\frac{1}{T_2} = \frac{1}{T_{2bulk}} + \rho_2\left(\frac{S}{V}\right) + \frac{D(\gamma G T E)^2}{12} \quad (6.2)$$

where T_{2bulk} is the relaxation of bulk fluid, ρ_2 is the surface relaxivity of the pore wall, $\frac{S}{V}$ is the surface/volume ratio of the pore space, D is the diffusion coefficient, γ is the gyromagnetic ratio, G is the gradient of magnetic field B_0 inside the pore, and TE is the echo time used in the CPMG sequence.

According to the work of Brownstein and Tarr (Brownstein & Tarr, 1979), there are three regimes depending on the value of a term κ (Eq. 6.3): fast diffusion regime ($\kappa<1$), intermediate-diffusion regime ($1< \kappa>10$) and slow-diffusion regime ($\kappa>10$).

$$\kappa = \frac{\rho_2 * r}{D} \tag{6.3}$$

where ρ_2 is the surface relaxivity, r is the radius of the pore and D is the self-diffusion coefficient of the fluid. The κ calculated was in the range of 0.052 to 0.49 for the width range of artificial cracks considering ρ_2 = 5.51μm/s for C-S-H, value reported by Dalas et al (Dalas et al., 2014), and D = 2000 $\mu m^2/s$ for the water diffusion coefficient at room temperature (Coates et al., 1999). The calculated values of κ indicated that the crack widths considered in the study were in the fast-diffusion regime, and the maximum allowable crack width for this regime was ≈725 μm.

In the analysis of water relaxation within the artificial cracks, the three relaxation mechanisms were considered according to equation 6.2. The T_{2Bulk} = 2.4 s was measured for free water, $T_{2diffusion}$ was calculated with the D value mentioned above, $\gamma = 42.58$ MHZ /s, G was the B_0 gradient inside each crack obtained from COMSOL simulations, and $TE = 150\ \mu s$. A rectangular prism geometry was used to determine the $\frac{S}{V} = \frac{(2ab+2db+ad)}{abd}$ for $T_{2Surface}$, assuming a crack shape shown in Figure 6.3.

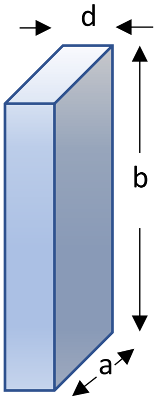

Figure 6.3 Rectangular prism geometry of the artificial cracks used to determine the s/v ratio.

6.3 Results and discussion

Figure 6.4 shows the CPMG decays of a cement paste sample with a 203 μm crack width and a control sample. There is a faster decay in the sample without crack. The NMR signal decay is dominated by the bulk of the cement paste, and only a small part (about 1%) corresponds to signal of water in the cracks.

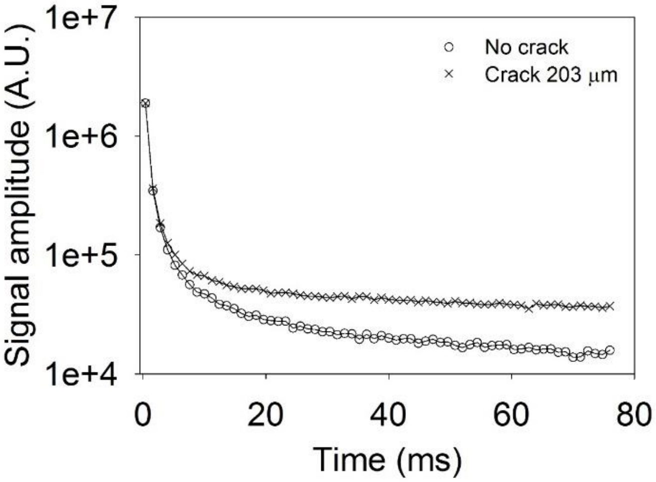

Figure 6.4 CPMG decays of ordinary Portland cement paste samples with and without crack.

In the CPMG signal fitted to a four-component exponential decay function, the first, second and third components are attributed to gel pores, inter-hydrate pores and capillary pores, respectively; the fourth component is attributed to water in the largest capillary pores and micro-cracks (Muller, 2014),(Kowalczyk, Gajewicz, & Mcdonald, 2014). In this case it was observed a linear relationship between signal intensity and T_2 lifetime with the crack width (Figure 6.5). The other components did not exhibit a specific relationship. The proportional increase in T_2 lifetime as the crack width increases (Figure 6.5a) is because the surface relaxation is less effective as the separation between the crack surfaces increases. Therefore, it is possible that at a specific upper range of crack width, the water contained will start behaving as bulk water. On the other hand, the increase in signal intensity of the fourth component is explained by the increase in crack volume (water volume) as the crack width increases (Figure 6.5b). This behavior is observed in a similar way for the other types of samples.

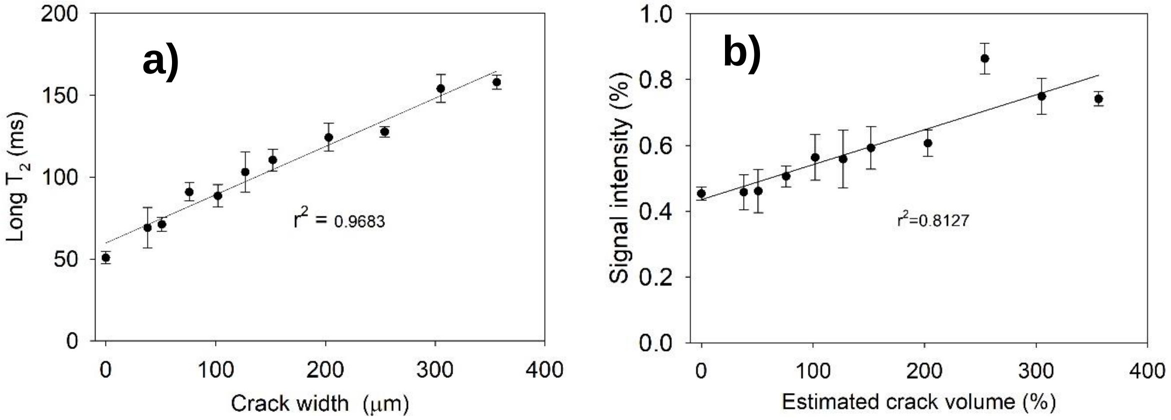

Figure 6.5 Ordinary Portland cement pastes (w/c = 0.50) with artificial cracks, a) T_2 lifetime versus crack width, and b) Signal intensity versus crack volume. The first point at cero width crack is the control specimen.

Figure 6.6 shows the relationship between T_2 lifetime and the crack width for OPC, white cement, OPC plus 10% SF, OPC plus 20% FA cement pastes, and mortar at different curing times. In case of white cement paste and OPC paste, an increase in the $T_{2,4}$ lifetime values were observed with increasing age, which may be due to changes in the surface relaxivity ρ caused carbonation of the surface.

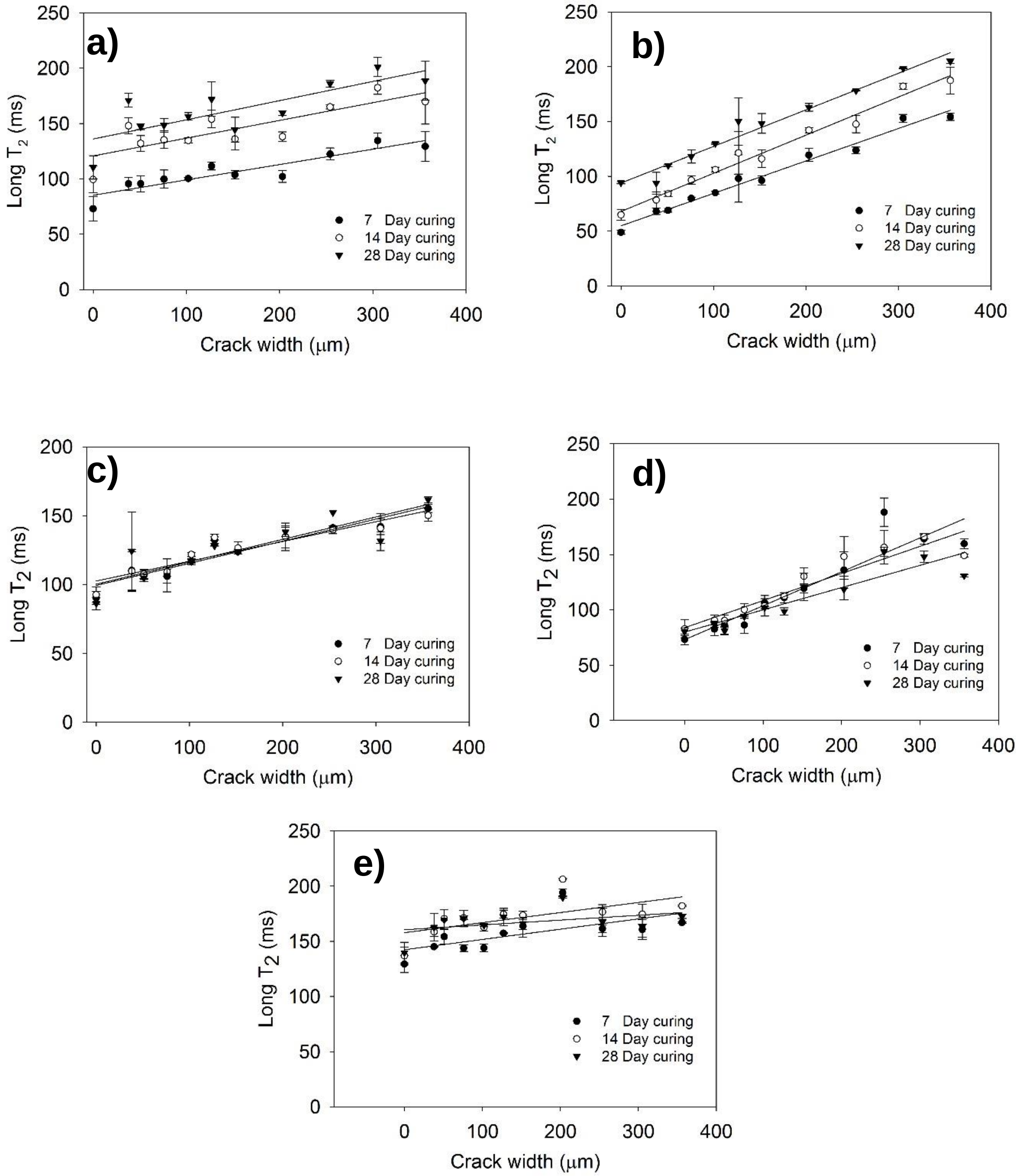

Figure 6.6 Crack width versus T_2 relationship obtained in cement pastes at different ages of curing, where the points in zero crack width correspond to control samples, a) OPC paste, b) White cement paste, c) OPC + 10 % SF, d) OPC + 20 % FA, and e) OPC mortar.

Results of the simulation of the magnetic field B_0 inside the cracks are shown in Figure 6.7. There is a magnetic field gradient along the crack. This gradient was determined for each crack width and it was considered in the calculation of $T_{2diffusion}$. However, these gradient values were not high enough to produce a significant change in T_2 through the diffusion mechanism.

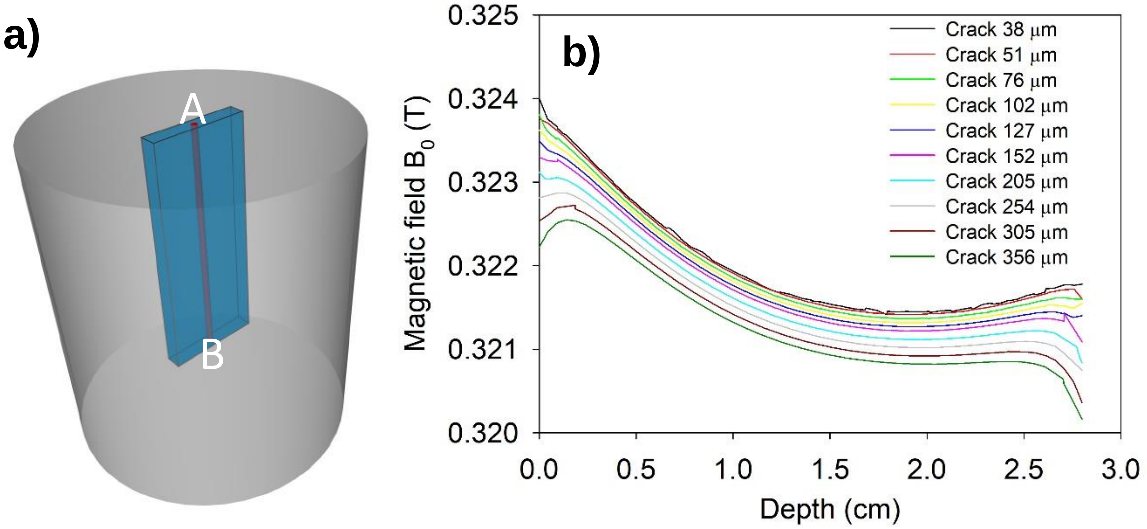

Figure 6.7 a) The magnetic field gradient in the crack was obtained along the line AB, A corresponds to 0 and B the depth = 3 cm. b) B_0 field gradient within the cracks obtained from the simulation in COMSOL Multiphysics

Figure 6.8a shows a comparison between T_{24} values measured in OPC pastes with artificial cracks and the $T_{2,4}$ values calculated for cracks according to equation 6.2, considering a rectangular prism geometry for the crack (see Fig. 6.3). It was observed that the calculated $T_{2,4}$ values far exceeded the measured $T_{2,4}$. Since the hydrated cement paste possesses a rough surface on a microscopic scale (Apedo, Montgomery, Serres, Fond, & Feugeas, 2016; Thomas, Jennings, & Allen, 1999) as shown in a roughness profile in figure 6.9, it implies that in Equation 6.2, the real surface inside the cracks is not being adequately considered.

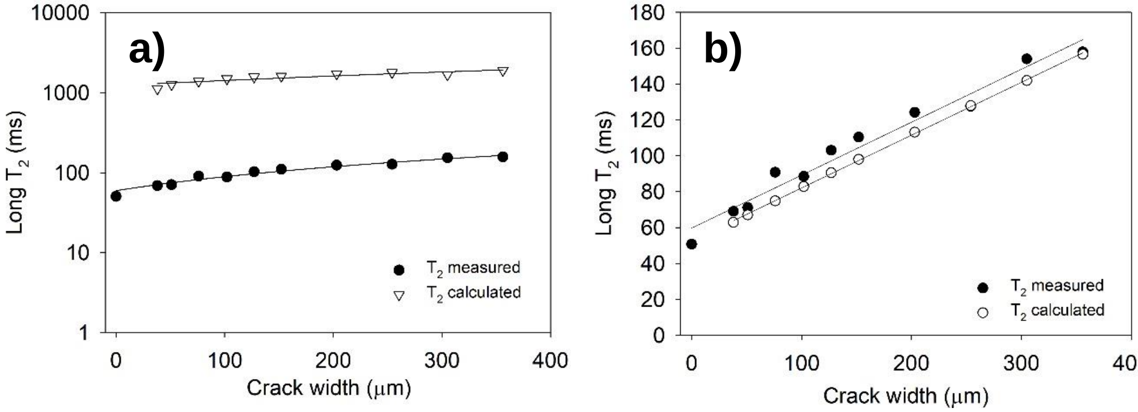

Figure 6.8 Comparison between measured and calculated T_2 values of OPC paste samples, a) Without considering the roughness in the surface of the crack's walls and the background, and b) Considering that the surface of the crack walls is magnified by a factor R = 280 due to its fractal nature and adding the value of $T_{2control}$ as background.

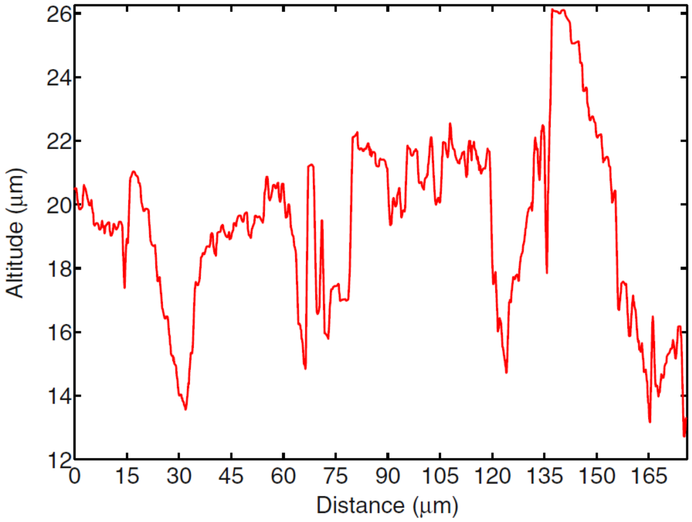

Figure 6.9 Profile of the roughness from an unpolished cement paste sample (Apedo et al., 2016).

The calculation of the profile line length in Figure 6.9 indicates that stretching the profile line in a straight line covers a distance $l = 1.5$ greater than the original. This means that a surface with the same roughness must cover an area up to $l^2 = 2.25$ times larger than the original. Therefore, the area S in Equation 6.2 has to consider a magnification factor R = 2.25.

$$T_{24} = T_{2\,crack} + T_{2\,control} \qquad (6.4)$$

However, a 2.25 factor was not enough to obtain measured values close to the predicted ones. A value of magnification factor $R = 280$ is what permitted obtaining the calculated values of $T_{2,4}$ with a slope similar to that presented by the measured values. It is also necessary to add the $T_{2\,control}$ (Eq. 6.4), since it is considered as a background in the absence of artificial cracks to approximate the calculated values of $T_{2,4}$ with the measured values of $T_{2,4}$ as shown in Figure 6.8b, where this background can be attributed to micro-cracking and macropores naturally formed in the specimen.

On the other hand, it has been shown that the surface of the hydrated cement paste is fractal in nature, which has large fractal dimension D values (between 2.95 to 3.09) which means that it has an extremely irregular surface (Winslow, 1985). For this reason, it is possible that if roughness profiles such as that in Figure 6.8 were analyzed at a higher magnification, a larger surface magnification factor could be determined. It has also been shown that a larger surface area within the same volume would cause a more efficient T_2 relaxation, as demonstrated by Muller-Petke et al (Müller-petke, Dlugosch, Lehmann-horn, & Ronczka, 2015) with the simulation of T_2 relaxation times in pores with different fractal surfaces.

Figure 6.10 shows the $T_{2,4}$ values in the samples with cracks of different depths (1.5, 2.5 and 3.5 cm). There is a trend indicating that there is an increase in T_2 as the depth of the crack increases. However, an analysis of variance with the SigmaPlot software showed that there is no significant difference between the data.

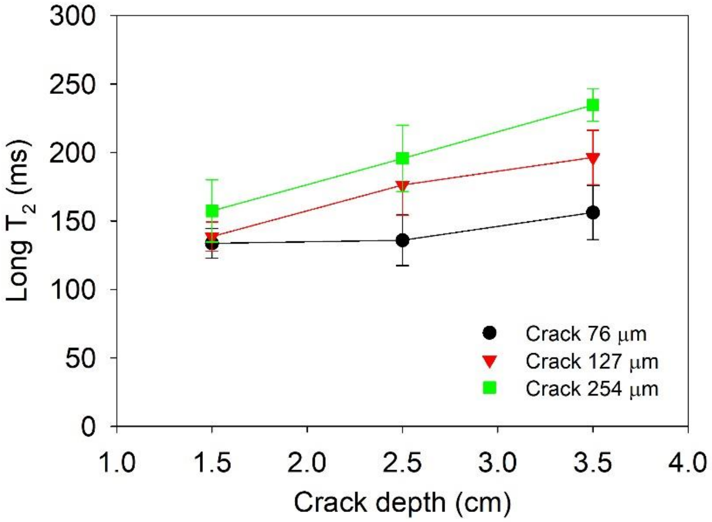

Figure 6.10 Relationship between T_{24} and the cracks depth, using three different crack widths.

6.4 Conclusions

NMR signals obtained by CPMG measurements provide a means of estimating the crack width in cement pastes, where a four-component exponential decay function was fit to the data. The fourth T_2 component and its corresponding signal intensity, have a linear relationship with the crack width.

The surface relaxation mechanism of the water within the cracks seems to dominate the signal decay.

A rectangular prism geometry was considered as the shape of the artificial cracks generated. However, to calculate the s/v ratio of the crack, it is necessary to consider that the surface is magnified by a factor of approximately 280 times, since the hydrated cement paste is a rough material of a fractal nature.

No significant changes were observed in the measured $T_{2,4}$ values when varying the depth maintaining the crack width constant.

Acknowledgements

P. Cano acknowledges Consejo Nacional de Ciencia y Tecnologia (Conacyt). F. Diaz acknowledges CONACYT for a graduate studies scholarship and to the COFAA-IPN for a BEIFI scholarship.

6.5 References

ACI Committee 224. (2007). *Causes , Evaluation , and Repair of Cracks in Concrete Structures*. Farmington Hills, MI.

Aldea, C.-M., Shah, S. P., & Karr, A. (1999). Effect of Cracking on Water and Chloride Permeability of Concrete. *Journal of Materials in Civil Engineering*, *11*(3), 181–187.

Apedo, K. L., Montgomery, P., Serres, N., Fond, C., & Feugeas, F. (2016). Geometrical roughness analysis of cement paste surfaces using coherence scanning interferometry and confocal microscopy. *Materials Characterization*, *118*, 212–224. https://doi.org/10.1016/j.matchar.2016.05.023

Blümich, B., Anferova, S., Pechnig, R., Pape, H., Arnold, J., & Clauser, C. (2004). Mobile NMR for porosity analysis of drill core sections. *Journal of Geophysics and Engineering*, *1*(3), 177–180. https://doi.org/10.1088/1742-2132/1/3/001

Brake, K. A. T. E. and N. A. (2016). International Conference on Transportation and Development 2016 : Projects and Practices for Prosperity. (p. 1253). Retrieved from http://apps.webofknowledge.com.proxy.lib.uwaterloo.ca/full_record.do?product=WOS&search_mode=GeneralSearch&qid=3&SID=5FDZgIPKgm413cSsw85&page=3&doc=24&cacheurlFromRightClick=no

Brownstein, K. R., & Tarr, C. E. (1979). Importance of classical diffusion in NMR studies of water in biological cells. *Physical Review A*, *19*(6), 2446–2453. https://doi.org/10.1103/PhysRevA.19.2446

Coates, G. R., Xiao, L., & Prammer, M. G. (1999). *NMR logging applications*. Houston, Texas, USA: Halliburton Energy Services.

Dalas, F., Korb, J., Pourchet, S., Nonat, A., Rinaldi, D., & Mosquet, M. (2014). Surface Relaxivity of Cement Hydrates. *Phisical Chemistry*. https://doi.org/10.1021/jp500055p

Kowalczyk, R. M., Gajewicz, A. M., & Mcdonald, P. J. (2014). The mechanism of water-isopropanol exchange in cement pastes evidenced by NMR relaxometry. *RSC Advances*, *4*(40), 20709–20715. https://doi.org/10.1039/c4ra00889h

Müller-petke, M., Dlugosch, R., Lehmann-horn, J., & Ronczka, M. (2015). Nuclear magnetic resonance average pore-size estimations outside the fast-diffusion regime, *80*(3).

Muller, A. C. A. (2014). *Charles, Muller - 2014 - Characterization of porosity & C-S-H in cement pastes by 1 H NMR*. École Polytechnique Fédérale de Lausanne.

Rivera, J. P., Josipovic, G., Lejeune, E., Luna, B. N., & Whittaker, A. S. (2015). Automated Detection and Measurement of Cracks in Reinforced Concrete Components. *ACI Structural Journal*, *112*(3), 397–405.

Thomas, J. J., Jennings, H. M., & Allen, A. J. (1999). The surface area of hardened cement paste as measured by various techniques. *Concrete Science and Engineering*, *1*(March), 45–64. https://doi.org/10.1016/S0008-8846(98)00049-0

Winslow, D. N. (1985). THE FRACTAL NATURE OF THE OF CEMENT PASTE. *Cement and Concrete Research*, *15*, 817–824.

Young, J. J., Szomolanyi, P., Bremner, T. W., & Balcom, B. J. (2004). Magnetic resonance imaging of crack formation in hydrated cement paste materials. *Cement and Concrete Research*, *34*(8), 1459–1466.

Zhang, W., Zhang, Z., Qi, D., & Liu, Y. (2014). Automatic crack detection and classification method for subway tunnel safety monitoring. *Sensors (Basel, Switzerland)*, *14*(10), 19307–19328.

Conclusiones generales

Los resultados de los estudios presentados en esta tesis confirman que es posible implementar métodos confiables de caracterización de algunos aspectos relacionados con la durabilidad del concreto de manera no destructiva. Aprovechando las ventajas de la resonancia magnética nuclear de campo bajo, dada su versatilidad ha sido posible el diseño, construcción e implementación de antenas de RF para adaptarlos a las necesidades de los distintos tipos de arreglo de magnetos utilizados en esta investigación.

El diseño y construcción de una antena elíptica de superficie para el arreglo de tres magnetos permitió mejorar significativamente la resolución espacial comparado con un estudio previo (Cano-Barrita et al., 2017). Esto se debió a que con la forma elíptica se pudo reducir la zona de influencia de la antena a lo largo de la muestra. Además, se pudieron extender las mediciones a morteros saturados y sin saturar donde se pudieron observar diferencias en los tiempos de relajación T_2 e intensidad en la zona carbonatada con respecto a la zona no carbonatada. Además, se obtuvieron perfiles de contenido de humedad durante absorción capilar de agua en muestras de mortero y concreto conteniendo agregados naturales. Los perfiles obtenidos fueron similares a los obtenidos con la técnica de imagenología de RMN. Debe mencionarse que en la muestra de concreto no fue posible obtener un perfil de distribución de humedad por medio de imagenología por RMN. Sin embargo, si fue posible con el arreglo de tres magnetos y la antena elíptica, que además no tiene restricción en le tamaño de la muestra a ensayar.

Las antenas de RF construidas para detectar ^{35}Cl y ^{23}Na permitieron obtener señales de calidad aceptable en campo bajo. Para ambos núcleos activos se obtuvo una buena correlación ($r^2 \geq 0.96$) entre las intensidades de señales (CPMG y FID) y la concentración molar de NaCl en soluciones acuosas. También fue posible la detección de señal de ^{23}Na en pastas de cemento saturadas con soluciones a diferentes concentraciones de NaCl usando el arreglo de magnetos comercial de un sistema de imagenología por RMN, que al contar con *shims* activos permitió incrementar la homogeneidad del campo magnético B_0. Con el arreglo Halbach de magnetos solo se pudo obtener señales de RMN de ^{35}Cl y ^{23}Na en soluciones de NaCl a distintas concentraciones, a pesar de generar un mayor campo magnético, pero más heterogéneo y en un menor volumen.

Finalmente, se demostró que los tiempos de vida de la señal T_2 poseen una relación lineal con el ancho de grietas artificiales en pastas de cemento y morteros ($r^2 = 0.96$). Por otra parte, la relajación del agua contenida en la grieta está mayormente influenciada por la relajación por superficie, donde la superficie de las paredes de la grieta debe calcularse considerando que la pasta de cemento hidratada es un material rugoso de naturaleza fractal. Se estimó de manera empírica un valor de 280 veces el incremento de área en la grieta para que los datos medidos fueran similares a los calculados.

Lista de publicaciones

Artículos en Journals

Floriberto Díaz Díaz, Prisciliano F. de J. Cano Barrita, Frank Manuel León Martínez, Francisco Castellanos, Unilateral low-field magnetic resonance measurements of carbonation depth in unsaturated and saturated Portland cement mortars, Cement and Concrete Research, 138. https://doi.org/10.1016/j.cemconres.2020.106237

Prisciliano F. de J. Cano Barrita, **Floriberto Díaz Diaz**, Moisture distribution profiles during water absorption of mortars obtained nondestructively by low-field unilateral magnetic resonance, Submitted to Materials and Structures, December 2020.

Artículos o presentaciones en congresos

P. F. de J Cano-Barrita., **Floriberto Díaz Díaz**, Frank Manuel León Martínez, Francisco Castellanos. Detección no destructiva del frente de carbonatación en pastas de cemento y mortero, utilizando resonancia magnética de bajo campo. 8° Congreso Nacional Alconpat México. Tuxtla Gutierrez Chiapas. Del 17 al 19 de octubre de 2018.

Díaz-Díaz F., Cano-Barrita P. F. de J. Construcción de antenas de RMN para un arreglo unilateral de magnetos que mejoren los perfiles de Intensidad y T_2. XI Jornadas Politécnicas en Ciencia y Tecnología 2018. Santa Cruz Xoxocotlán, Oaxaca, México. Del 17 al 18 de mayo de 2018.

Díaz-Díaz F., Cano-Barrita P. F. de J. Carbonation front in cement paste and mortar detected by low-field NMR. 14th International conference on magnetic resonance microscopy. Halifax, Nova Scotia, Canadá. Del 13 al 17 de agosto de 2017.

Díaz-Díaz F., Cano-Barrita P. F. de J. Señal de RMN en bajo campo de los núcleos ^{35}Cl y ^{23}Na en soluciones acuosas y pastas de cemento. X Jornadas Politécnicas 2017. Santa Cruz Xoxocotlán, Oaxaca, México. Del 17 al 19 de mayo de 2017.